



**Codes And Methods Improvements
for VVER comprehensive safety assessment**

Grant Agreement Number: 945081

Start date: 01/09/2020 - Duration: 36 Months

WP6 – Task6.2

**D6.2 – Results of Kozloduy-6 Mixing Experiment
Benchmark**

V. Sanchez, M. Böttcher (KIT)
Ch. Marchand, O. Bernard (FRA), U. Bieder, R. Nop (CEA), D. Ruban, A. Hashymov, O.
Sevbo (ER), N. Forgione, O. Halim, A. Pucciarelli (UNIPI)
Version 1 – 27/01/2023



This project has received funding from the Euratom research and training programme 2019-2020 under grant agreement No 945081.

CAMIVVER – Grant Agreement Number: 945081

Document title	Communication and dissemination strategy plan
Author(s)	V. Sanchez-Espinoza, M. Böttcher (KIT), Ch. Marchand, O. Bernard (FRA), U. Bieder, R. Nop (CEA), D. Ruban, A. Hashymov, O. Sevbo (ER), N. Forgiione, O. Halim, A. Pucciarelli (UNIFI)
Document type	Deliverable
Work Package	WP6
Document number	D6.2
Issued by	KIT
Date of completion	27/01/2023
Dissemination level	Public

Summary

This deliverable describes the analysis of the CFD-simulations performed by the different partners of the Coolant Mixing Test at the Kozloduy Unit 6 Nuclear Power plant. In the first part, the coolant mixing test is shortly described as well as the initial and boundary conditions used. In the second part, the different CFD-codes used are described in some details. In the section three, the modelling of the RPV of the Kozloduy plant developed for the CFD simulations of the tests by each partners are described.

In the fourth part, first of all the test data is compared to the predictions of the different CFD-codes and in the second part, a code-to-code comparison of selected data predicted by the tools is performed.

The comparative results are discussed and the main findings presented. The reasons for deviations of the code predictions are explained, too.

Approval




Version	First Author	WP leader	Project Coordinator
1	V. Sanchez Espinoza (KIT) 21/12/2022  Dr. V. Sánchez	O. Bernard (Framatome) 26/01/2023 	D. Verrier (Framatome) 27/01/2023 

Table of contents

Table of contents	3
List of Figures	4
List of Tables	6
1 Introduction	7
2 The coolant mixing test at the VVER-1000/V320 plant	7
2.1 Short description	7
2.2 Goals of the test.....	7
2.3 Measured data	8
3 Short description of the used CFD Codes	8
3.1 STAR CCM+ (FRAMATOME, UPISA)	8
3.2 ANSYS/FLUENT 2019/R3 (ENERGORISK)	9
3.3 ANSYS CFX (KIT)	11
3.4 TrioCFD (CEA)	12
4 CFD RPV and Core models	13
4.1 FRAMATOME Model of the RPV and Core (Star-CCM+).....	13
4.2 UNIPI Model (Star-CCM+).....	18
4.3 KIT Model (ANSYS CFX).....	22
4.4 CEA Model (TrioCFD).....	28
4.5 ENERGORISK Model (ANSYS/FLUENT 2019/R3)	31
5 Overview of model and parameter settings	44
6 Comparative results	46
7 Conclusions	64
8 Bibliography	64
A Additional core configurations	67
A.1 Assorted model results	67

List of Figures

Figure 1: Overview of the geometry	14
Figure 2: Overview of the mesh	15
Figure 2: Cold leg experimental temperatures	16
Figure 3: Hot leg experimental temperatures	16
Figure 4: VVER lower plenum (bottom), upper plenum (top): (a), RPV: (b), and Cross-sectional view of VVER vessel model: (c)	19
Figure 5: Radial power distribution map (left), Axial power distribution map (right).....	20
Figure 6: The old (left) and new model version (right)	23
Figure 7: Coarse mesh (V1) and very fine mesh (V3)	23
Figure 8: Flow through elliptical bottom plate holes by using different meshes	24
Figure 9: Mass flow distribution at core outlet.....	25
Figure 10: Mass flow distribution at core outlet.....	25
Figure 11: Core outlet temperature of V2 at 0s (left) and at 1800s (right)	26
Figure 12: Sketch of inlet swirl boundary condition and the situation at cold leg 1 at t = 0s	27
Figure 13: <i>Overview of the mesh used for TrioCFD</i>	28
Figure 14: <i>Zoom in the lower plenum of the mesh used for TrioCF</i>	28
Figure 15: Mixing coefficient. Comparison between experimental data computed with /without swirl	30
Figure 16: <i>Analytic input for TrioCFD and comparison with experimental data</i>	31
Figure 17: Cold legs, downcomer (only vertical part) / 8.594E05 nodes / 7.946E05 elements	33
Figure 18: Lower plenum (including space of reactor vessel elliptical bottom) / 9.647E06 nodes / 8.748E06 elements	34
Figure 19: Reactor core / 3.448E06 nodes / 3.076E06 elements	35
Figure 20: Upper plenum / 2.915E06 nodes / 2.575E06 elements	36
Figure 21: Hot legs and hot legs collection chamber / 4.154E05 nodes / 3.868E05 elements.....	36
Figure 22: RPV with the main flow paths and the locations for the pressure difference prediction	37
Figure 23: Distribution of average energy release by core height	40
Figure 24: Distribution uneven energy release coefficients by cassettes	41
Figure 25: Comparison of the hot leg 1 temperature predicted by the partners with the data	47
Figure 26: Comparison of the hot leg 2 temperature predicted by the partners with the data	47
Figure 27: Comparison of the hot leg 3 temperature predicted by the partners with the data	48
Figure 28: Comparison of the hot leg 4 temperature predicted by the partners with the data	48
Figure 29: Comparison of the coolant temperature measured at the FA-outlet at 0 s with the predicted values	49
Figure 30: Comparison of the coolant temperature measured at the FA-outlet at 1800 s with the predicted values.....	50
Figure 31: Comparison coolant mixing coefficient (data) of loop-1 with the predictions of the partners	51
Figure 32: Comparison coolant mixing coefficient (data) of loop-2 with the predictions of the partners	51
Figure 33: Comparison coolant mixing coefficient (data) of loop-3 with the predictions of the partners	52
Figure 34: Comparison coolant mixing coefficient (data) of loop-4 with the predictions of the partners	52

Figure 35: Mixing coefficient in dependence of the angular position as predicted by partners and compared to the data..... 53

Figure 36: Coolant temperature at core inlet predicted for the initial state (0 s) by the partners 57

Figure 37: Mass flow rate at core inlet predicted for the initial state (0 s) by the partners 57

Figure 38: Coolant velocity at core inlet predicted for the initial state (0 s) by the partners 58

Figure 39: Coolant temperature at core inlet predicted for the final state (1800 s) by the partners 58

Figure 40: Mass flow rate at core inlet predicted for the final state (1800 s) by the partners 59

Figure 41: Coolant velocity at core inlet predicted for the initial state (0 s) by the partners 59

Figure 42: Coolant mass flow rate at FA-outlet predicted for the initial state (0 s) by the partners 60

Figure 43: Coolant velocity at the FA-outlet predicted for the initial state (0 s) by the partners 61

Figure 44: Coolant mass flow rate at FA-outlet predicted for the final state (1800 s) by the partners. 61

Figure 45: Coolant velocity at FA-outlet predicted for the final state (1800 s) by the partners 62

Figure 46: Loop-1 mass flow rate at the RPV-outlet predicted for the initial state (0 s) by the partners 62

Figure 47: Loop-2 mass flow rate at the RPV-outlet predicted for the initial state (0 s) by the partners 63

Figure 48: Loop-3 mass flow rate at the RPV-outlet predicted for the initial state (0 s) by the partners 63

Figure 49: Loop-4 mass flow rate at the RPV-outlet predicted for the initial state (0 s) by the partners 63

List of Tables

Table 1: Initial and final parameters	15
Table 2: Pressure drop in the vessel	17
Table 3: Parameters for the pressure loss correlation	29
Table 4: Quantitative comparison of the mixing coefficient without and with swirl	30
Table 5: Comparison of the pressure drop in different sections of the RPV regarding the reference value	37
Table 6: Main balance results of quasi-stationary calculation representing initial state of Kozloduy-6 mixing experiment (V1000CT-2)	42
Table 7: <i>Overview of model and parameters used by the different CFD-codes</i>	44
Table 8: <i>Comparison of the pressured drop predicted by the different partners with the reference data</i>	46
Table 9: Comparison of the pressured drop predicted by the different partners with the reference data	46
Table 10: Error statistics of assembly averaged absolute temperature deviation vs. data [K].....	50
Table 11: Average absolute deviation of model results vs. data	52
Table 12: Angular turn analysis	56
Table 13: Core porosity factors of the various models	60

1 Introduction

In the framework of the H2020 CAMIVVER project [1] Work Package 6 is devoted to the CFD-analysis of a coolant mixing test performed in a Nuclear Power Plant of VVER-design located in Kozloduy, Bulgaria. This test is very important to validate the simulation capability of 3D coarse mesh system thermal hydraulic codes and CFD-codes. This Deliverable D6.2 is focused on the analysis of the coolant mixing test.

The coolant mixing within the reactor pressure vessel may take place during accidental conditions e.g. after a main steam line break (MSLB) in a PWR, during boron dilution (BD) accidents and rod ejection accidents (REA). Due to the feedbacks of the thermal hydraulics with the core neutronics, these situations may lead to a non-symmetrical behaviour of the core meaning that the power generation in the core will be distorted in some way. Under such conditions, it is important to assess overall core behaviour regarding safety relevant phenomena such as DNB, power increase and re-criticality.

Hence, it is of paramount importance to assess the prediction capability of system thermal hydraulic and CFD codes by analysing appropriate experiments such as the one performed during the commissioning phase of the VVER-1000 Unit 6 at Kozloduy.

In the CAMIVVER Project, the focus is the validation of different CFD tools such as ANSYS CFX (KIT), ANSYS FLUENT (ENERGORISK), STAR-CCM+ (FRAMATOME, UPISA) and TrioCFD (CEA) using the unique coolant mixing data.

2 The coolant mixing test at the VVER-1000/V320 plant

2.1 Short description

The coolant mixing test was performed at the Kozloduy Unit 6 – a VVER-1000/W320 reactor design- during the commissioning phase in order to study the coolant mixing in the downcomer and the propagation of the mixing pattern to the core. The initial state is at BOC and at low power level (9.4 % of the nominal power).

The test is initiated by isolation of one steam generator (loop-1) which leads to a deterioration of the heat transfer from the primary to the secondary side: Hence, the temperature of the primary coolant of the loop-1 is increasing. Consequently, the coolant in the downcomer sector connected to the loop-1 is increasing while the coolant temperature of the other downcomer sectors is not directly perturbed. Under such conditions, a coolant mixing takes place between the hotter coolant of sector linked to loop-1 with the coolant of the other sectors. The resulting mixing pattern propagates along the downcomer downwards the lower plenum and from there to the core. More details of the test can be found in [2]. During the tests all MCP remained in operation. Non-uniform and asymmetric loop flow mixing in the reactor vessel was observed in the event of asymmetric loop operation. For certain flow patterns, there has been a shift of the main loop flows with respect to the cold leg axes (a swirl) since the loops are not arranged symmetrically. The test was initiated at 04:29 am at 29.06.1991 and the main thermal hydraulic plant parameters were stabilized after 30 minutes.

The main changes in observed plant parameters took place within the first 10 minutes. After that, the plant has been stabilized after 20 min. with three working SGs and one isolated SG.

Important thermal hydraulic parameters of the loops and the core were recorded for code validation purposes, which will be used to validate the different CFD-codes in this project.

2.2 Goals of the test

The main objectives to the coolant mixing test are the following:

- Provide reliable experimental data for code validation,
- Evaluate the mixing coefficients i.e. rate of mass exchange between each pair of loops, for two in-vessel flow paths from cold to hot legs, and from cold legs to the inlet of fuel assemblies,
- Investigate the azimuthal shift (rotation) of loop flows from cold legs to the core inlet, and
- Provide accurate data about the evolution of cold and hot leg temperatures during the transient phase of the test for comparison with the predictions, and
- Identify the modelling issues with the highest impact on the CFD-simulation's results.

2.3 Measured data

The measured data e.g. mass flow rates, coolant temperature of the cold/hot legs, pressure drops along the core and loops, etc. are given in [2]. Hence, it will not be repeated here.

3 Short description of the used CFD Codes

3.1 STAR CCM+ (FRAMATOME, UPISA)

STAR-CCM+ code is a commercial and industrial code of fluid mechanics: it is a three-dimensional finite volume thermal-hydraulic code, which solves the general equations of the fluid dynamics (i.e. continuity, momentum, energy) by using numerical methods and turbulence models on complex unstructured meshes. It is developed and distributed by SIEMENS PLM [3]. The code is fully parallelized allowing good performances on large numbers of CPU. More than a single CFD solver, STAR-CCM+ is an entire engineering tool from the pre-processing, to the solving and post-processing of the solution. The code can deal with multi-physics and can handle and couple several kinds of solvers. It provides a suite of integrated components that can address a wide variety of modelling needs. These components include the following modelling bricks:

- 3D-CAD modeller;
- CAD embedding;
- Surface preparation tools;
- Automatic meshing technology;
- Physics modelling;
- Turbulence modelling;
- Post-processing;
- CAE Integration.

It is a commercial code with industrial character as:

- It covers a large field of applications (hydrodynamics, aerodynamics, combustion, rotative machines, etc.),
- It integrates a fine physical modelling of the flow (single-phase, multi-phase flow, heat transfer, reactive flow),
- It presents reliable and successful numerical methods in terms of robustness, accuracy, memory, and calculation time.

STAR-CCM+ code allows calculating:

- In the multidimensional space (3D);
- In single-phase, laminar or turbulent flows:
 - in steady-state or transient conditions;
 - isothermal or with consideration of the temperature;
 - with or without conjugate heat transfer with a solid;
 - with constant or variable properties of fluid;
 - with or without buoyancy effects;
 - with possibility of source terms;
- Incompressible, dilatable ($\rho=f(T)$) or compressible flows ($\rho=f(P)$);
- Different models of turbulence:

- RANS type models (Reynolds Average Navier-Stokes equations) with two equations (typically, the k - ϵ Realizable model) based on a Boussinesq approximation involving the concept of turbulent viscosity;
- More complex RANS-type models of the RSM type (Reynolds Stress Models) consisting of solving the 6 components of the Reynolds tensors;
- Even finer models, of the DES (Detached Eddy Simulation) or LES (Large Eddy Simulation) type, for the simulation of large-scale turbulence.

Thus, STAR-CCM+ code allows estimating the parameters characterizing a flow:

- Hydraulic variables
 - velocity components fields
 - pressure field
 - fluid properties fields
- Turbulent related parameters
 - turbulent kinetic energy, turbulent dissipation rate and turbulent viscosity for Eddy Viscosity Models
 - Reynolds Stress components and turbulent dissipation rate for Reynolds Stress modelling
 - Turbulent viscosity for Large Eddy Simulation
- Thermal variables
 - temperature field in the fluid and in the solid
 - heat flux
 - temperature at the interface between fluid and solid (so-called “wall temperature”)
- Transported variables
 - species or scalar mass fractions
 - species or scalar fluxes
- Hydraulic loads on walls with a decomposition between the shear force and the pressure related one.

3.2 ANSYS/FLUENT 2019/R3 (ENERGORISK)

3.2.1 Fundamental foundations

The ANSYS Fluent code is used to solve the governing equation of the incompressible fluid flow and heat transfer processes, including the continuity, momentum conservation and heat conservation equations. The purpose of the computational fluid dynamic is the representation of a part of a real physical system, limited by a mathematically calculated discrete mesh and boundary conditions in such a way that does not distort the behaviour of the real system – the preservation of the fundamental fluid mechanics principles [4], [5]:

- Conservation of mass (mass balance, continuity of the fluid space);
- Newton’s second law of motion (balance of the moments of inertia);
- First law of thermodynamics (heat energy balance, heat energy conservation);
- Second law of thermodynamics (heat energy balance).

Computational fluid dynamics is, in part, the method of replacing the governing partial differential equations of fluid flow with numbers, and advancing these numbers in space and/or time to obtain a final numerical description of the complete flow field of interest [5]. The product of CFD is indeed a collection of numbers, in contrast to a closed-form analytical solution that is, the CFD provides an indirect representation of the problem. However, in the end the objective of most engineering applied analyses, closed form or otherwise, is a quantitative description of the problem, i.e. numbers [6]. This approach to applied problems also applies to research of the RPV mixing phenomena with use of the CFD methods.

3.2.2 Turbulence modelling

Thus, based on the preservation of the fundamental principles of fluid mechanics, as well as on the applied aspects of engineering evaluation of the problem with the use of CFD methods (ANSYS Fluent code), the following principles, assumptions of the RPV mixing problem are formulated:

- CFD model based on RANS approach,

- RANS approach is correct for applied problems of industrial use, especially taking into account the large scale aspect of computational analysis,
- Considered RANS SST k- ω turbulence model with “scalable” wall treatment,
- The selected turbulence model is proven by both own and general engineering practice to solve a wide range of industrial problems related to the phenomenology of flow mixing, vortex separation and twisting, multidirectional flows with medium and high Reynolds number (characteristic phenomenology of the flow for the RPV mixing quasi-stationary and transient problems),
- “scalable” wall treatment provides sufficient solution accuracy and stable solver convergence in the case of mixed (different element types) and coarse meshes, when it is impossible to clearly adhere to the desired criterion for a dimensionless number y^+ ,
- The buoyancy effects are not taken into account, owing to the high Reynolds number and lack of conditions for the formation of the contour of natural circulation.

3.2.3 Solution methods

The pressure-based solver of FLUENT-code is using. In the pressure-based approach the pressure field is extracted by solving a pressure or pressure correction equation, which is obtained by manipulating continuity and momentum equations – the pressure equation is derived from the continuity and the momentum equations in such a way that the velocity field, corrected by the pressure, satisfies the continuity. The ANSYS Fluent is solving the governing integral equations for the conservation of mass and momentum, and for energy and other scalars such as turbulence. In all cases, a control-volume-based technique is used that consists of [4]:

- Division of the domain into discrete control volumes using a computational mesh;
- Integration of the governing equations on the individual control volumes to construct algebraic equations for the discrete dependent variables such as velocities, pressure, temperature, and conserved scalars;
- Linearization of the discretized equations and solution of the resultant linear equation system to yield updated values of the dependent variables.

Solver methods in the case of steady-state solver run [4]:

- Coupled pressure-velocity coupling scheme; this algorithm solves a coupled system of equations comprising the momentum equations and the pressure-based continuity equation;
- 2nd order upwind resolution discretization schemes for momentum and energy equations; this scheme of multidimensional linear reconstruction approach is used when second-order accuracy is desired; in this approach, higher-order accuracy is achieved at cell faces through a Taylor series expansion of the cell-centred solution about the cell centroid;
- 1st order upwind resolution discretization schemes for turbulent kinetic energy and dissipation rate equations; this scheme is used when 1st order accuracy is desired; quantities at cell faces are determined by assuming that the cell centre values of any field variable represent a cell-average value and hold throughout the entire cell, the face quantities are identical to the cell quantities;
- Pseudo transient option is activating; the pseudo transient under-relaxation method is a form of implicit under-relaxation; default values of the pseudo transient explicit relaxation factors is used.

Solver methods in the case of transient solver run [4]:

- SIMPLE pressure-velocity coupling scheme; the SIMPLE segregated algorithm uses a relationship between velocity and pressure corrections to enforce mass conservation and to obtain the pressure field;
- 2nd order upwind resolution discretization schemes for momentum and energy equations;
- 1st order upwind resolution discretization schemes for turbulent kinetic energy and dissipation rate equations;
- Default values of the under-relaxation factors is used.

3.2.4 Porous medium and mixing coefficients modelling

Flow through porous media (fuel cassettes model) is modelled by adding an extra source term to the standard flow equations (Navier-Stokes equation) by using the Forchheimer equation. In order to define the properties of the core porous zone, the viscous resistance coefficients and inertial resistance coefficient are obtained.

To estimate the mixing coefficients, additional variables are introduced based on the passive scalars of the fluid transport equation. Despite the introduction of several recent novel approaches, the Fickian diffusion assumption based on turbulent diffusivity remains the most widely-applied framework to study the transport of a scalar in a turbulent flow. The assumption of the standard gradient diffusion hypothesis requires the estimation of the turbulent Schmidt number. This parameter is defined as the ratio of momentum diffusivity to mass diffusivity in a turbulent flow.

3.3 ANSYS CFX (KIT)

ANSYS CFX [7] is a general-purpose high-performance computational fluid dynamics program that is used to solve complex wide range fluid problems for over two decades now. At the heart of the ANSYS CFX is its innovative solver technology that is the main driving force to achieve highly reliable and accurate results in a much more efficient manner as compared to other CFD solvers. The main advantages of CFX are the numerical robustness of the code in terms of poor mesh quality and the fast convergence mainly in case of single-phase flow and steady state simulations. In Germany, CFX is widely used for nuclear engineering research as reference CFD code. It has to be noted that CFX and Fluent are implemented in the ANSYS software bundle and a wide range of physical models is similar in both tools.

CFX provides key physical models for radiation and heat transfer (also conjugate heat transfer), turbulence modelling, combustion and multiphase flow. In case of simulation and processing for rotating machinery, CFX is a global leader for industrial applications.

3.3.1 Turbulence modelling:

Most of the industrial flows are turbulent, therefore several common RANS (**R**eynolds **A**veraged **N**avier **S**tokes) models are provided such as SST, Reynolds-Stress models, k-epsilon and k-omega. For more expensive LES (**L**arge **E**ddy **S**imulation) a Smagorinsky and Wale model can be used. Also hybrid LES models – a blending between URANS and LES dependent on the local mesh scales – in terms of so called detached eddy models are implemented.

3.3.2 Porous media models:

For nuclear engineering, porous media models are essential for modelling the reactor core or perforated structures. In the version ANSYS CFX 2020 R2 in porous regions a fluid and solid part with possible heat transfer between the components is considered. Source terms for energy can be specified for both components combined with several pressure loss models for the fluid part.

3.3.3 Meshing:

All types of unstructured and structured meshes are supported. Polyhedral meshes are presently not supported. CFX is able to re-organize a mesh in terms of improving the mesh quality because of poor angles or non-optimal aspect ratio. As consequence, also simulations with non-optimal mesh quality may lead to acceptable results.

3.3.4 Material properties:

A data basis for a wide range of materials is provided. In case of the present project, IAPWS water data can be used. The user has the possibility to create his own model with temperature and pressure dependent properties.

3.4 TrioCFD (CEA)

TrioCFD [8] is a general CFD code based on the TRUST platform [9]. The code is developed at CEA-Saclay and has been especially designed for turbulent flows in complex geometries. The platform independent code is based on an object oriented, intrinsically parallel approach and is coded in C++. The flexible code structure allows the user to choose a suitable discretization method and to combine various appropriate physical models. Several convection and time marching schemes as well as wide range of boundary conditions are available.

3.4.1 Conservation Equations

The Reynolds averaging procedure is applied on the instantaneous velocity u , which is decomposed into a statistical mean value \bar{u} and a fluctuating component u' . Using the Einstein notation, the mean velocity is determined by the equations of mass conservation (eq.(1)) and momentum conservation (eq.(2)) [10]. Thermal effects are neglected in the momentum equations, as the local Reynolds numbers are very high. External forces are taken into account by the momentum source term $F_{m,i}$.

$$\frac{\partial \bar{u}_j}{\partial x_j} = 0 \quad , \quad (1)$$

$$\frac{\partial \bar{u}_i}{\partial t} + \frac{\partial (\bar{u}_i \bar{u}_j)}{\partial x_j} = -\frac{\partial \bar{p}}{\rho \partial x_i} + \frac{\partial}{\partial x_j} \left[\nu \left(\frac{\partial \bar{u}_i}{\partial x_j} + \frac{\partial \bar{u}_j}{\partial x_i} \right) - \bar{\tau}_{ij} \right] + F_{m,i} \quad , \quad (2)$$

Applying the Boussinesq hypothesis, the Reynolds stress tensor τ_{ij} is defined according to eq.(3):

$$\bar{\tau}_{ij} \equiv -\overline{u'_i u'_j} = \nu_t \left(\frac{\partial \bar{u}_i}{\partial x_j} + \frac{\partial \bar{u}_j}{\partial x_i} \right) - \frac{2}{3\rho} k \delta_{ij} \quad (3)$$

Eq.(4) describes the conservation of energy.

$$\frac{\partial \bar{T}}{\partial t} + \bar{u}_j \frac{\partial \bar{T}}{\partial x_j} = \frac{\partial}{\partial x_j} \left[\left(\frac{\lambda}{\rho r} + \frac{\lambda_t}{\rho r_t} \right) \frac{\partial \bar{T}}{\partial x_j} \right] + F_e \quad . \quad (4)$$

The following formulation of the k- ϵ model is used (Pope, 2000) to evaluate the turbulent viscosity ν_t :

$$\frac{\partial k}{\partial t} + \frac{\partial (\bar{u}_j k)}{\partial x_j} = \frac{\partial}{\partial x_j} \left[\left(\frac{\mu}{\rho} + \frac{\mu_t}{\rho \sigma_k} \right) \frac{\partial k}{\partial x_j} \right] - \epsilon + P \quad , \quad (5)$$

$$\frac{\partial \epsilon}{\partial t} + \frac{\partial (\bar{u}_j \epsilon)}{\partial x_j} = \frac{\partial}{\partial x_j} \left[\left(\frac{\mu}{\rho} + \frac{\mu_t}{\rho \sigma_\epsilon} \right) \frac{\partial \epsilon}{\partial x_j} \right] + C_{\epsilon 1} P \frac{\epsilon}{k} - C_{\epsilon 2} \frac{\epsilon^2}{k} \quad (6)$$

$$\text{with} \quad \nu_t = c_\mu \frac{k^2}{\epsilon} \quad \text{and} \quad P = -\overline{u'_i u'_j} \frac{\partial \bar{u}_i}{\partial x_j}$$

The Reynolds stresses $\overline{u'_i u'_j}$ in the production term P are calculated from eq.(3). The following empirical coefficients are used: $c_\mu = 0.09$, $\sigma_k = 1$, $\sigma_\epsilon = 1.3$, $C_{\epsilon 1} = 1.44$ and $C_{\epsilon 2} = 1.92$.

At inflow faces, Dirichlet boundary conditions with imposed velocity are used. In this context, k and ϵ were calculated from a spatial mean velocity $|U_m|$ and a hydraulic diameter d_h , assuming a turbulence level of 10 % ($u' = 0.1 \cdot |U_m|$):

$$k = \frac{1}{2} \cdot (u')^2, \quad \epsilon = \frac{c_\mu^{3/4} \cdot k^{3/2}}{d_h} \quad (7)$$

At outflow faces, Neumann boundary conditions with imposed pressure are used.

Non-slip walls enclose the calculation domain. Wall functions are used to model momentum exchange between walls and fluid. Here, the general wall law of Reichardt [11] is applied that spans with one correlation the three sublayers of viscous-, buffer- and logarithmic law region ($\kappa=0.415$). The correlation is written for the non-dimensional velocity U^+ :

$$U^+ = \frac{U}{U_\tau} = \frac{1}{\kappa} \cdot \ln(1 + \kappa \cdot y^+) + 7.44 \cdot \left(1 - e^{(-y^+/11)} - \frac{y^+}{11} e^{(-y^+/3)} \right) \quad (8)$$

U_τ and y^+ are friction velocity and non-dimensional wall distance, respectively. Definitions of all non-dimensional quantities can be found in [10]. Local equilibrium between production and dissipation of turbulent kinetic energy is assumed at the first near wall calculation point. The following boundary conditions for k and ε are derived from Reichardt's wall law (eq. (8)). The functions are written in non-dimensional form:

$$k^+ = \frac{k}{U_\tau^2} = 0.07 \cdot y^{+2} \cdot e^{\left(-\frac{y^+}{9}\right)} + \frac{1}{\sqrt{c_\mu}} \left(1 - e^{\left(-\frac{y^+}{20}\right)}\right)^2 \quad (9)$$

$$\varepsilon^+ = \frac{\varepsilon}{\nu U_\tau^4} = \frac{1}{\kappa \cdot (y^{+2} + 15^4)^{\frac{1}{4}}} \quad (10)$$

3.4.2 Discretization

In TrioCFD, the conservation equations can be discretized on unstructured, tetrahedral grids by using a finite volume based finite element method (Finite Volume Elements, VEF). The discretization is an extension of the classical Crouzeix–Raviart element [12], where the main vector unknowns (velocity) and scalar unknowns (temperature, k , ε and concentration) are located in the centre of the faces of an element whereas the pressure is discretized in both the centre and the vertices of the element. This staggered mesh arrangement is P1-non-conforming for velocity and scalars then P0-P1 for the pressure.

3.4.3 Solution Method

After discretization, a system of non-linear algebraic equations is obtained, whose unknowns are the discrete physical variables. An implicit, mass-conserving time marching scheme is used. Temporal integration of Navier-Stokes equations is done with a fractional steps method [13]:

1. A Reynolds averaged, non-divergence free velocity field \vec{u}^* is calculated with the linear system solver GMRES. The convection term is linearized. In vector notation this leads for eq.(2) to:

$$\frac{\vec{u}^* - \vec{u}^t}{\Delta t} = -\frac{1}{\rho} \nabla p^n + \nabla \cdot [(\nu + \nu_t) \cdot (\nabla \vec{u}^* + \nabla^T \vec{u}^*)] - \nabla \cdot (\vec{u}^n \vec{u}^*) + \vec{F}_m \quad , \quad (11)$$

2. The intermediate velocity field \vec{u}^* is then projected by the pressure solver with the conjugated gradient method into a divergence free space by introducing the increment δp :

$$\delta p = p^{n+1} - p^n \quad , \quad \Delta \delta P = \nabla \cdot \vec{u}^* \quad , \quad \vec{u}^{n+1} = \vec{u}^* - \frac{\Delta \delta P}{\Delta t} \quad (12)$$

4 CFD RPV and Core models

4.1 FRAMATOME Model of the RPV and Core (Star-CCM+)

The model is built with STAR-CCM+ v.2021.3.

4.1.1 Geometry

The geometry represented in the model is of the primary vessel. It spans from the cold legs, through the downcomer, the core and the upper plenum to the hot legs. The domain used in the calculation is shown on the **Figure 1**. Only the downcomer and the perforated elliptical bottom of the core barrel have an explicit representation. The core geometry is simplified (in orange on the **Figure 1**): each assembly is modelled by a porous medium, thus the spacing grids and the fuel rods are not explicitly represented. Similarly, the basket enclosing the core, the plates in the upper plenum, the shielding block tube and the grid in the vessel before

the hot legs are treated as porous media (in grey on the **Figure 1**). The holes in the support columns are not explicitly represented either, a head loss coefficient is used to model their influence on the flow. There is no circulation in the spacer ring between the cold legs and the hot legs, the whole flow must go through the downcomer.

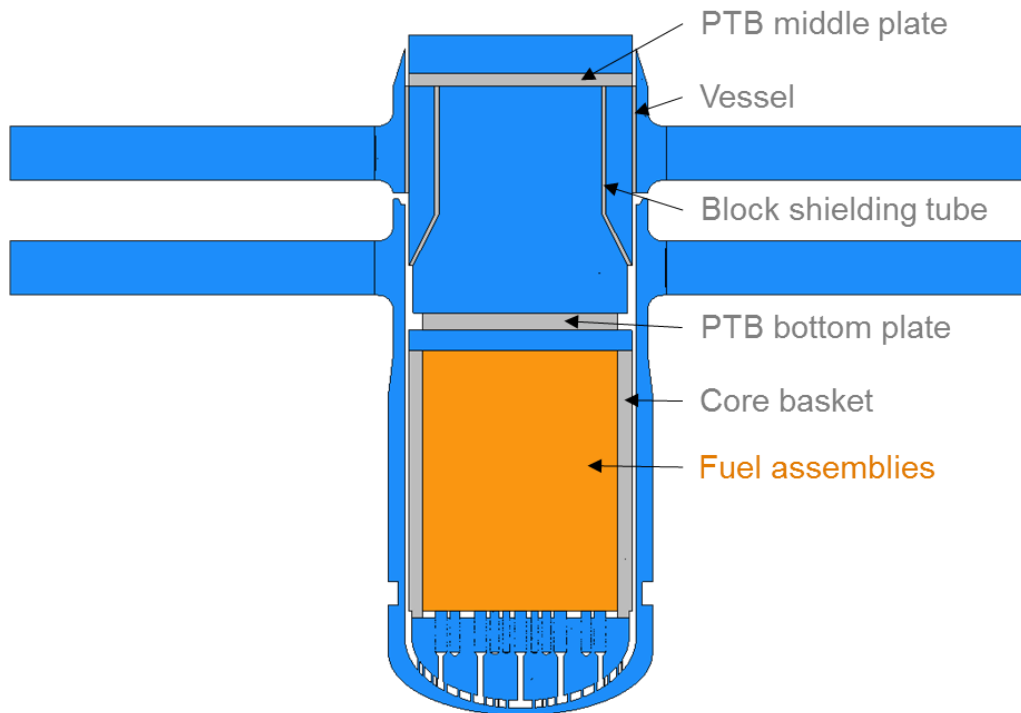


Figure 1: Overview of the geometry

4.1.2 Meshing

The mesh is made with an automated mesh of polyhedral cells and contains approximately 48 million cells, except for the assemblies, which are made with a directed mesh of polygon cells. The base size is 0.08 m with a minimal target of 0.008 m and the prism layer total thickness is around 0.04m. The perforated elliptical bottom of the core barrel is refined to improve mixing flow. An overview of the mesh is given on **Figure 2**.

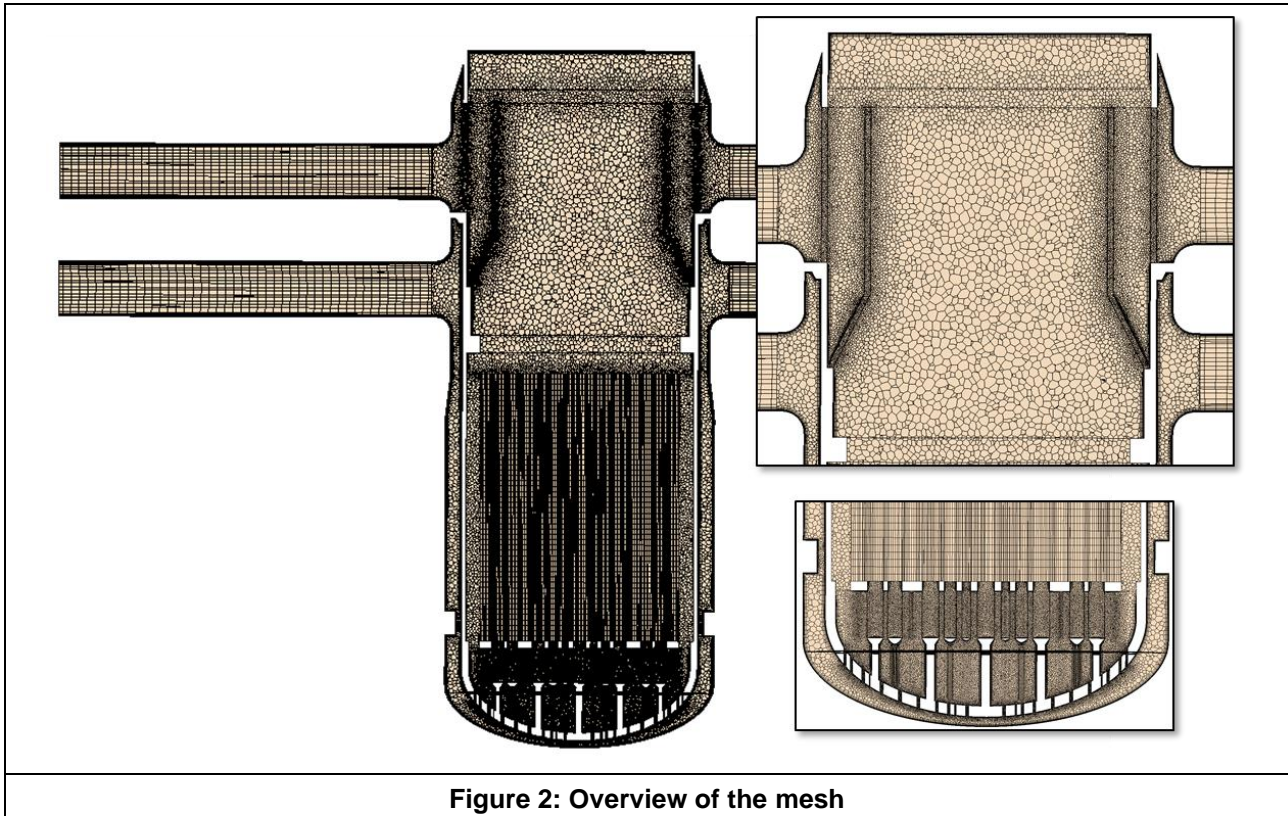


Figure 2: Overview of the mesh

4.1.3 Boundary conditions

At initial state, the thermal power of 281 MW was about 9.36% of the nominal power. With 15.59 MPa, the pressure above the core was close to the nominal value of 15.7 MPa. The coolant temperature at the reactor inlet was 268.6 °C, about 20 °C lower than the nominal value. The bypass flow through the core is about 2.9% of the total reactor mass flow rate. A mass flow inlet condition is set on the cold legs with a fluid temperature defined in **Table 1** and **Figure 3**. The turbulence intensity is 1% and viscosity ratio about 10 in each cold legs (no swirl component). On the hot legs, a pressure outlet condition is applied. The stabilized state at 1800 s is considered as final state. The experimental measured core outlet temperature distribution is shown on **Figure 4**.

Table 1: Initial and final parameters

Parameters	Initial state at 9.36%PN, before closing SIV-1	Final stabilized state, SIV-1 closed
Core power (MW)	281	286
Reactor inlet pressure (MPa)	15.97	15.97
Reactor outlet pressure (MPa)	15.55	15.55
Reactor mass flow rate (kg/s)	18971	18730
Mass flow rate 1 (kg/s)	4737	4566
Mass flow rate 2 (kg/s)	4718	4676
Mass flow rate 3 (kg/s)	4682	4669
Mass flow rate 4 (kg/s)	4834	4819

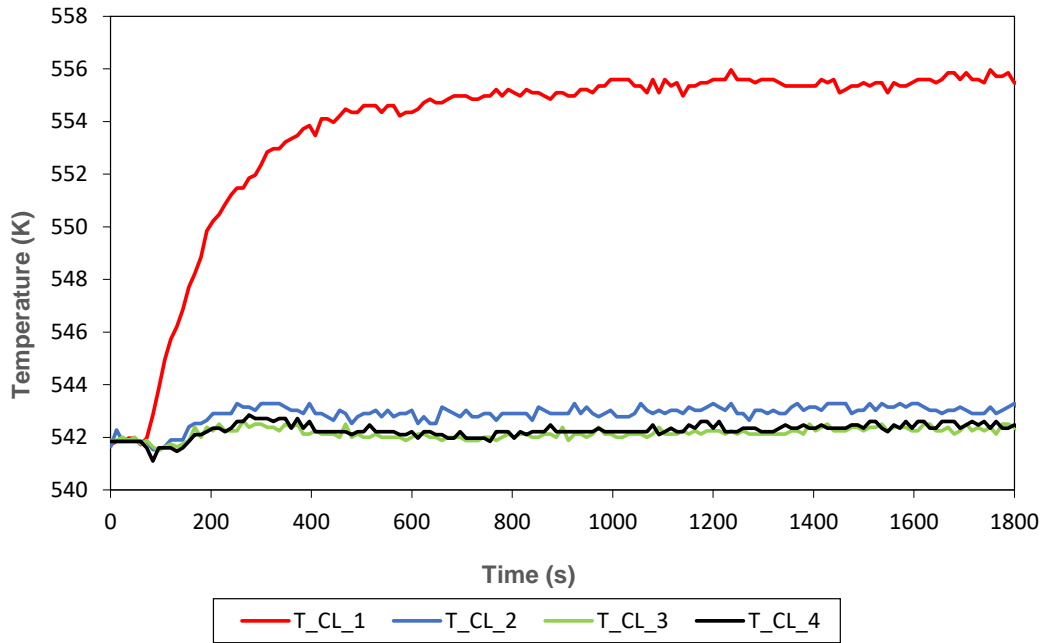


Figure 3: Cold leg experimental temperatures

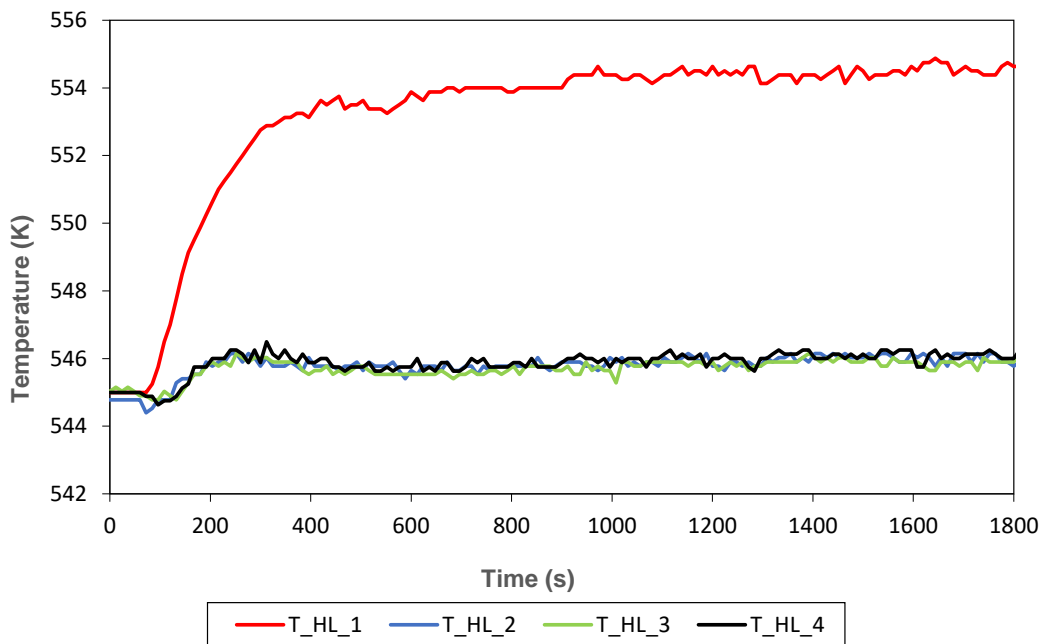


Figure 4: Hot leg experimental temperatures

4.1.4 Head loss coefficients

Head loss coefficients are applied at the following locations to regulate either the mass flow or the head variation:

- In the core basket to control the by-pass of the core, with a porosity of 5%;
- In the support columns to set the head loss through the orifices, with a porosity of 17%;
- In the core to account for the grids (axially) and the rod bundles (horizontally), with a porosity of 46%;
- Through the base plate of the block shielding tube, with a porosity of 40%;

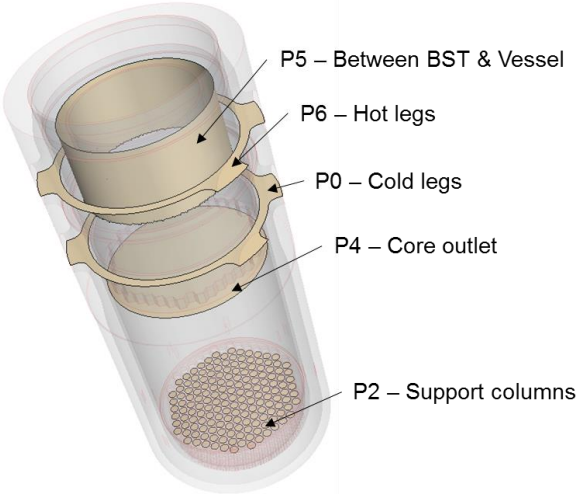
- Through the block shielding tube, with a porosity of 56%;
- Through the vessel before the hot legs, with a porosity of 33%.

The mass flow of the core bypass amounts 2.9% of the total mass flow delivered by the pumps.

The head loss coefficients are adjusted to fit the following **Table 2** pressure drop:

Table 2: Pressure drop in the vessel

Zone	ΔP experimental measurement [MPa]	ΔP CFD [MPa]
P0 - P2	0.1971	0.232
P2 - P4	0.1422	0.154
P4 - P5	0.0284	0.03399
P4 - P6	0.0363	0.05768
P0 - P6	0.376	0.448



The pressures are measured as follows:

- P0 is in a horizontal section of the downcomer, the altitude corresponds to the centre of the cold legs;
- P2 is in a horizontal section of the support columns;
- P4 is above the core, before the bottom plate of the BST;
- P5 is a radial section of the upper plenum between the BST and the vessel;
- P6 is in a horizontal section whose altitude matches the centre of the hot legs.

4.1.5 Numerical parameters

The fluid solver used for the calculation is a segregated steady RANS model, with 2ndorder spatial schemes. The turbulence model used is K-epsilon Realizable Two-Layer with a two-Layer all Y+ wall treatment. The thermal solver is a segregated one with 2ndorder schemes too.

The solver is set to Implicit Unsteady, with a second order Temporal Discretization. The time-step is 0.1 s with a convergence criterion of 20 inner iterations.

The following properties of water are used, with T_c the temperature in °C:

Density [kg/m³]	$3573.393 - 28.26898 * T_c + 0.1004155 * T_c^2 - 1.260181 \times 10^{-4} * T_c^3$
Specific heat [J/(K*kg)]	$1212344.0 - 17044.71 * T_c + 90.04235 * T_c^2 - 0.2111469 * T_c^3 + 1.856398 \times 10^{-4} * T_c^4$
Thermal conductivity [W/(K*m)]	$0.329343 + 0.00344348 * T_c - 8.8837710^{-6} * T_c^2$
Dynamic viscosity [Pa*s]	$6.654779 \times 10^{-4} - 5.107215 \times 10^{-6} * T_c + 1.611641 \times 10^{-8} * T_c^2 - 1.83385 \times 10^{-11} * T_c^3$

4.2 UNIPI Model (Star-CCM+)

Hereafter the description of the STAR-CCM+ model developed by UPISA is described.

4.2.1 Geometrical specifications

Due to the complexity of the RPV flow path, and in order to simulate the targeted mixing phenomena, a full 3D geometry of the VVER-1000 is developed considering several geometrical simplifications to fit the computational capabilities and reduce the computational cost. The simplifications for the RPV internal structures (see **Figure 5 (a, b)**) are listed as follows and the simplified model is shown in **Figure 5 (c)**:

- 1) Only fluid regions are modelled; some internal structures and solid parts are modelled as porous media.
- 2) The flow bypass from the cold-leg to hot-leg is neglected and consequently the total mass flow at the inlets is reduced by 1% to compensate for the cold-hot legs bypass.
- 3) The core basket water cooling channels are modelled as a whole part connected to the lower plenum with the porous media treatment, to match the 3% core flow bypass corresponding to the actual plant data.
- 4) The perforated parts of the support columns are modelled as porous media interfaces.
- 5) The internal structures of FAs are not modelled explicitly; in fact, no fuel rods, control and instrumentation rods and water channels are modelled. The core region is instead modelled as 163 whole hexagonal FAs adopting again the porous media treatment.
- 6) The upper plenum internal structures are neglected, and the upper plenum zone is modelled as a fluid region, while the effects of the internal structures on the mixing phenomenon are considered to be negligible.
- 7) The perforated shielding tube block is modelled as a porous region to reproduce the plant pressure losses between the exit of the FAs and right before the perforated section of the barrel.
- 8) The perforated section of the barrel is modelled as a porous region to set the plant pressure losses between the exit nozzles and the inside barrel.
- 9) The two connection nozzles for the pressure safety injection system are neglected.

As a result of the geometrical simplifications mentioned earlier, the modelled domain consists of the 7 regions shown in **Figure 5 (c)**. Six porous regions are modelled due to the simplifications ahead prescribed; they are labelled in red (i.e., core) and orange (i.e., core basket, upper core support plate, shielding tube shroud, perforated section of the barrel and the upper plate) colours in **Figure 5 (c)**, while the blue colour represents a single region modelled as fluid. Thanks to the introduction of these porous media, the heat transfer processes between solid and fluid can be taken into consideration via thermal non-equilibrium model, as well as reproducing the plant pressure losses through setting the porous resistance parameters not only in the stream wise direction but also in the radial and circumferential ones. All the considered assumptions contributed to reduce the total mesh element count and consequently reduce the computational time.

The porosity settings for the different regions have been based on the geometrical characteristics and properties and have been based on the ratio of the surface area of the solid and fluid. The porosity setting in the core region is set to be 0.55, in the perforated fuel assembly support column is set to be 0.25, in the perforated section of the barrel is set to be 0.40 and in the perforated section of the shielding tube block as well as both upper core support plate and the upper support plate is assumed to be 0.50.

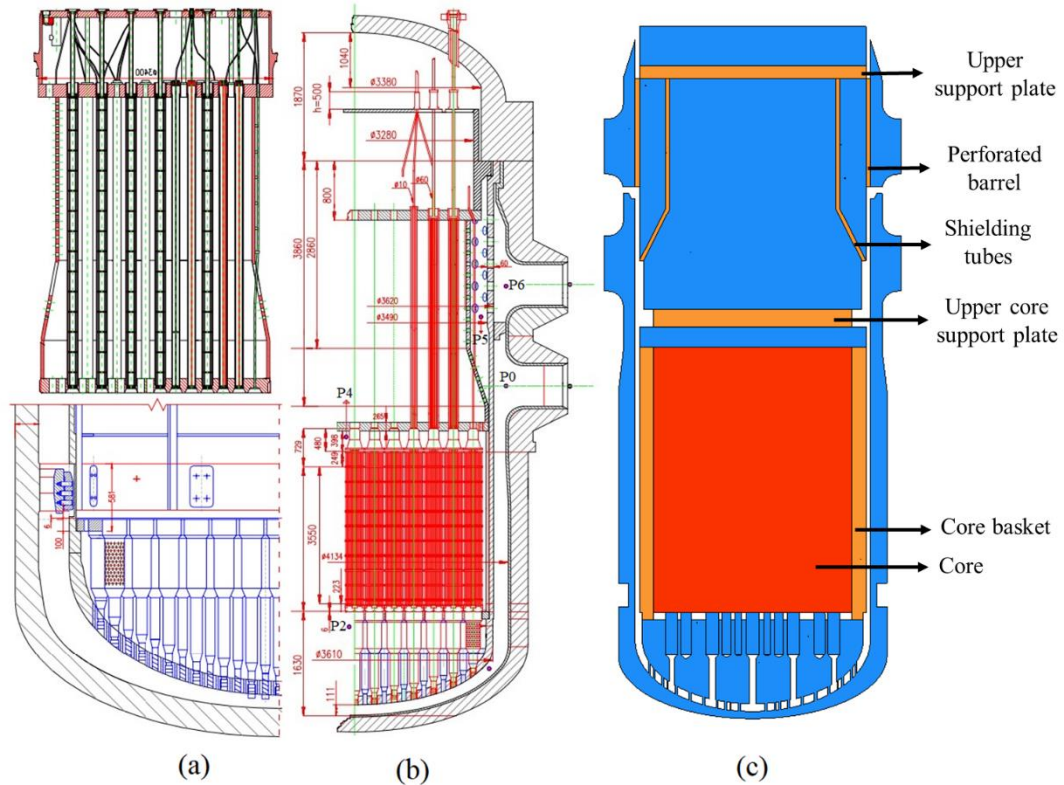


Figure 5: VVER lower plenum (bottom), upper plenum (top): (a), RPV: (b), and Cross-sectional view of VVER vessel model: (c)

4.2.2 Meshing Characteristics

The computational grid of the fluid region is constructed by 24.8 million unstructured polyhedral cells, where 10 prism layers are used to resolve the near wall flow with a stretching factor of 1.5 and a total thickness of 25 mm. The core region contains approximately one million cells, constructed from 50 prismatic cell layers generated from polygonal cells. Eventually, all the porous regions are generated using unstructured polyhedral cells and constructed by 1.8 million cells. Therefore, the full geometry is constructed by a mesh grid of roughly 27.6 million cells: the size of the cells in the computational grid ranges from 20 mm up to 100 mm. It is important to notice that, since neither the fuel pins in the FAs nor the internal structure of the upper plenum is considered in the CAD, additional pressure losses are introduced in the porous regions to reproduce the design pressure losses measured at the positions P0, P2, P4, P5 and P6 as indicated on **Figure 5 (b)**, while operating at nominal conditions.

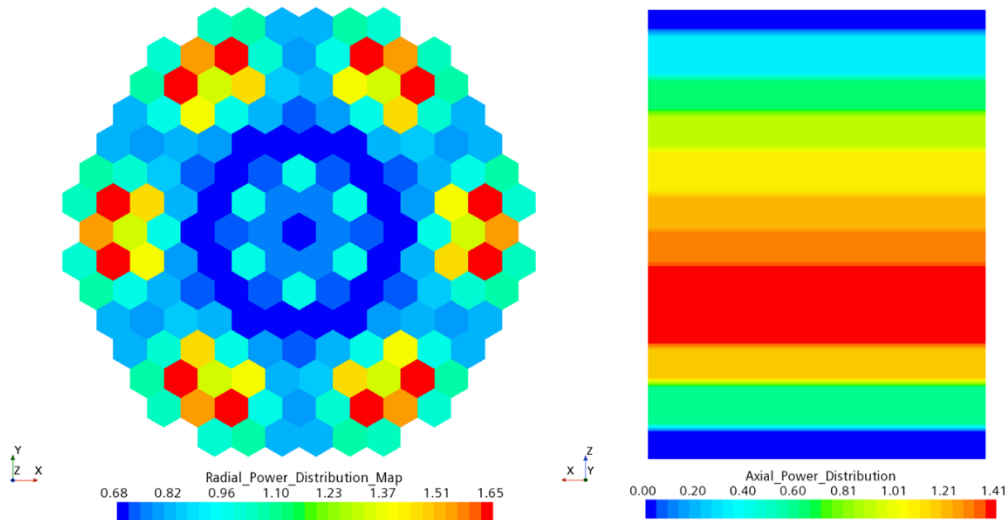
4.2.3 Boundary Conditions

A uniform azimuthal inertial resistance coefficient of a value of 2636 kg/m^4 was used for the core region and 50000 kg/m^4 radial resistance was adopted for the core region. In addition, a uniform azimuthal inertial resistance coefficient of a value of 211202 kg/m^4 was used for the core basket region, to limit the core-bypass mass flow rate close to the range of 3% of the total vessel flowrate at nominal operating conditions. Eventually, an overall isotropic inertial resistance coefficient of 5900 kg/m^4 was used for the upper plenum regions. These porous resistance settings were adjusted for nominal operating conditions and maintained for the transient computations. **Table 1** presents a comparison between the measured pressure at reference locations and the CFD model predictions for nominal steady state conditions and the steady state before the beginning of the transient.

Table 3: Comparison of the predicted pressure losses and plant data.

ΔP	ΔP measured [MPa]	ΔP CFD [MPa] T6.1	ΔP CFD [MPa] T6.2
P0-P2	0.201	0.1955	0.2186
P2-P4	0.142	0.1419	0.1438
P4-P5	0.029	0.0289	0.0315
P4-P6	0.037	0.036	0.0387
P0-P6	0.392	0.371	0.4076

The axial and radial power distribution maps were adopted to impose the internal heat source according to the boundary condition specifications sheet. **Figure 6** shows the radial power distribution map (left) and the axial power distribution (right).


Figure 6: Radial power distribution map (left), Axial power distribution map (right).

In **Table 2**, the initial BC and final BC of the transient are summarized.

Table 4: Initial and final states B.C.

Parameter	BC Initial state	BC Final state
Core power, MW	281	281
Pressure above the core, MPa	15.60	15.58
Cold leg #1 temperature, K	541.72	555.47
Cold leg #2 temperature, K	541.65	543.28
Cold leg #3 temperature, K	541.88	542.38
Cold leg #4 temperature, K	541.85	542.47
Hot leg #1 temperature, K	544.81	556.23
Hot leg #2 temperature, K	544.88	547.20
Hot leg #3 temperature, K	544.91	545.85
Hot leg #4 temperature, K	545.04	546.84
Loop #1 flow rate, kg/s	4689.63	4689.63
Loop #2 flow rate, kg/s	4670.82	4670.82
Loop #3 flow rate, kg/s	4635.18	4635.18
Loop #4 flow rate, kg/s	4785.66	4785.66
Core flow rate, kg/s	18222.95	17992.63
Reactor pressure drop, MPa	0.4076	0.4030
Bypass flow (Core basket), kg/s	559.24	550.97
total mass flow rate at inlets, kg/s	18781.29	18781.29

4.2.4 Numerical Model

The STAR-CCM+ version 16.0 code was used to model the transport phenomenon of the fluid flow and heat transfer processes in the RPV. The thermos-physical properties (density, dynamic viscosity, specific heat capacity and conductivity) of the coolant were introduced as temperature-dependent polynomials at a constant pressure of 15.5 MPa based on NIST REFPROP-V10 database. The inlet boundary condition was set to be a uniform mass flow and the outlet boundary condition was set to be pressure outlet. Static temperatures were imposed at both inlets and outlets according to the plant data. The inlet turbulent settings were: 1% turbulent intensity and 10 viscosity ratio. The boundaries of the flow domain were modelled as adiabatic walls with no-slip conditions. Two-equation based turbulence models were considered to study their capabilities at predicting the mixing phenomenon, the standard $k-\epsilon$ low-Reynolds (Lien et al., 1996) and the SST $k-\omega$ [14] were mainly adopted. Second order convection discretization schemes were used for all transport equations and for all the RANS models adopted in this work. The all y^+ wall treatment was used for near wall flow modelling. The heat transfer processes between solid and fluid in porous regions were modelled via thermal non-equilibrium model and the solid properties were set to be constant at the average temperature of the plant data. Passive tracers were injected at the inlets to quantify the flow mixing at the core exit, as well as the azimuthal shift which occurs in the vessel.

4.3 KIT Model (ANSYS CFX)

Hereafter, the ANSYS CFX model details developed by KIT is described.

4.3.1 General model description

The main problem for the creation of a detailed CFD model for a geometrical high complex technical system like the VVER1000 nuclear pressure vessel is to develop an adequate computational mesh that is able to resolve all relevant flow scales inside the pressure vessel. At a vessel height of about 10m and a diameter larger than 3m, the smallest geometrical relevant scales have 3mm such as the gap width of perforations in the upper part of the core support columns. The coolant reaches locally a maximum speed of nearly 30m/s – while passing through the holes of the elliptical bottom plate - which requires a smallest wall spacing of 0.02mm in order to be close to y^+ values of 100. Fortunately, the Reynolds number is large ($>1e6$), so that values for $y^+ \gg 100$ are acceptable mainly for the computation of pressure losses. For the accurate calculation of heat transfer, the general recommendation is a value of $y^+ \approx 1$, which is impracticable because of limitation of computational resources. For practical reasons, several regions of the pressure vessel are meshed as porous medium: the core, the upper part of the core support columns and nearly the complete part of the upper plenum.

Based on the experiences as former participant of a VVER1000 benchmark by OECD a new mesh was developed by using the provided CAD model by Framatome. The new model uses an updated numerical setup of the old version (from CFX 5.9 in 2009 to ANSYS 2020 R2). The main improvements of the new model are a mesh with partial boundary layer inflation, IAPWS data basis for water properties and improved porous media modelling capabilities. The main disadvantage of the new version is the missing structural resolution in the upper plenum, where control rod guide tubes and several perforated walls are treated now as porous medium (in old model in full resolution), which has disadvantages now in missing mixing properties of the upper plenum.

4.3.2 Description of meshing

For meshing, meshing software by Pointwise is used. Pointwise provides features for semi-automatic boundary layer inflation, which were used intensively for generating the meshes of the new model. **Figure 7** shows both CFD model versions. While the old version represents the upper plenum in full detail, the new version represents here an inner perforated wall as porous region. Several differences in detail modelling are visible. The new model does not take into account the upper core plate, which is resolved in the old version. The core is modelled as porous region by individual resolution of all assemblies, while the old version resolves assemblies as subchannels with empty centre volumes equal to the volume of the fuel pins. For all models between the core and the core barrel, a small bypass channel at gap width of about 25 mm is created. The bypass mass flow of about 2.9% is regulated by the introduction of an additional pressure loss coefficient for this channel. Below the core (red region), nozzle connections between each assembly and the core support plate are modelled in the new version, while this volume is considered as empty space in the old version. The core support plate is fixed by support columns against an elliptical bottom plate, which is finally connected with vessel wall structures. The upper part of the core support columns is perforated by small slots at its outer shells and serves as flow path from the lower plenum into the perforations of the core support plate, see blue and turquoise colour inside **Figure 7**. It is modelled as porous region with adjusted pressure loss coefficients derived from former CFD detail simulations. For the support columns in peripheral location, the loss coefficients plenum (only for the new model version) are fixed to obtain the design pressure drops at nominal steady state conditions [2]. For a more detailed description of the porous region loss coefficients see [15] and [16].

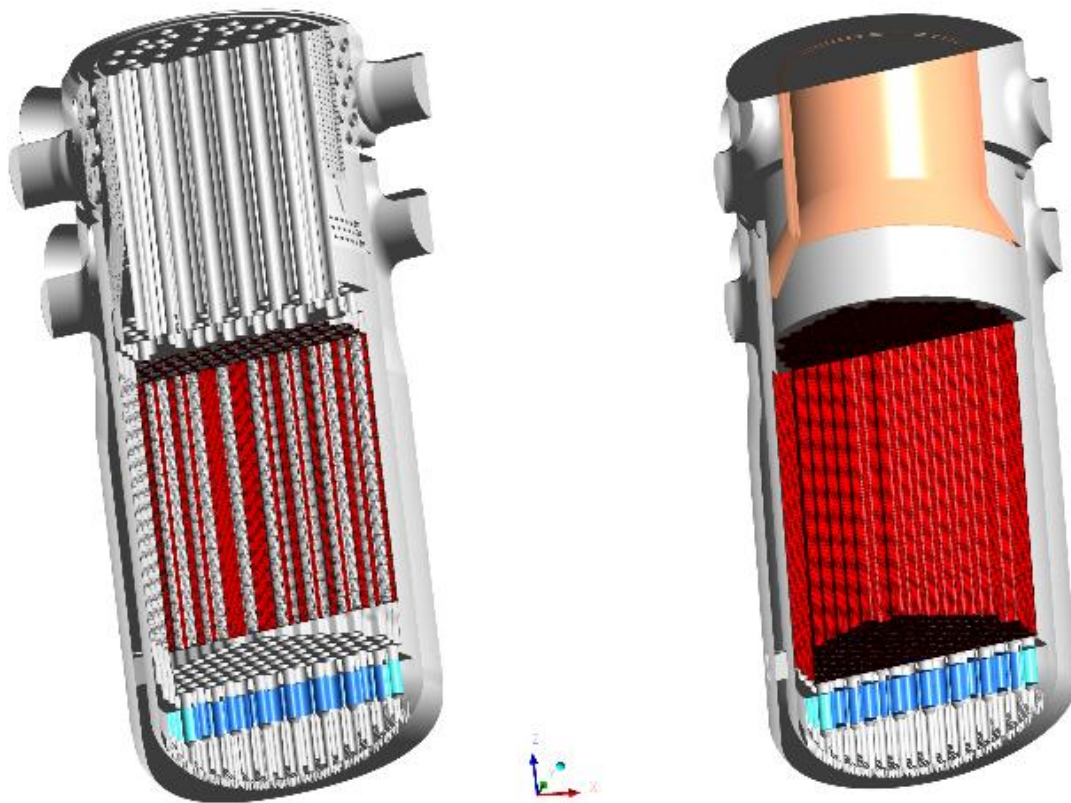


Figure 7: The old (left) and new model version (right)

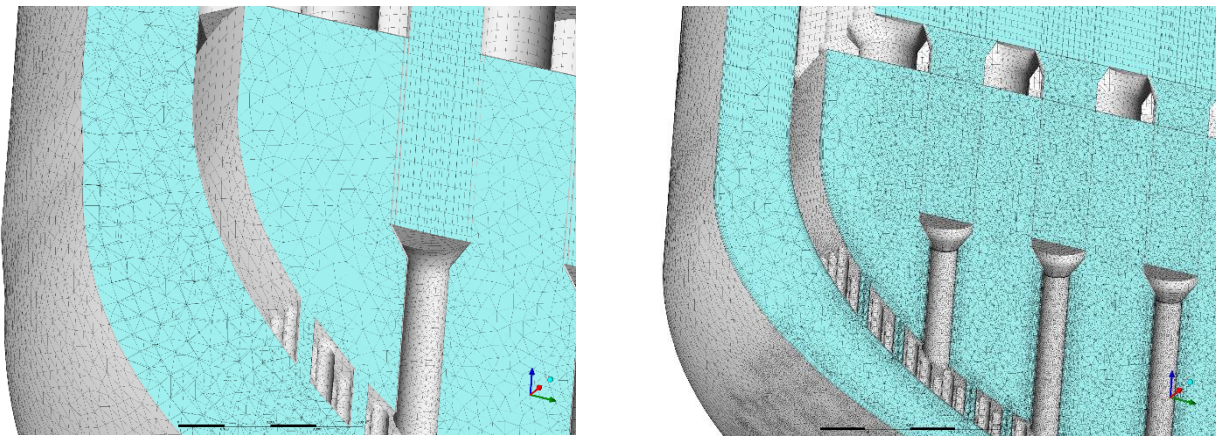


Figure 8: Coarse mesh (V1) and very fine mesh (V3)

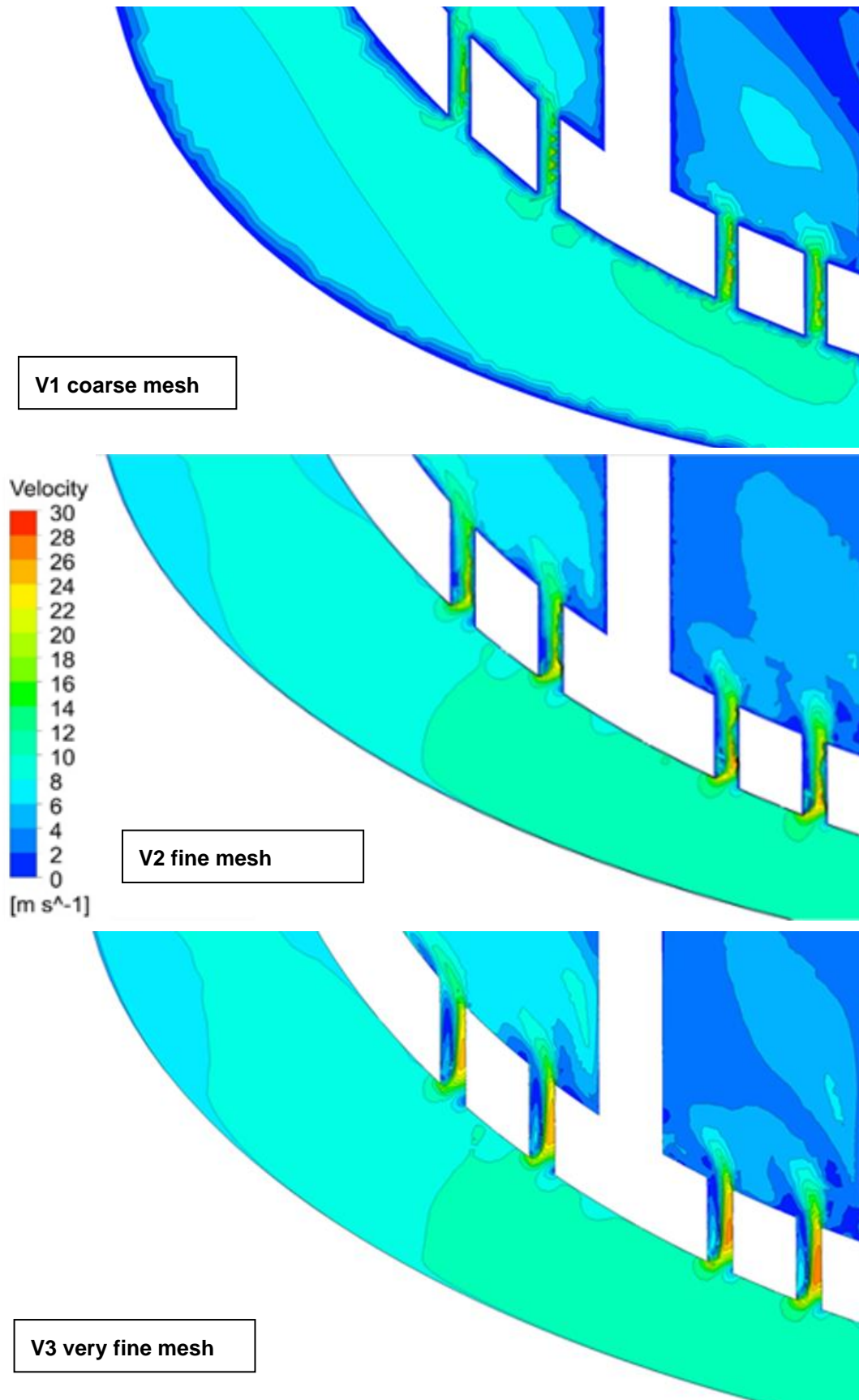


Figure 9: Flow through elliptical bottom plate holes by using different meshes

For all model versions unstructured meshing was used with cell scales from 5-50mm for the old version (V1, 23.8 million cells) and 1-40 mm for the new version (V2, 36.2 million cells) with medium spatial resolution and boundary layer inflation from the inlet nozzles and the downcomer until the entrance holes of the elliptical bottom plate. An additional mesh refinement for the new version model is performed by the extension of boundary inflation through the elliptical bottom plate holes into the lower plenum (V3, 57.6 million cells). **Figure 8** shows a part of the mesh in the lower plenum at the elliptical bottom plate which represents in terms of meshing the most crucial part of the pressure vessel. Local mesh refinements at the outer vessel wall below the holes of the elliptical bottom plate were necessary to generate a smooth transition region between the inflation fronts inside the downcomer. The thickness of the wall closest inflation layer varies between 1mm in the downcomer and 0.25mm inside the bottom plate holes.

Figure 9 shows the influence of the meshes on the flow patterns inside the elliptical bottom plate holes, where the highest flow velocities and highest wall shear stresses inside the vessel are located. The velocity distributions are calculated for steady state normal operation conditions at a total mass flow of 17.583 tons/s, a temperature of 287°C at the inlets and a pressure of 15.6 MPa. The coarse mesh V1 without boundary layer inflation overestimates the boundary layer thickness in the downcomer and is not able to calculate local flow separation inside the holes. For the fine mesh V2, the boundary layers in the downcomer are better resolved and flow separation in the holes is calculated but obviously with some numerical diffusion and numerical noise. The best convergence was obtained with the finest mesh V3, where the separation zones are more stable and better resolved by the mesh. As convergence criteria, the normalized RMS residual values mainly for pressure and velocity components and the global balances for momentum and energy equations are used. For all cases RMS values were slightly higher than 10^{-4} ($1.6 \cdot 10^{-4}$ for V3 and $4 \cdot 10^{-4}$ for V1), while the accuracy for the global balances was $<1\%$ for all cases. Within 200 iterations, convergence for a steady state simulation could be achieved.

All models apply a SST k- ω turbulence model by [14] with a standard 1st order discretization scheme. All other equations are solved with a high order scheme with 1st order in regions with strong gradients and 2nd order in other regions by Barth and Jespersen [17]. The models include the following simplifications:

No solids were considered because of the low heat capacity of steel compared with coolant and lower mass inventory. Steel has a significantly higher thermal conductivity than water, but the energy transport by conduction is negligible against convection. All outer boundaries were assumed as adiabatic because of the large volume-to-surface ratio so that any losses can be neglected. Several design elements were not considered by the mesh such as fuel pins or spacers. In general, the new model versions provide a higher mesh quality, while for the upper plenum the old model is significantly more accurate. First tests have shown that mixing in the upper plenum is calculated as more intensive by the older model and shows significant differences from mixing in a porous media model.

The coolant properties were implemented as temperature and pressure dependent by using the IAPWS water data library in ANSYS.

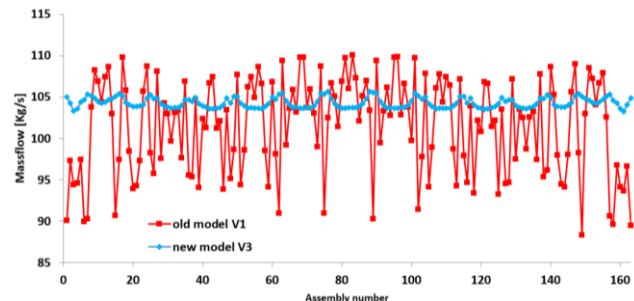
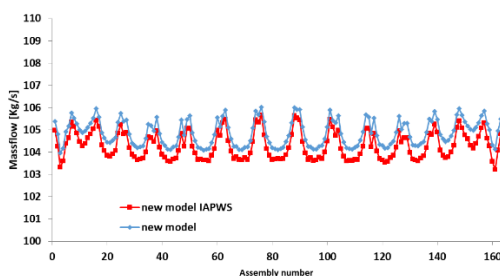


Figure 10: Mass flow distribution at core outlet **Figure 11: Mass flow distribution at core outlet**

Figure 10 shows the influence of different modelling of physical water properties on the mass flow distribution at the core outlet at standard operation conditions. Only temperature dependent physical properties (blue

curve) results in local absolute differences $<0.4\%$ (together with a slight modification of bypass flow). **Figure 11** shows mass flow distributions at nominal operation conditions at the core outlet for the old model and the new model. Both models are using the same IAPWS physical properties but have different meshing concepts mainly in the downcomer and lower plenum. The main difference between V3 and V1 is the significant finer resolution of wall boundaries by prism layers. Concerning the differences caused by meshing (up to 15 %) the deviations caused by different modelling of physical properties are negligible.

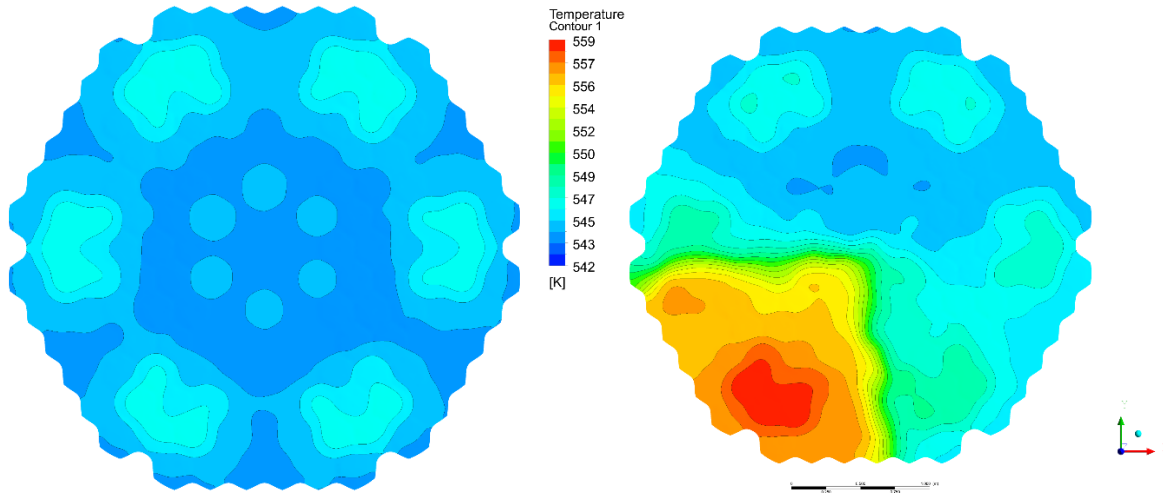


Figure 12: Core outlet temperature of V2 at 0s (left) and at 1800s (right)

In **Figure 12**, the core outlet temperature distributions at initial state and at the end of the transient from model V2 that is finally used for transient calculations are shown. After 1800 s the loop 1 region, that has heated up by 10K, is clearly visible. The lowest assembly temperatures are located in radial peripheral positions, where the assemblies with the lowest power factors are found and a mixing with colder bypass coolant takes place. In general, the temperature patterns at $t=0s$ correlate with the power factor distribution. The hot spot temperatures are located at assemblies with power factors larger than 1.3. The heat and mass exchange between neighbouring assemblies is reducing the temperature differences, but the signature of the power factor distribution is clearly visible at the core outlet.

The numerical accuracy of the new model versions V2 and V3 could be significantly improved against the older V1 version because of advances in meshing technics not implemented in meshing tools available more than a decade ago. By using boundary layer inflation, y^+ values inside the holes of the elliptical bottom plate could be reduced from 30000 in V1 below 1000 for the V3 version. Concerning the computational costs for steady state simulations, the V3 model consumes about 1 day (by 30 CPU's). As previously mentioned, the V2 model is used as a compromise for transient simulations.

4.3.3 Boundary conditions

At the cold leg inlets, transient mass flow and temperature conditions corresponding with plant data given by the benchmark were used. As boundary conditions for turbulence, a medium turbulence level of 5% according to the mean velocity was assumed. Additionally, at all inlets a swirl velocity component in right hand side direction corresponding to the local central axes of the inlet nozzles with a value of 0.15 (see description in previous chapter) was assumed. The value of 0.15 was extracted from a set of previous steady state calculations as optimum value for the calculation of mixing coefficients for loop 1.

At the outlets, a relative pressure of zero Pa was used. Furthermore, transient plant pressure data at a location above the core was used as reference pressure for the calculation of temperature and pressure dependent water properties from the IAPWS water data library. All outer vessel boundaries were considered as adiabatic.

4.3.4 Numerical setup of inlet swirl

Former simulations with a CFD model containing all components of the primary loops indicated a possible impact of pump swirl on coolant mixing. In this model version an additional swirl component at each cold leg inlet was added. The swirl is implemented with axial orientation adjusted to the local inlet nozzle axis, see **Figure 13**. The rotational momentum for each inlet cross section was selected to 15% of the axial momentum at each inlet. The swirl orientation was the same for all inlets. Steady state simulations with various rotational strength from 0% to 30% were performed and differences of mixing coefficients to experimental data in loop 1 were analysed. The best fitting of 15% was used for transient simulations.

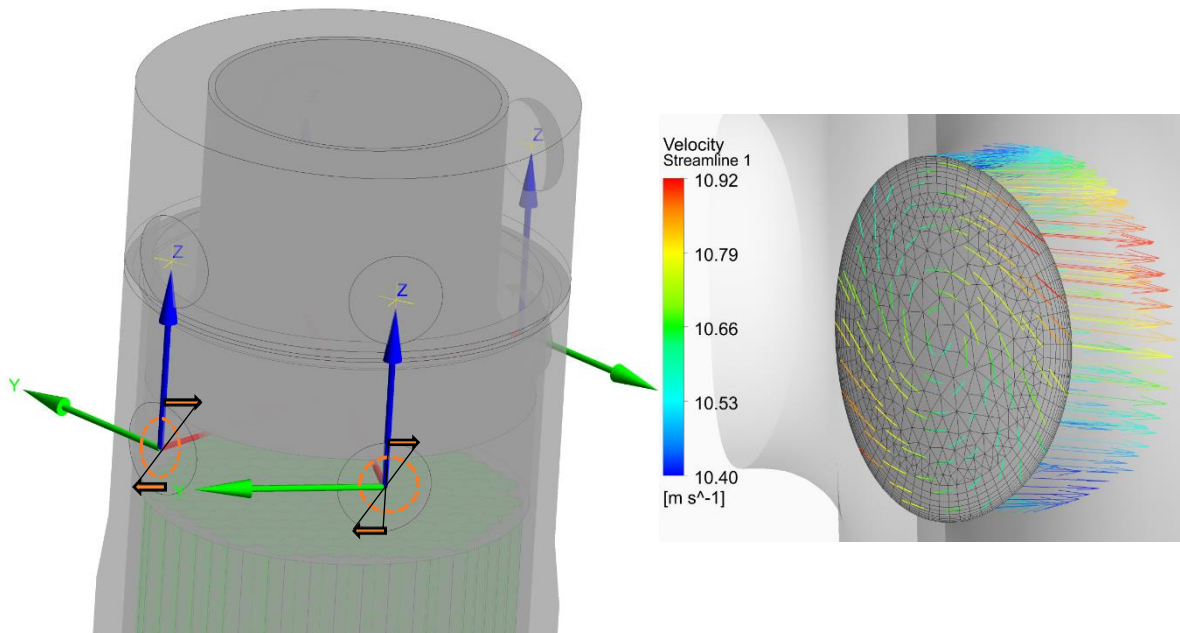


Figure 13: Sketch of inlet swirl boundary condition and the situation at cold leg 1 at $t = 0s$

4.4 CEA Model (TrioCFD)

In this subchapter, the TrioCFD model of the VVER-1000 RPV developed by CEA is described.

4.4.1 Geometry model

From the described CAD model, a tetrahedral mesh of about 32 million elements has been created using the mesh-generator module of the open-source software SALOME, **Figure 14**. A surface mesh was created with the MG CAD-surf algorithm. Finally, the 3D tetrahedral mesh was created using the MG Tetra algorithm **Figure 15**.

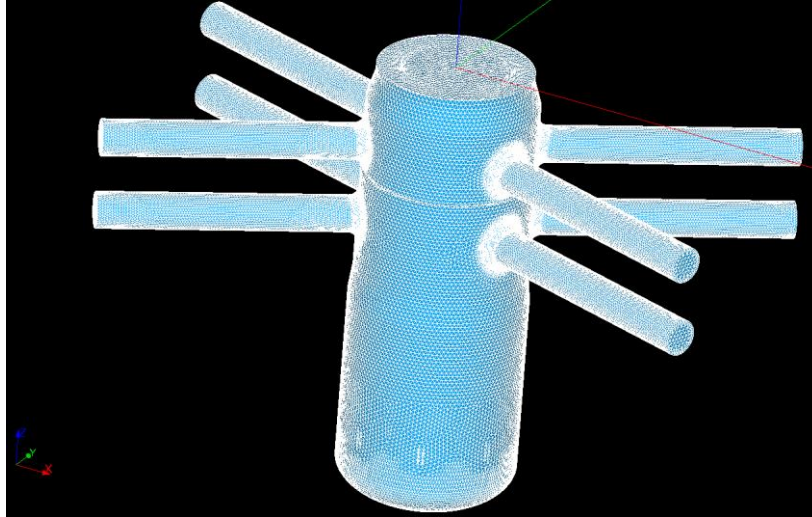


Figure 14: Overview of the mesh used for TrioCFD

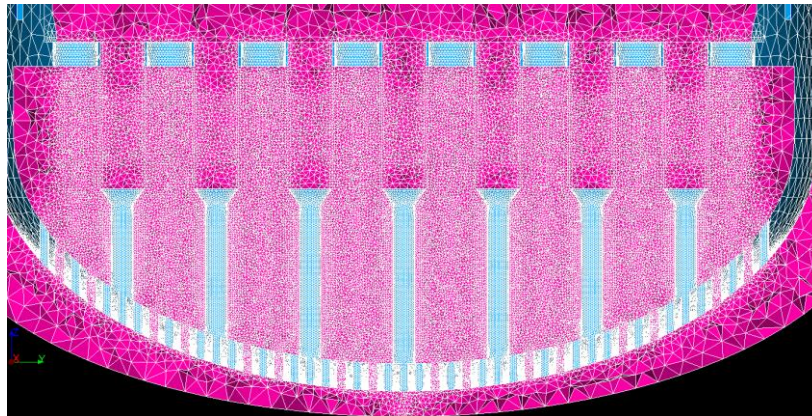


Figure 15: Zoom in the lower plenum of the mesh used for TrioCFD

4.4.2 Modelling of the core region

An explicit resolution of the reactor core is not possible to date. Thus, simplifications were introduced, which lead to a basic porosity modelling of the core region. In the VVER-1000 core, fuel pins block about 46% of the volume. Hence, a homogeneous volume porosity of 0.54 is introduced in the calculation for the core region.

To take into account both axial and transverse pressure losses in fuel assemblies, friction coefficients are used. They are defined by eq. (13). The coefficients, **Table 5**, are used at CEA to estimate the pressure losses

in fuel assemblies of square arrangement; D_h is the hydraulic diameter of a sub-channel and D_e the minimum distance between two fuel rods.

$$C_f = a \cdot Re^{-b} \quad \text{with} \quad Re = \frac{U \cdot D}{\nu} \quad (13)$$

Table 5: Parameters for the pressure loss correlation

Direction	a	b	U	D
Axial	0.316	0.25	$ \bar{u}_a $	D_h
Transverse	4.03	0.27	$ \bar{u}_t $	D_e

These pressure losses are implemented in the Navier-Stokes equations (eq. (2)) as source term $F_{m,i}$.

The core power is taken into account in the energy equation (eq. (4)) by the source term F_e constant in time. An improvement from our modelling for WP6.1 is to implement an axial power profile in the core. The latter is approximated with a 4th order polynomial totalling a core power of 283 MW.

4.4.3 Boundary conditions and Swirl

As suggested by KIT, a way to improve the mixing coefficient results is to include swirl at the cold legs inlets aiming to reproduce the swirl generated by the pumps. In order to evaluate this possibility, we have realized calculations to evaluate the mixing coefficient results without and with swirl at the inlet of the cold leg.

The swirl is modelled by a solid body rotation at the inlet of the cold legs. So let us assume that the normal of each cold leg inlet is through the normed vector \bar{u}_z

- Without swirl, the boundary condition is defined as $\vec{v} = v_0 \bar{u}_z$, with v_0 the velocity associated with the mass flow rate.
- With swirl, the boundary condition is defined as $\vec{v} = v_0 (\bar{u}_z + 0.15 \frac{r}{R} \bar{u}_\theta)$, with r , the radial position, R the cold leg radius and the \bar{u}_θ azimuthal normed vector. The coefficient 0.15 corresponds to the 15% solid body rotation suggested by KIT.

The comparison is presented in **Figure 16**.

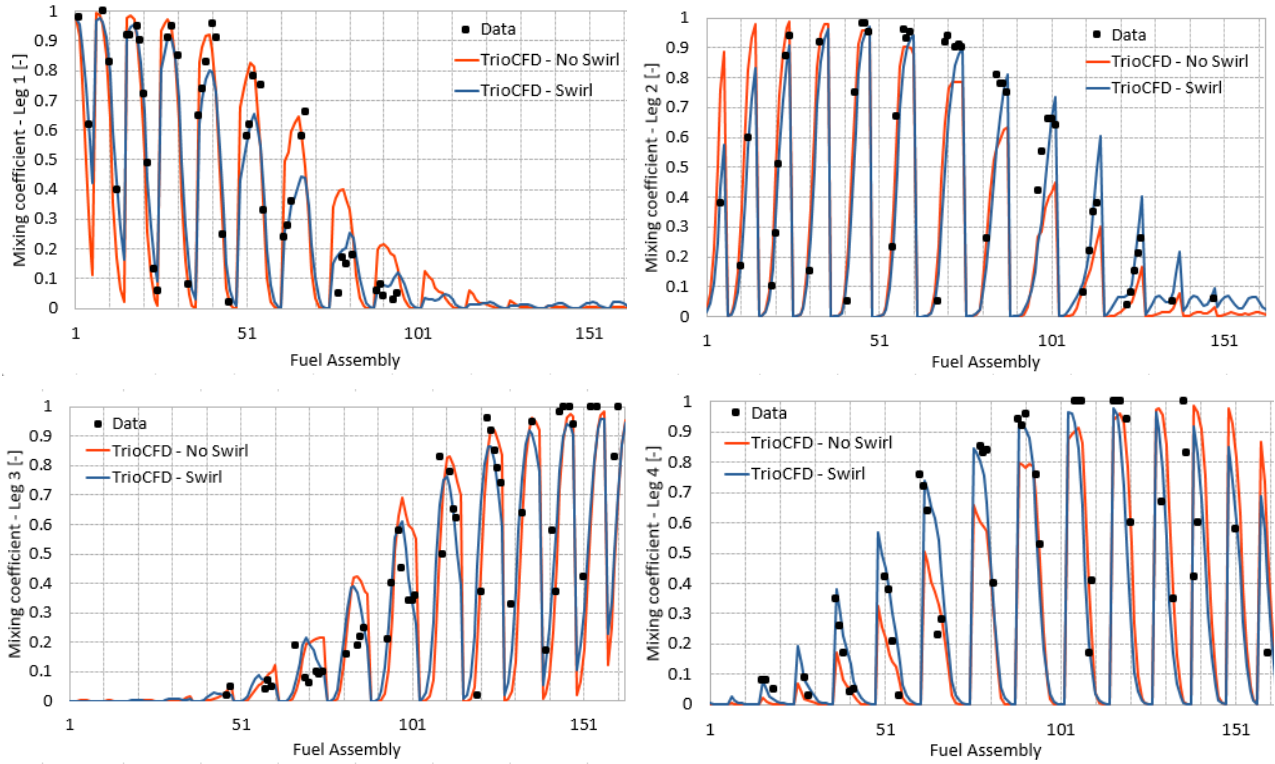


Figure 16: Mixing coefficient. Comparison between experimental data computed with /without swirl

The latter figure clearly shows an improvement in the mixing coefficient results, especially for the legs 2 and 4. More quantitatively, one can calculate the mean discrepancy between the simulation without and with swirl for each leg and presented in **Table 6**, which also shows a clear improvement of the results by implementing the swirl at the cold leg boundaries.

$$D_i = \frac{1}{N} \sum |E_i - E_{i,exp}|$$

Table 6: Quantitative comparison of the mixing coefficient without and with swirl

	Without Swirl	Swirl
Leg 1	0.138	0.060
Leg 2	0.127	0.086
Leg 3	0.143	0.111
Leg 4	0.190	0.168
Mean discrepancy	0.150	0.106

Consequently, we decided to realize the simulations with the swirl.

4.4.4 Strategy to compute the transient

It is not possible to arbitrarily set the time step beyond a certain limit with TrioCFD without the simulation to diverge. Consequently, it is not possible directly compute such a long transient. We estimate that the resources needed to realize a direct simulation of the transient is above 8 million CPU hours. Consequently, we needed to face the problem differently, especially as WP6.3 will require tens of simulations.

As the dynamic boundary conditions does not significantly vary during the transient: the mass flow rate evolves with a magnitude of about 3% for the cold leg 1 and almost none for the three other cold legs, we may assume that the velocity field does not significantly evolve during the transient. Subsequently, we propose to process as follows:

1. Simulation of steady-state velocity and temperature fields.
2. Extractions of the latter fields.
3. Simulation of the transient :
 - a. The temperature field is used as initial condition
 - b. The velocity field is fixed: The momentum equation is not solved and the temperature is solved with the fixed velocity field.

Thanks to this approach, the transient can then be simulated with reasonable resources: about 250,000 CPU hours to compute the steady state and approximatively 600 s of transient. For this deliverable, a crash in the simulation does not allow to run the transient until the expected end on time for the deadline. Fortunately, it nearly reaches the steady-state temperature and thus the results can still be exploited for the benchmark.

The temperature transient in the cold leg 1 is approximated with an analytic exponential expression, which is compared with the experimental data in **Table 6**. Discrepancy between experimental data and the analytical input for each point is less than 0.5 K. The other cold leg inlet temperatures are defined as constant.

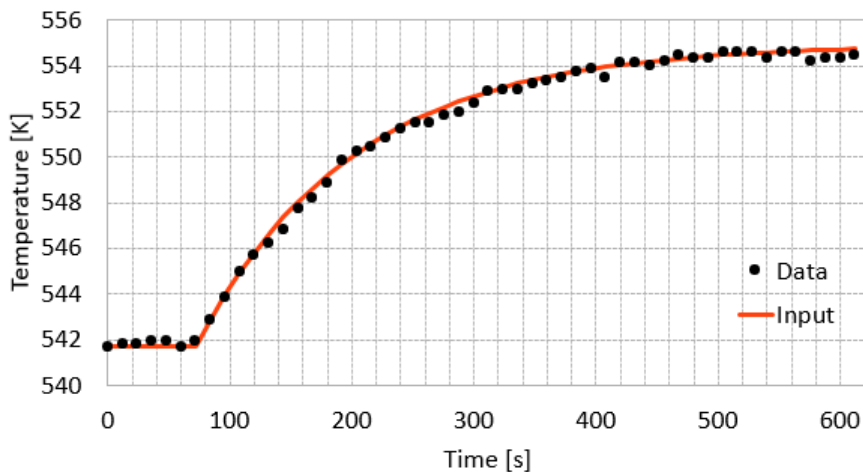


Figure 17: Analytic input for TrioCFD and comparison with experimental data

4.5 ENERGORISK Model (ANSYS/FLUENT 2019/R3)

For the simulation of the coolant mixing test performed at the Kozloduy Unit 6 NPP, an ANSYS/FLUENT model of the RPV and core was developed.

4.5.1 Geometry model: basic modelling simplifications

The geometric model in terms of the CFD problems is a representation of the volume and boundaries of the computational domain, which later serve as the basis for constructing the computational mesh of the discrete model.

Solid volumes of the reactor vessel and in-vessel equipment are not considered / adiabatic boundary conditions on surfaces (contact “fluid-solid”).

- The phenomenology of the studied processes (RPV mixing problem) is auto modal with respect to the possible influence of the heat energy of solid volumes – processes with sharp cooldown or heatup of the reactor as a whole, with the possibility of a heat transfer crisis, or processes in long-term (dozens of hours) cooldown/heatup of the reactor system are not considered. RPV mixing problem excluding solids practically does not lose physical essence and correctness and, at the same time, has much less loading on computational resources; this approach is widely used in international experience of the RPV mixing problem analysis with using of the CFD methods.

The core is modelled in a simplified manner using a porous media approach. For each fuel cassette provided individual cell zone with “porous zone” condition; fuel cassettes cross-flow is provided by internal interior interface

- Simplified modelling involves by technical plan document. Reactor core porous media approach is widely used in international experience

Supporting columns perforations (lower plenum), shielding tubes block perforations (upper plenum), reactor barrel perforations (upper plenum) and cross-flow between downcomer and upper plenum (around reactor spacer ring) are modelled in a simplified manner by porous jump approach at fluid-fluid interfaces.

- Simplified modelling involves by technical plan document. Porous jump model provides sufficient accuracy and correctness of the fluid flow distribution (takes into account the fluid flow area and hydraulic resistance of the space area, which is replaced by a flat porous jump interface) in case of impossibility/complexity of modelling a real geometrical profile

The buoyancy effects were neglected.

- High Reynolds number of flow and lack of conditions for the formation of the contour of natural circulation

4.5.2 Calculated mesh concept

The total RPV-model volume is divided into several parts, for which an exclusively structured mesh is formed based on hexahedral elements type;

- a structured qualitative mesh ensures stable convergence, correctness of the calculated results and acceptable problem/CPU time with the available underpowered computer resources;

These mesh parts are connected using fluid-fluid type of interfaces;

- the increase in CPU load due to the relatively large number of interfaces is offset by the efficiency of the structured mesh;

Core mesh model involves the allocation of 163 volumes of individual cassettes connected by an interior interface and forming 163 cell zones; all other mesh volumes are formed one fluid cell zone

- mesh convergence studies are considered (coarse, medium and fine meshes) and represent the initial stage of model validation; the medium mesh (17.28E06 nodes) is chosen as the most optimal.

In the **Figure 18** to **Figure 22**, the meshing of the different regions of the RPV are shown as developed for the FLUENT simulations.

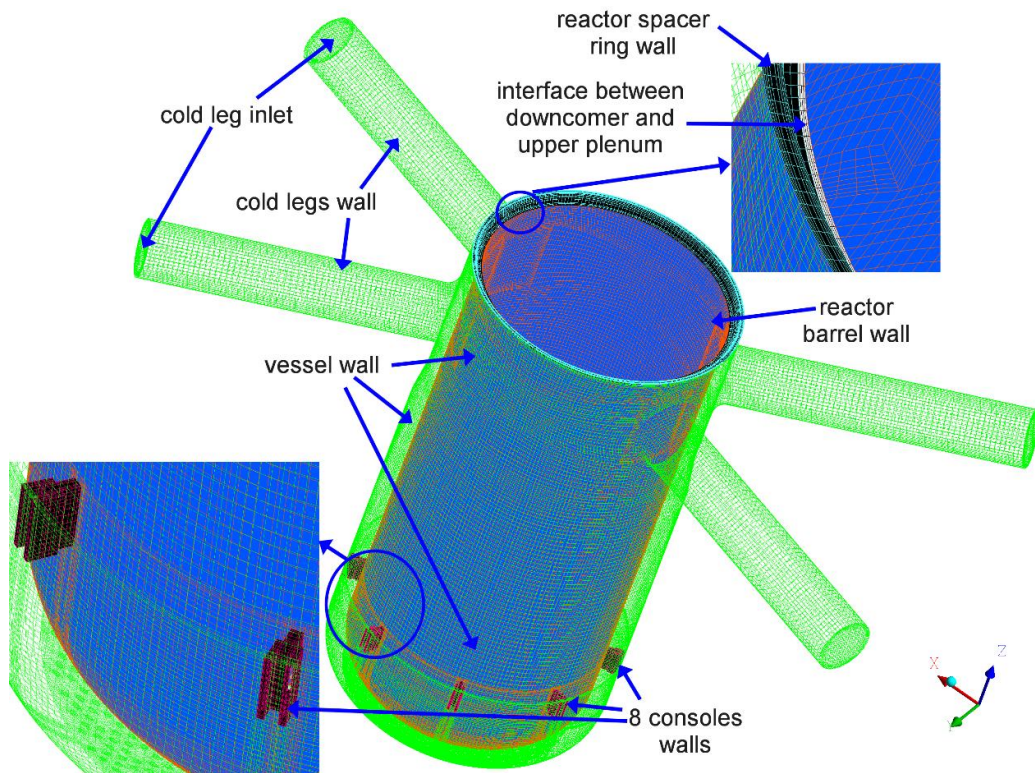


Figure 18: Cold legs, downcomer (only vertical part) / 8.594E05 nodes / 7.946E05 elements

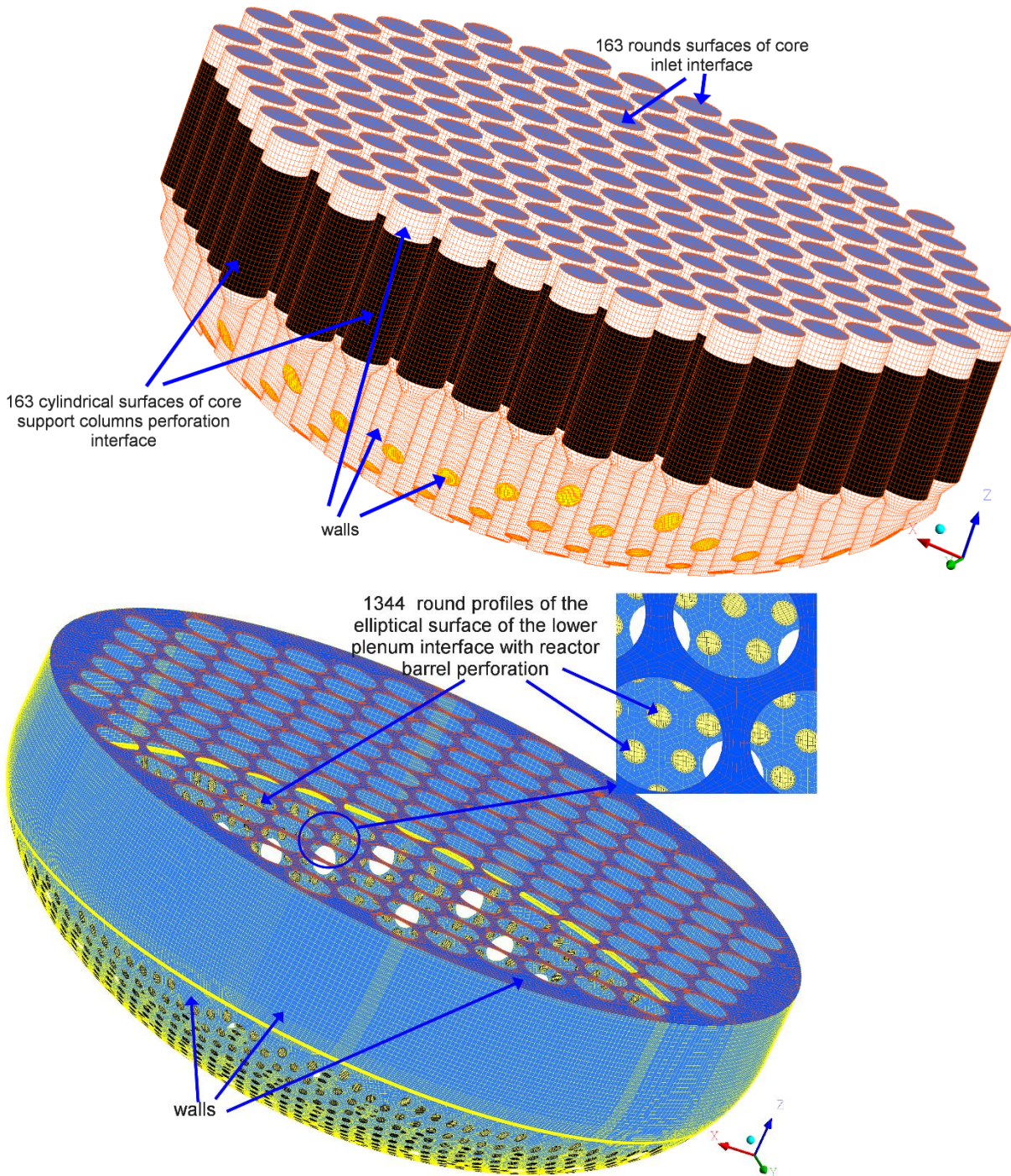


Figure 19: Lower plenum (including space of reactor vessel elliptical bottom) / 9.647E06 nodes / 8.748E06 elements

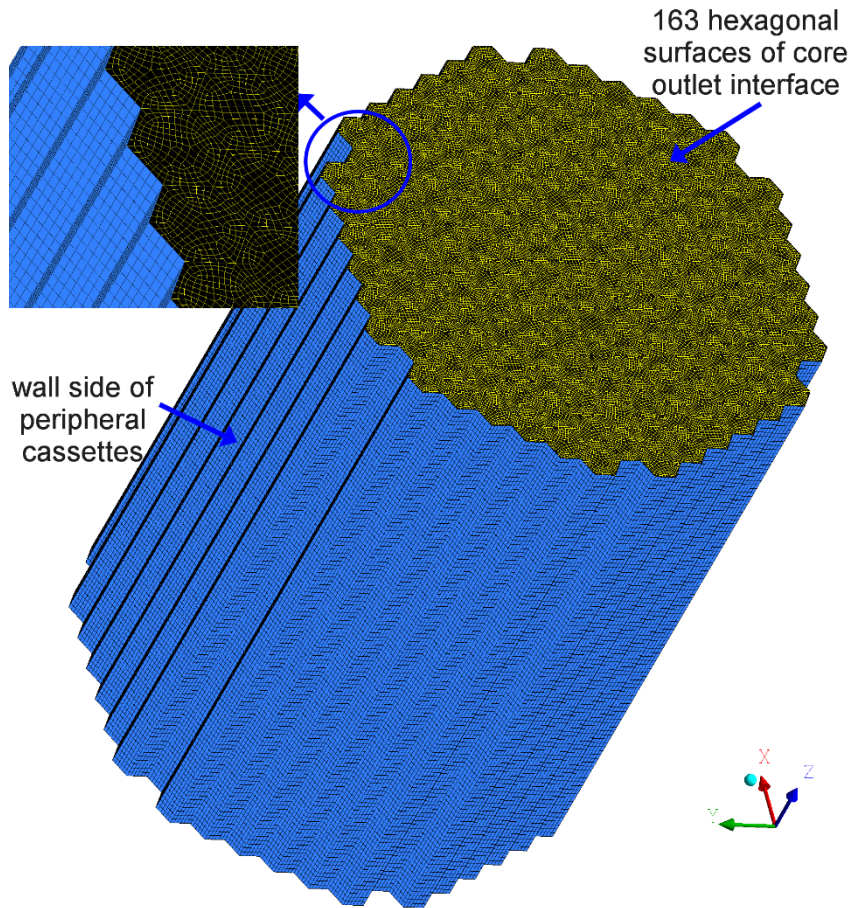


Figure 20: Reactor core / 3.448E06 nodes / 3.076E06 elements

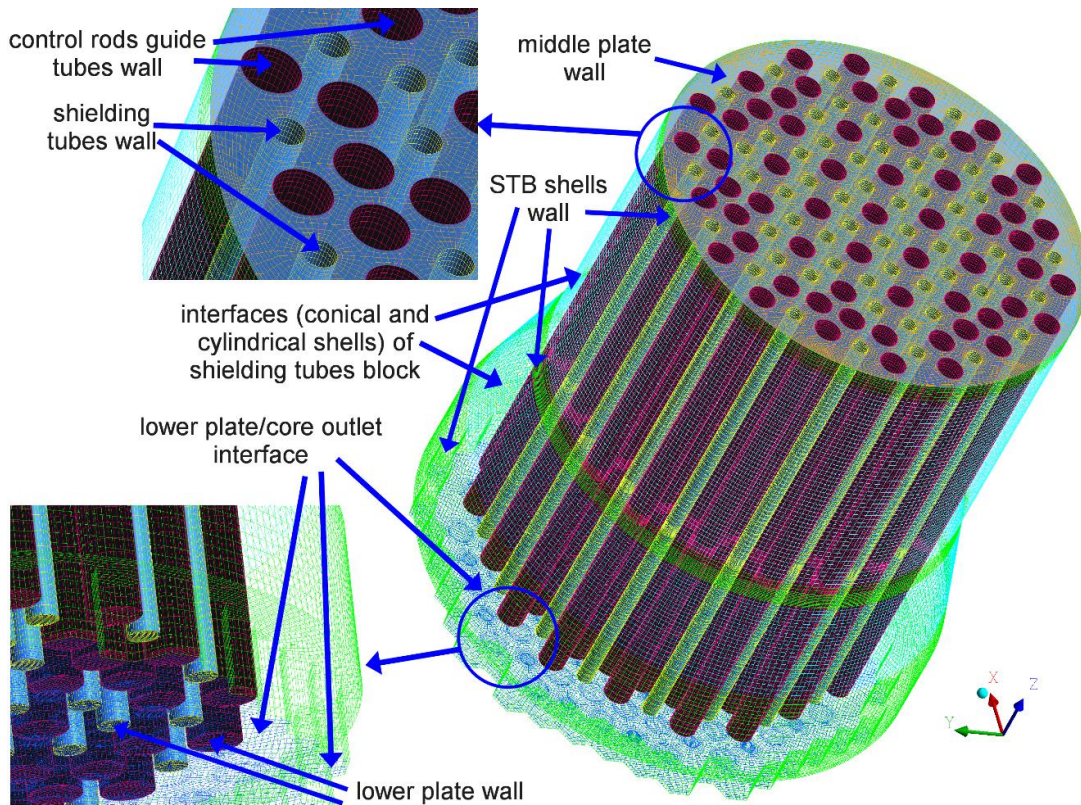
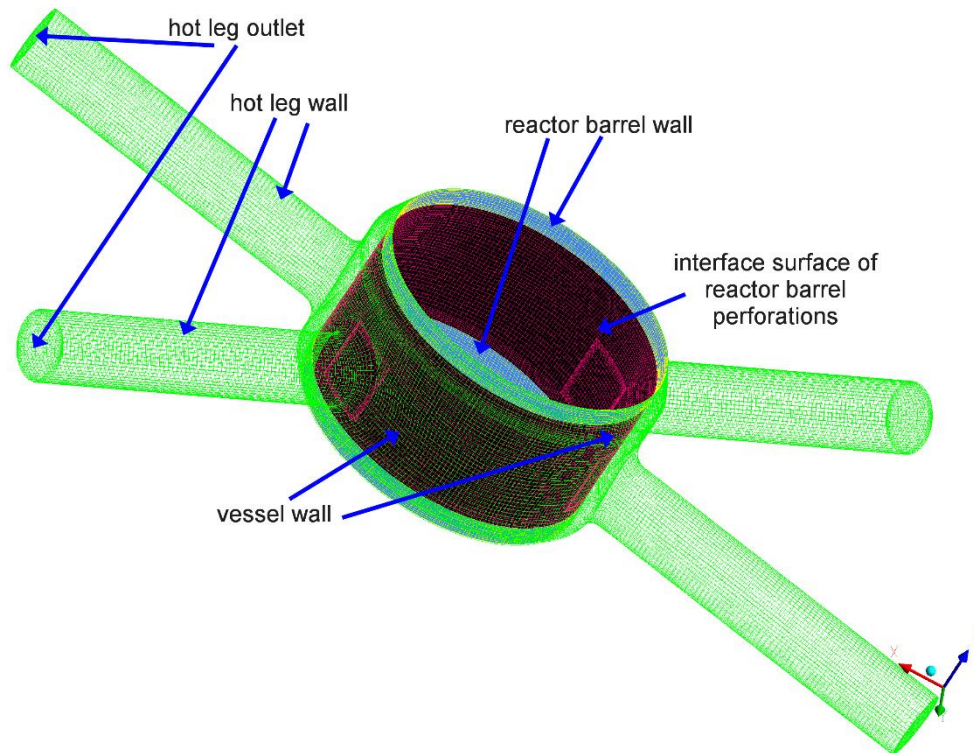


Figure 21: Upper plenum / 2.915E06 nodes / 2.575E06 elements**Figure 22: Hot legs and hot legs collection chamber / 4.154E05 nodes / 3.868E05 elements**

4.5.3 Turbulence modelling

The following models were selected: RANS approach, the SST $k-\omega$ turbulence model, and the scalable wall treatment.

This turbulence model brings together opportunities $k-\omega$ turbulence models family (correctness of numerical analysis at low Reynolds numbers) and $k-\epsilon$ turbulence models family (correctness of numerical analysis at high Reynolds numbers, taking into account the vorticity and mixing of flows).

4.5.4 Boundary conditions

The following boundary conditions were setup:

- inlet: the fully formed velocity profile is considered which provides the necessary mass flow; T =cold legs temperature;
- outlet: the pressure at the outlet from the reactor and the backflow temperature equal to the average temperature at hot legs outlet are considered;
- walls: adiabatic thermal conditions; smooth walls.

Remarks:

- for all considered computational analyses, a similar topology of mass and thermal boundary conditions is assumed;
- details of the boundary conditions are selected based on modelling experience and recommendations for the CFD-code under consideration.

4.5.5 Core model

Porous media approach involves modelling of viscous and inertial losses; the main axial direction and the direction of transverse losses (loss multiplier=10÷50) are considered;

- the choice of parameters of the cassettes porous medium is made iteratively with subsequent adjustment to the required or design parameters of the reactor;

Heat energy sources are modelled individually for all cassettes; cassette energy source is formed in the form of an axial profile based on axial non-uniformity of energy release and uneven energy release coefficients

- the cassettes heat energy source profiles are adjusted using multiplier factors to provide the required total core power.

4.5.6 RPV model adjustment

The adjustment of the pressure drop in the sections of the reactor and leakage from downcomer to upper plenum is implemented by simulating additional inertial losses at some interfaces with porous-jump model. In the following **Table 7** an overview of the predicted pressure drops compared to the design values is given.

Table 7: Comparison of the pressure drop in different sections of the RPV regarding the reference value

Reactor element / section	Design value	Calculated value	Absolute relative deviation (%)
Pressure difference (MPa)			
Reactor inlet chamber (section 1-2)	0.201	0.1990	0.995
Reactor core (section 2-3)	0.142±0.025	0.1424	0.282
Reactor outlet chamber (section 3-4)	0.037	0.0369	0.270
Reactor without inlet and outlet nozzles	0.380±0.06	0.3783	0.447
Crossflow between downcomer and upper plenum (percent of the total reactor mass flow rate)			
Gap between reactor spacer ring and reactor barrel (point-5)	0.10	0.0975	2.50

In **Figure 23**, the location of the positions for the pressure difference prediction and the flow paths are given.

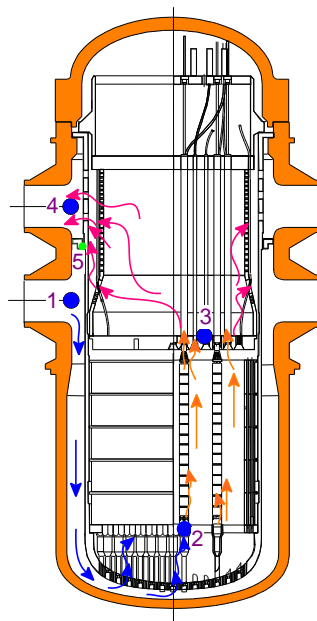


Figure 23: RPV with the main flow paths and the locations for the pressure difference prediction

4.5.7 Simulation of the CFD Benchmark on Kozloduy-6 Coolant Mixing Experiment

Implementation of Task 6.2 regarding CFD-simulation of mixing experiment benchmark on Kozloduy-6 is divided into three logical stages:

- 1st stage: quasi-stationary simulation of NPP experiment initial state;
- 2nd stage: transient simulation of benchmark scenario;
- 3rd stage: quasi-stationary simulation of NPP experiment final state

4.5.7.a Initial state of the plant

The first stage of the CFD simulation of mixing experiment benchmark on Kozloduy-6 is the numerical evaluation of the initial state (problem time is equal to 0.0 s). The initial state is a quasi-stationary process with constant boundary conditions, which represents the conditions of the reactor plant before conducting an experiment to study the mixing conditions of the coolant in the reactor vessel at asymmetric flow from the loops of the main circulation circuit. The conditions of the reactor plant, which represent the initial state, are as follows:

- Reactor parameters:
 - the reactor is at low power;
 - thermal power of the reactor is 281 MW (9.36% of nominal power);
 - the reactor is at the beginning of the cycle;
 - control rod groups #9 and 10 are fully inserted and groups #1÷7 are fully withdrawn; the position of the regulating rod group #8 is about 84% from the core bottom;
 - the automatic power controller and power limitation controller are turned off
- Coolant parameters:
 - coolant temperature at the reactor inlet is about 541.8 K (about 20 K lower than the nominal value);
 - pressure above the core is about 15.59 MPa (close to the nominal value of 15.7 MPa);
 - steam generator levels are equal to the nominal ones and there is no let-down flow; the main steam header pressure is 5.07 MPa (about 1.0 MPa lower than the nominal value).

The main objectives of the 1st stage of the mixing experiment simulation are as follows:

- Determination of mixing coefficients from cold legs to fuel cassettes outlet; comparison of the results (mixing coefficients) of the CFD calculation assessment and the KNPP-6 test;
- Definition of cassettes outlet average temperature; comparison of these results for CFD calculation and NPP experiment;
- Determination of hot legs outlet average temperature; comparison of this results for CFD calculation and NPP experiment;
- Definition of cassettes outlet mass flow rate;
- Definition of cassettes inlet average temperature and mass flow rate;
- Formation of complete spatial initial conditions for the implementation of the transient simulation in the next 2-nd stage.

4.5.7.b Initial conditions

The algorithm for forming the initial conditions for quasi-stationary calculation at the initial state of mixing experiment simulation is based on the principle of optimal use of numerical resources and is as follows:

- Steady-state solver run with hybrid Fluent solver initialization; hybrid initialization is recommended for large-scale tasks, especially in the case of porous medium modelling (SST k- ω turbulence model);
- Transient solver run from the case data of the previous steady-state calculation (DES turbulence model, modified k- ω model).

The settings of the steady state and transient solvers are identical for the calculation analyses in the previous stages for NPP nominal operating mode.

4.5.7.c Boundary conditions

A separate feature of the first stage of the CFD simulation of the mixing experiment in comparison with the following is the estimation of the so-called mixing coefficients. The loop to fuel assembly mixing coefficient K_{ij} is defined as the ratio of coolant flow from loop i (CLs, $i=1\div 4$) to the total flow through the assembly j ($j=1\div 163$) and takes values from 0.0 to 1.0 (0÷100%). The mixing coefficients in the ANSYS Fluent are modelled using solve the transport equation for an arbitrary, user-defined scalar (UDS) in the same way that it solves the transport equation for a scalar such as species mass fraction. These additional transport equations, which are initiated by the introduced passive scalars, track the transport (spreading and distribution) of the coolant from the user-specified location (cold legs inlet plane) to the study area (fuel cassettes outlet).

The sequence of simulation of the mixing coefficients is as follows:

- is introduced into the system of the 4th user-defined scalars UDS_{*i*} which correspond to the amount and item of CLs of circulation loops ($i=1\div 4$, correspond to CLs item); its UDS have the following parameters: active inlet diffusion function, flux function is mass flow rate;
- the coolant properties are complemented by the so-called UDS diffusivity (the dimension corresponds to the kinematic viscosity); based on default value of turbulent Schmidt number $Sc=0.9$ for $k-\omega$ turbulence models ($Sc=0.7$ for $k-\epsilon$ models) and functions of coolant dynamic viscosity $\mu(T)$ as well as coolant density $\rho(T)$ versus temperature T UDS diffusivity D defined as user-defined expression $D(T)=\mu(T)/(Sc \times \rho(T))$;
- inlet boundary conditions are complemented UDS area; UDS option is defined as specified value (portion of flow); i -th item of UDS_{*i*} takes the value 1.0, else 0.0 (for example, UDS₁ for loop-1 takes the value 1.0 when UDS_{2,3,4} for this loop takes the value 0.0).

The details of the list of boundary conditions used to perform quasi-stationary calculation representing initial state of V1000CT-2 mixing experiment on Kozloduy-6 are given in [18].

4.5.7.d Core heat energy release

For initial state (beginning of the mixing experiment) reactor total (thermal) power is 281 MW (9.36% of the nominal value); the reactor is at the beginning of cycle (BOC), [2].

Modelling the core heat energy release (energy source) is based on the following approach:

- individual profiles of energy release for each fuel cassette are considered (163 Fluent cell zones):
 - power profiles are set as user-defined functions based on imported external «Excel.csv» files;
 - the dependence of the energy release (specific heat power, W/m³) on the axial coordinate (Z -coordinate, m) of the fuel cassette model within the boundaries of the heated part is considered; the lower coordinate of core heated part is equal to 1.83 m and the upper coordinate – 5.38 m;
- the complete energy release profile is formed by multiplying two components:
 - first component: distribution of the energy release averaged over all the cassettes along the height of the core heated part; is based on the value of the reactor thermal power and the distribution of the coefficient of non-uniformity of energy release along the height of the core;
 - second component: uneven energy release coefficients by fuel cassettes; simulates part of the reactor thermal energy released in each cassette separately (takes into account the radial non-uniformity of energy release).

Figure 24 shown distribution of average energy release by core heated part height. This distribution is formed based on the following data:

- average cassette heat power N_{CAS} :
 - $N_{CAS}=N_{TOT}/163=1.724$ MW ($N_{TOT}=281$ MW – reactor total heat power);
- volume of the heated part of the fuel cassette mesh model: $V_{CAS}=0.17123$ m³;
- uneven energy release coefficients by core height:
 - the axial non-uniformity of the energy release is applied for Kozloduy-6 NPP at initial state before mixing experiment (beginning of fuel cycle) according to the partner's data;
 - the selected coefficients KZ of axial non-uniformity of energy release are given below (H – relative core heated part height, %):

K _Z	0.607	1.146	1.399	1.410		1.306	1.194	1.068	0.898	0.654	0.318
H	5	15	25	35		45	55	65	75	85	95

Figure 24 shows the distribution of selected «points» of the resulting axial non-uniformity of energy release («Source vs. Z») and the integral curve («Fitted curve») used for the subsequent BC formation. The integral curve was obtained on the basis of the data «points» of the theoretical distribution using the MATLAB Curve Fitting Tool instrumentation. This curve has the following functional relationship («sum-of-sine» curve fitting type):

$$Q_{V,CAS} = a_1 \times \sin(b_1 \times Z + c_1) + a_2 \times \sin(b_2 \times Z + c_2) + a_3 \times \sin(b_3 \times Z + c_3), \text{ W/m}^3,$$

where Z – axial core heated part coordinate, m;

$a_1, b_1, c_1 = 1.728E07, 0.9723, -1.872$ – the coefficients of the first term of the sine function;

$a_2, b_2, c_2 = 4.853E06, 1.83, -2.231$ – the coefficients of the second term of the sine function;

$a_3, b_3, c_3 = 2.347E05, 3.887, -1.912$ – the coefficients of the third term of the sine function.

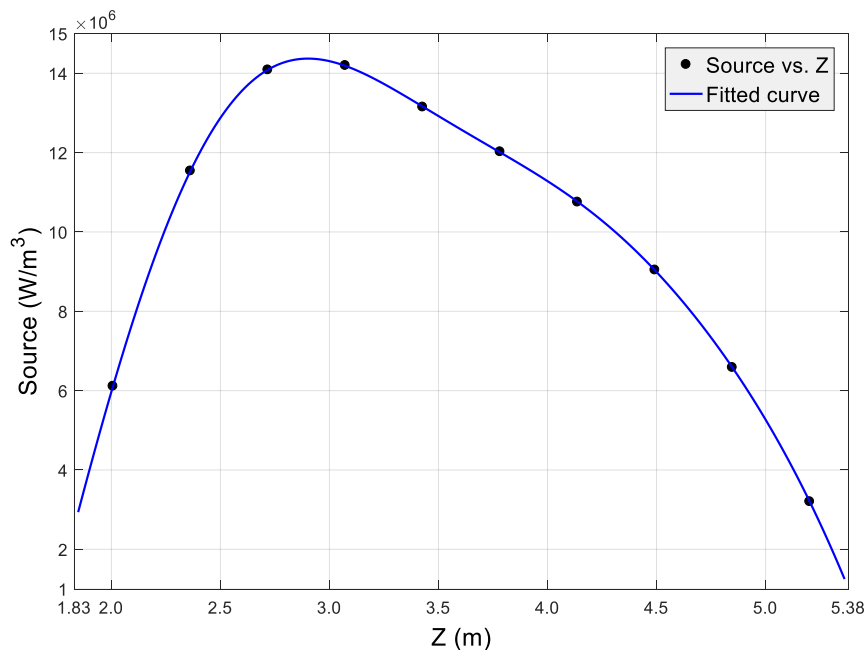


Figure 24: Distribution of average energy release by core height

Figure 25 shows the distribution of uneven energy release coefficients (K_q) by fuel cassettes. These coefficients are based on the following principles and data:

- the coefficients of non-uniformity of energy release by cassettes are applied for Kozloduy-6 NPP at initial state before the mixing experiment (beginning of fuel cycle) according to the partner's data.

Checking and adjusting the energy source BC for the fuel cassettes model takes into account the following:

- the model response to the discrete energy release profile is checked after its interpolation to the computational mesh;
- a preliminary calculation is performed to estimate the total power allocated in the cassettes;
- using a multiplying factor, the original energy release profiles are corrected for accurate correlation with the required value of the total heat power.

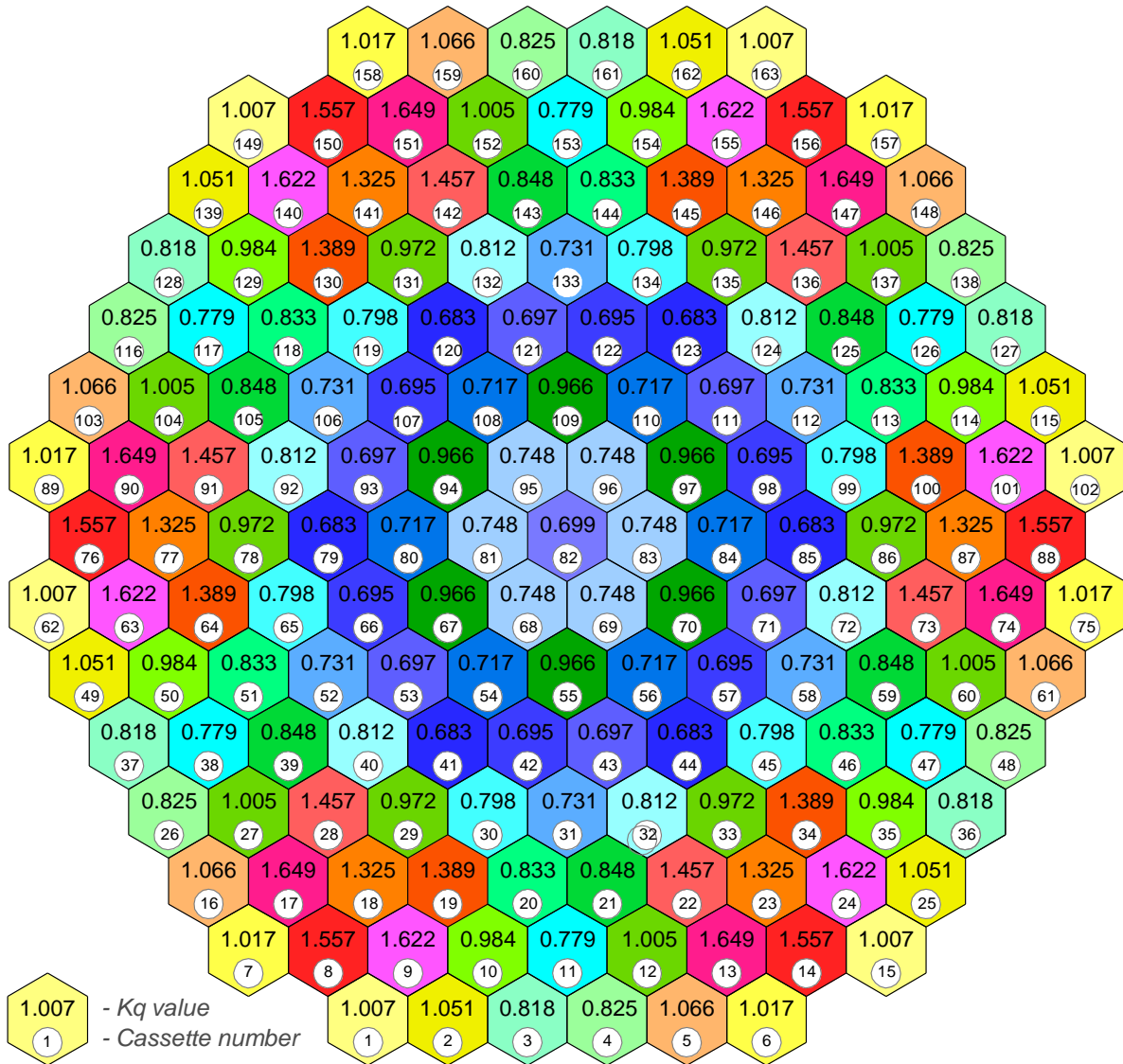


Figure 25: Distribution uneven energy release coefficients by cassettes

4.5.7.e Calculation results and conclusions

Table 8 shows the main balance results of quasi-stationary calculation representing RPV operating conditions at reduced power (9.4% of nominal power level) – initial state of Kozloduy-6 V1000CT-2 mixing experiment: outlet mass flow rate and average temperature (mass and heat energy balance parameters). Also provides an estimate of the relative deviation Δ of the calculated values:

- HL outlet, loop-1÷4 (item 1÷4 in Table 8) – relative deviation between average value of mass flow rate by loops and mass flow rate for loop-1÷4; relative deviation between calculated and experimental results for HLs outlet average temperature;
- RPV model total outlet (item 5 in Table 8) – relative deviation between total inlet (BC) and outlet mass flow rate; relative deviation between total outlet average temperature (calculated value) and its theoretical formulation (by fundamental relationship); total outlet average temperature by fundamental relationship is estimated in the following way:
- $T_{ave} = T_{in} + N_{tot} / ((MFR_{in} - MFR_{leak}) \times C_{p,ave}) = 544.718$ K,
- where $T_{in} = (T_{in-cl1} \times MFR_{cl1} + T_{in-cl2} \times MFR_{cl2} + T_{in-cl3} \times MFR_{cl3} + T_{in-cl4} \times MFR_{cl4}) / MFR_{in} = 541.775$ K – average inlet temperature (boundary condition);
- $MFR_{cl1-4} = 4737, 4718, 4682, 4834$ kg/s – CL-1÷4 inlet mass flow rate respectively (boundary condition);
- $T_{in-cl1-4} = 541.72, 541.65, 541.88, 541.85$ K – CL-1÷4 inlet temperature respectively (boundary condition);

- $MFR_{in}=MFR_{cl1}+MFR_{cl2}+MFR_{cl3}+MFR_{cl4}=18971$ kg/s – inlet total mass flow rate (boundary condition);
- $MFR_{leak}=12.9$ kg/s – crossflow between DC and UPL (calculated result);
- $N_{tot}=281$ MW – core total heat energy release (boundary condition);
- $C_{p,ave}=5036.46$ J/kg/K – average coolant heat capacity (boundary condition).

Table 8: Main balance results of quasi-stationary calculation representing initial state of Kozloduy-6 mixing experiment (V1000CT-2)

Item	Outlet BC section	Mass flow rate		Average temperature		
		Value (kg/s)	Δ (%)	CFD-value (K)	Test-value (K)	Δ (%)
1	HL of loop-1	4754.13	0.24	544.635	545.00 \pm 2.0	0.067
2	HL of loop-2	4804.14	1.29	544.670	544.78 \pm 2.0	0.020
3	HL of loop-3	4871.43	2.71	544.737	545.03 \pm 2.0	0.054
4	HL of loop-4	4541.85	-4.24	544.790	545.00 \pm 2.0	0.039
5	Total outlet section	18971.55	0.003	544.707	–	-0.004

4.5.7.f Main Conclusions:

Based on the balance results of the quasi-stationary calculation, given in **Table 8**, the following conclusions can be formulated regarding the correctness of results of the mixing experiment initial state simulation:

- negligible deviation (0.003%) in mass balance – total inlet and outlet mass flow compliance;
- negligible heat balance deviation (0.004%) – correspondence between the heating of the coolant at RPV model and the generated heat power in the core;
- the deviation of the outlet mass flow rate through loop in comparison with the average flow rate for the loops is not a representative parameter (not regulated by design standards) for the reactor operating mode with reduced power level with the existing asymmetry of the flow at the inlet; nevertheless, estimated the value of the maximum relative deviation of this quantity, which is 4.24% and has no significant deviation (proportionality) from this value for cold legs (1.92%), which indicates the correctness of the calculated results;
- negligible relative deviation between calculated (CFD simulation) and experimental results regarding to HLs outlet average temperature taking into account the error of temperature measurement experimentally, which is ± 2.0 K; the values of this deviation are as follows:

	HL-1	HL-2	HL-3	HL-4
Experiment, K	545.00	544.78	545.03	545.00
CFD, K	544.635	544.670	544.737	544.790
Deviation, %	0.067	0.020	0.054	0.039

Detailed results of the calculation of the mixing coefficients from the loops (cold legs inlet) to the fuel cassettes outlet are given in (mass flow averaged values). Regarding the main result of the calculation analysis at 1st stage of V1000CT-2 experiment simulation (initial state), namely the mixing coefficients, the following conclusions can be formed:

- sufficient and reliable correlation of calculated and experimental results is available; such a correlation is observed for the mixing coefficients from all loops;
- sufficient correlation of calculated and experimental estimated values of azimuthal shift of the loop flow centres (azimuthal asymmetry of loop flow centres relative to the cold leg axes); loop flow centres represent the centrelines of non-mixing zones with mixing coefficients about $0.9\div 1.0$ (90 \div 100%); the following results were obtained for azimuthal shift of the loop flow centres:

	Loop-1	Loop-2	Loop-3	Loop-4
Experiment	-24°	+8°	-30°	+8°
CFD	-33.7°	+8.3°	-32.3°	+8.1°

- it should also be noted that the experimental results, especially at the boundary section of the loop sectors (active mixing zone), have some degree of inaccuracy due to the difficulty of determining the mixing coefficients experimentally; the experimental way of mixing coefficients determining has the following limitations:
 - indirect principle of determining mixing coefficients based on heat balance; thus does not take into account the discrepancy of coolant flow at the inlet and outlet of the cassettes, which is noticeable;
 - limited number of temperature sensors at the outlet of the cassettes;
 - the estimation of the mass flow rate of the coolant through the cassette additionally depends on the error of measuring the temperature at the outlet of the cassettes, and the analytical estimation of the flow distribution from the loops to cassettes depends on the dimension of the considered range of possible combinations which ensure compliance with the heat balance.

Other key results of the 1st stage of V1000CT-2 experiment simulation (initial state) is the distribution of coolant flow parameters at the inlet and outlet of the cassettes. Detailed results of the calculation of the mass flow rate and average temperature (mass flow averaged values) at fuel cassettes inlet/outlet. Regarding of this results of the calculation analysis at 1st stage of V1000CT-2 experiment simulation the following conclusions can be formed:

- excellent correlation of calculated and experimental values of the average temperature at the fuel cassettes outlet:
 - the calculated results (CFD simulation) correlate with the experimental values taking into account the error of temperature measurement $dT=\pm 1.0$ K (for reactor outlet temperature measurement by in-reactor control system);
 - not essential value of relative deviation between calculated and experimental results regarding to cassettes outlet average temperature: maximum deviation is 0.196%, average deviation is 0.071%;
- the coolant temperature distribution at the fuel cassette inlet corresponds to the asymmetry of the inlet BC (noticeable formation of azimuthal sectors and mixing zones) and correlates with the resulting distribution of mixing coefficients;
- there is a slight fluctuation of the distribution of the coolant flow in the sectors at the fuel assemblies' inlet in comparison with the nominal NPP operating mode, which corresponds to the asymmetry of the coolant flow from the cold legs; coolant mass flow rate at the cassettes outlet is characterized by much lower fluctuations due to the coolant crossflow at the height of the fuel assemblies.

Sections of the spatial distribution of physical parameters confirm the following aspects of the computational study of quasi-stationary regime of Kozloduy-6 NPP at reduced reactor power level (9.36% of nominal power) and some asymmetry of the inlet coolant flow before mixing experiment researching:

- correct pressure distribution based on estimates of the pressure loss in the reactor sections;
- correct distribution of coolant velocity based on pressure distribution, core modelling assuming porous medium and reactor design features;
- the correct amount of the coolant heating in the core and the nature of the temperature distribution based on the NPP operating non-uniformity of energy release; the average core outlet temperature at heated part 544.718 K is slightly larger than the average RPV model outlet temperature 544.707 K (see **Table 8**) due to additional coolant mixing up the cassettes over the heating core part.

5 Overview of model and parameter settings

In the following **Table 9**, an overview of the models and parameters used by the different partners in the different CFD-simulations is given.

Table 9: Overview of model and parameters used by the different CFD-codes

	CEA	Energorisk	Framatome	KIT	UNIFI
Tool	TrioCFD	ANSYS Fluent	STARCCM+	ANSYS CFX	STARCCM+
Mesh type	unstructured	mainly structured	unstructured	unstructured	unstructured
Mesh elements	Tetra	mainly hexahedra	tetra+polyhedra	mainly tetrahedra and prisms	tetra+polyhedra
Boundary layer inflation	no	linear narrowing of mesh layers (block topologies)	yes	yes (not everywhere)	yes
No of elements	32 mio	15.4 mio	48 mio	36 mio	27.6 mio
Element size			8 mm - 80 mm	5 mm – 50 mm	20 mm – 100 mm
CAD model	Framatome	Framatome	Framatome	Framatome	Framatome
Upper plenum	Full resolved	CAD extensions (shielding and control rods tubes are considered)	Porous media CAD extensions	Porous media	Porous media CAD extensions
Turbulence model	Standard k- ϵ	SST k- ω	k- ϵ low Re	SST	Standard k- ϵ
Physical properties	T dependent at 15.6 MPa	T dependent at 15.6 MPa	T dependent At 15.6 MPa	IAPWS tables with p and T dependency	T dependent at 15.6 MPa
Spatial discretization	VEF (finite volume elements)	2 nd order	2 nd order	Higher order method Blending 1 st -2 nd ord.	2 nd order
Time integration				2 nd order Euler back- ward	
Cold to hot leg bypass	Not modelled			Not modelled Mass flow at the inlets reduced by 1%	Not modelled and total mass flow at the inlets reduced by 1%
Core basket bypass	Not modelled			Modelled; mass flow rate ~3%	Modelled and flow restricted in the core basket to be ~3%

SWIRL	Consideration of additional pump swirl at the cold leg inlets			Consideration of additional pump swirl at the cold leg inlets	
-------	---	--	--	---	--

6 Comparative results

Hereafter, selected parameters describing the main thermal hydraulic plant models at the nominal conditions just before the coolant mixing test are given in the following **Table 10**.

Table 10: Comparison of the pressured drop predicted by the different partners with the reference data

ΔP	ΔP data [MPa]	Framatome	KIT	UNIPI	CEA	ENERG
P0-P2	0.201	0.233	0.199	0.2186		0.1990
P2-P4	0.142	0.154	0.155	0.1438		0.1424
P4-P5	0.029	0.034	0.018	0.0315		0.0306
P4-P6	0.037	0.058	0.031	0.0387		0.0369
P0-P6	0.380	0.446	0.376	0.4076		0.3783
ΔP data are design pressure drops at full power						

6.1.1 Reference values compared with predicted ones at 0 s

In **Table 11**, a comparison of the pressure drop predicted by the partners and the reference data is given.

Table 11: Comparison of the pressured drop predicted by the different partners with the reference data

Parameter	Data	CEA	ENERG	Framatome	KIT	UNIPI
Core power [MW]	281	283	281	281	281	281
Cold leg 1, T [K]	541.7 2	541.75	541.72		541.72	541.72
Cold leg 2, T[K]	541.6 5	541.85	541.65		541.65	541.65
Cold leg 3, T [K]	541.8 8	541.75	541.88		541.88	541.88
Cold leg 4, T [K]	541.8 5	541.75	541.85		541.85	541.85
Hot leg 1, T [K]	545.0	544.36	544.64	544.79	544.64	544.81
Hot leg 2, T [K]	545.0	544.5	544.67	544.86	544.74	544.89
Hot leg 3, T [K]	544.9	544.65	544.74	544.91	544.75	544.92
Hot leg 4, T [K]	545.0	544.77	544.79	545.01	544.91	545.04
Cold leg 1 flow rate [kg/s]	4737	4721	4737	4737	4737	4690
Cold leg 2 flow rate [kg/s]	4718	4612	4718	4718	4718	4671
Cold leg 3 flow rate [kg/s]	4682	4667	4682	4682	4682	4635
Cold leg 4 flow rate [kg/s]	4834	4894	4834	4834	4834	4785
Core flow rate (inc. bypass) [kg/s]	18971	18893	18972		18955	18782*

* UNIPI model does not consider the cold-leg to hot-leg bypass, and the total mass flow at the inlets is reduced by 1%. Deviation from the plant data, shall be explained, stressing what types of bypasses is modeled or not. Bypasses modelling whether considered or not may be mentioned in Table 7. (i.e., cold leg to hot leg bypass; core basket bypass)

6.1.2 Data-vs-prediction: Loop temperature at RPV-outlet during the transient

Transient calculations are split into two steps. First, a steady-state calculation at Hot Full Power (HFP) that will serve as the initial condition. Secondly, the transient scenario with its corresponding boundary conditions and time evolution is performed. In the **Figure 26** to **Figure 29**, the comparison of the data with the coolant temperature of the hot legs 1 to 4 predicted by the different partners is shown.

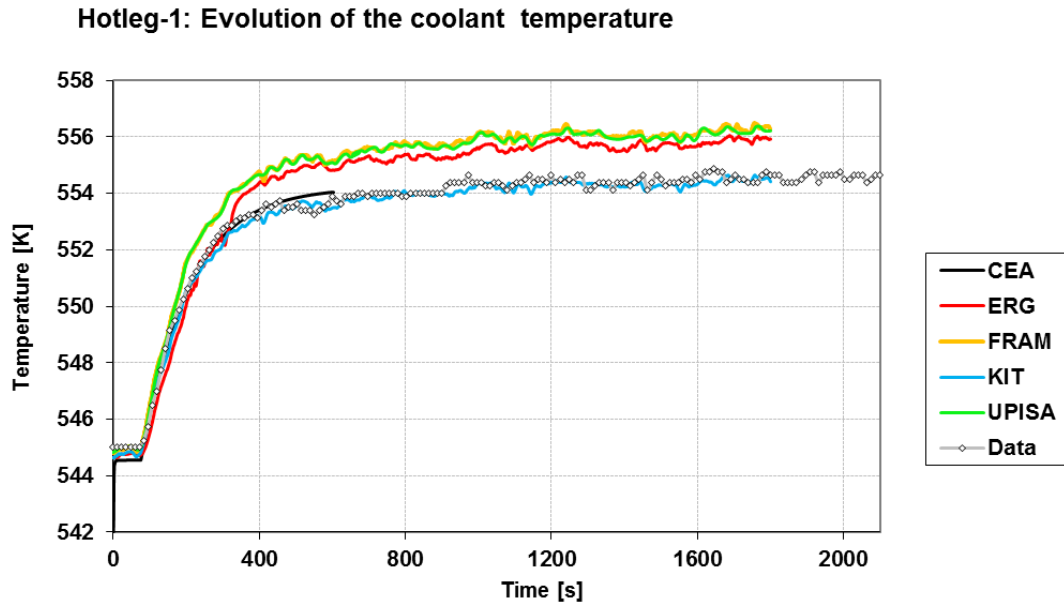


Figure 26: Comparison of the hot leg 1 temperature predicted by the partners with the data

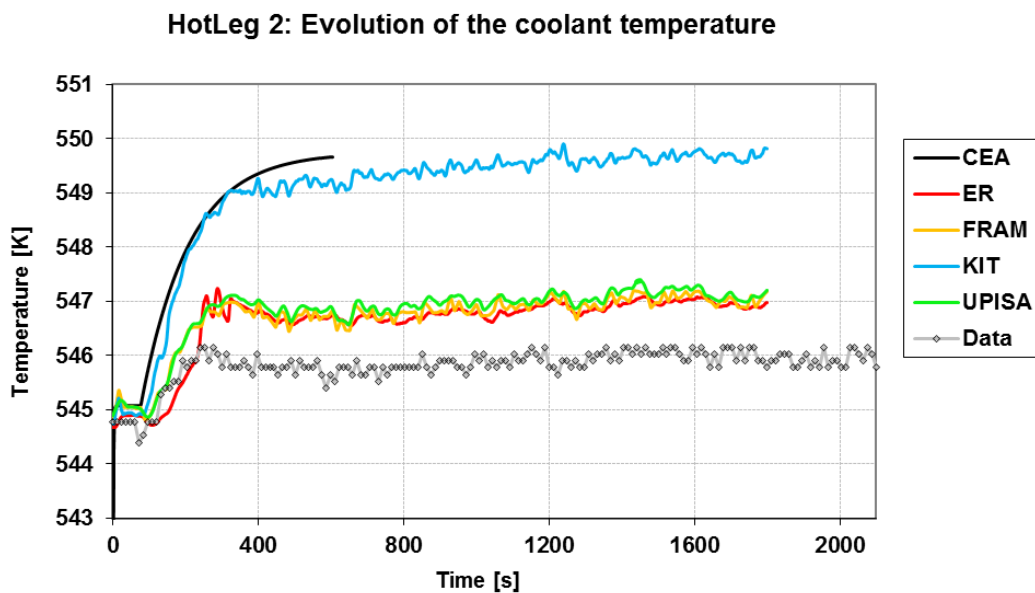


Figure 27: Comparison of the hot leg 2 temperature predicted by the partners with the data

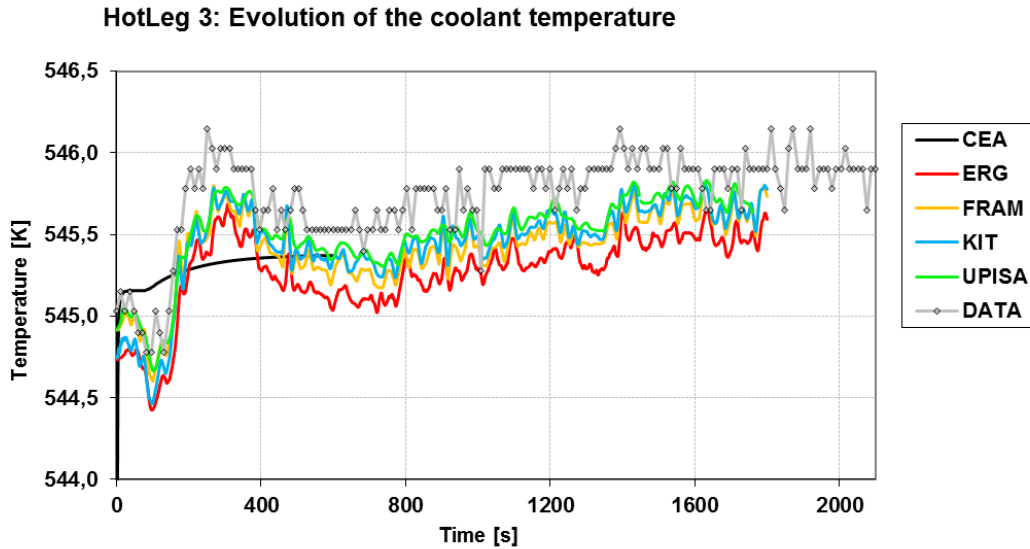


Figure 28: Comparison of the hot leg 3 temperature predicted by the partners with the data

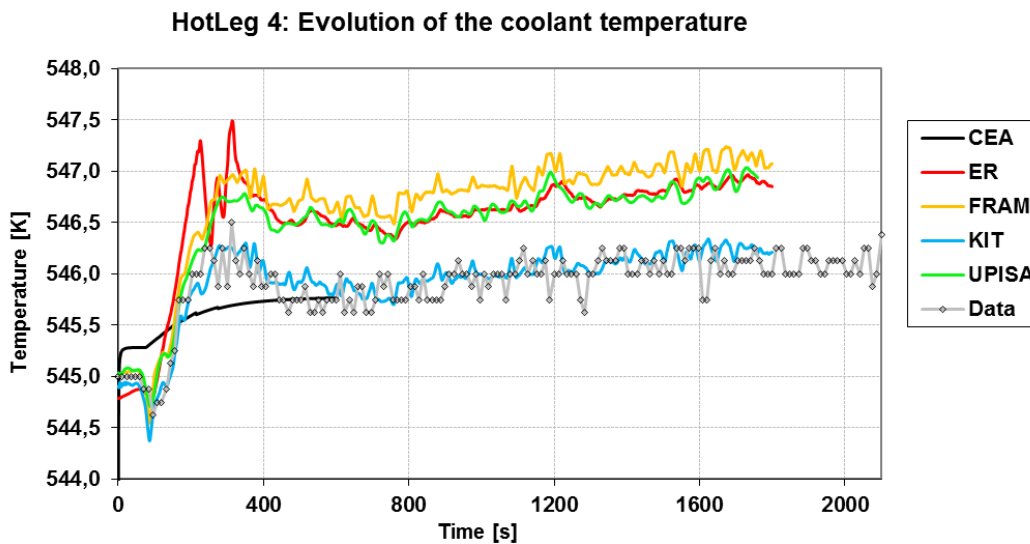


Figure 29: Comparison of the hot leg 4 temperature predicted by the partners with the data

- **Summary of results comparison – hot leg coolant temperatures**

All models are able to simulate the transient with deviations based on the model setup and the used tool.

The temperature increase of leg 1 within the first 2s is predicted by all participants very close. Until the final state at 1800s KIT and CEA (but only until 600s) reproduce the plant data very good, while the models by UNIFI, Framatome and Energorisk are overestimating the final state temperature of about 2K. The Energorisk

model partially calculates high frequent temperature oscillations with an amplitude of $\pm 0.5\text{K}$, which are not visible in the data. A reason therefore maybe Fluent, which is very sensitive to the local mesh quality.

All participants overestimate the moderate temperature increase of loop 2, which means that the amount of hot coolant of loop 1 that enters into loop 2 is too high. While the models by Framatome, Pisa and Energorisk are over-predicting the temperature rise of 1K , the models by CEA and KIT are overestimating the final state temperature by nearly 4K . For the KIT model the reasons maybe the missing diffusion of upper plenum structures and a rather fine mesh in this region and the added swirl at the inlets. CEA and KIT are using additional pump swirl at the cold leg inlets which was adjusted mainly by the study of mixing in loop 1. Because the CEA model resolves the upper plenum in detail and shows similar over-predicting, pump swirl is considered as main reason and should be in future adjusted by studying the phenomena in all loops.

Loop 3 and 4 caused problems to the CEA model, which was not able to predict the initial low frequency oscillations of the plant data. Coolant temperature at FA-outlet at the initial state (time 0s).

It has to be mentioned that the accuracy of temperature measurements of plant data was specified by $\pm 2\text{K}$. As consequence, only the temperatures for loop 2 (see Fig. 26) by CEA and KIT are running out of the upper limit of plant data.

6.1.3 Data-vs-Predictions: Coolant temperature at FA-outlet at 0s and 1800s

In **Figure 30** and **Figure 31**, the comparison of the coolant temperature measure at the FA-outlet at time 0s and 1800s is given together with the predicted values of the different partners.

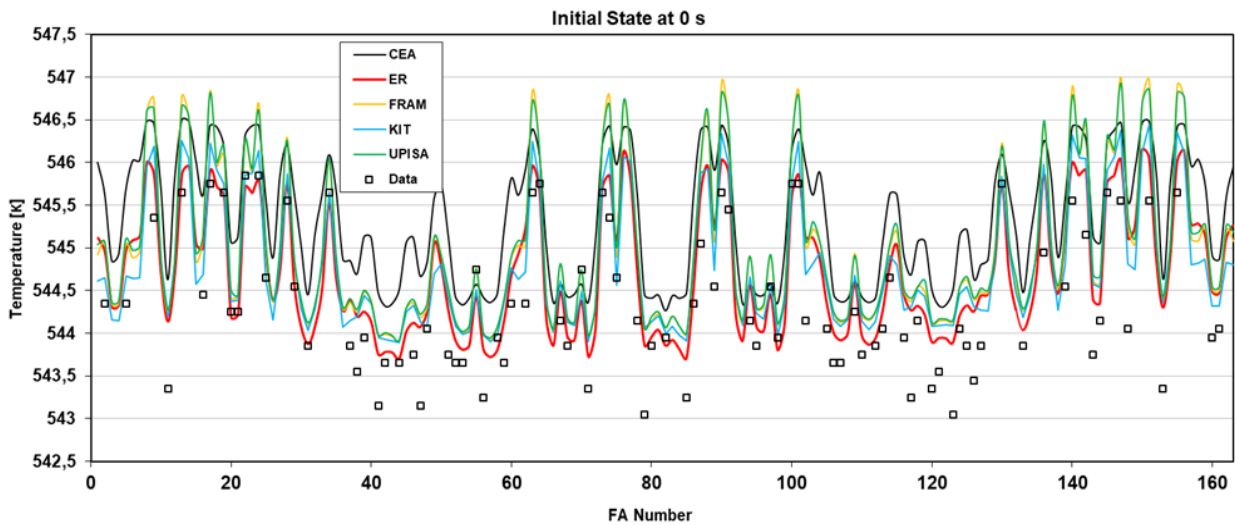


Figure 30: Comparison of the coolant temperature measured at the FA-outlet at 0s with the predicted values

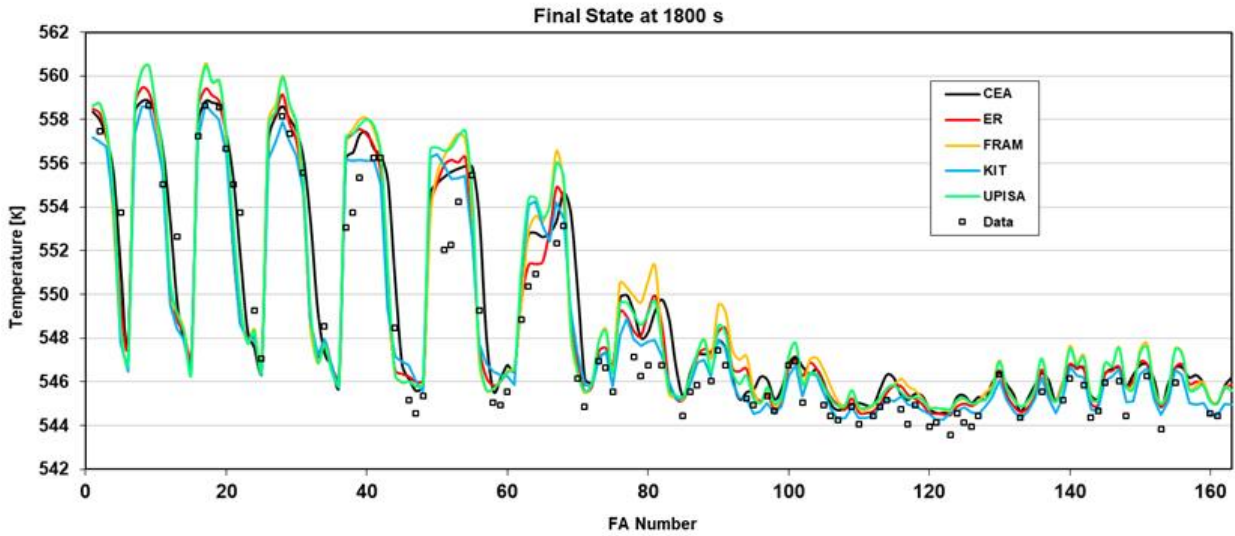


Figure 31: Comparison of the coolant temperature measured at the FA-outlet at 1800 s with the predicted values

The analysis of the initial state temperature distribution at the core outlet refers to a systematic problem between plant data and simulations, because in average the temperature are overestimated by roughly 0.5K by all participants. This fact was also observed in a previous benchmark of the OECD in 2010. According to the data accuracy of ± 2 K all models are in reasonable agreement at the initial state. At the final state, the agreement between simulations and measurements seems to be (by optical impression) improved, which is caused by the heat up of loop 1 of 10K. An analysis of the mean absolute errors show a significant increase of deviations between the initial and final state of all participants, **Table 12**.

Table 12: Error statistics of assembly averaged absolute temperature deviation vs. data [K]

t=0s /1800s	CEA	Energorisk	Framatome	KIT	UNIPI
av. deviation	0.93 / 1.10	0.39 / 1.14	0.66 / 1.50	0.46 / 0.92	0.68 / 1.38
max.dev	1.82 / 4.25	1.07 / 4.80	1.50 / 5.71	1.06 / 5.94	1.54 / 5.47
Assembly no	102 / 56	148 / 22	136 / 5	117 / 5	136 / 5

6.1.4 Data-vs-predictions: Loops coolant mixing coefficients

The comparison of the mixing coefficient predicted by the different partners with the data for the different cold legs (1 to 4) is shown in **Figure 32** to **Figure 35**.

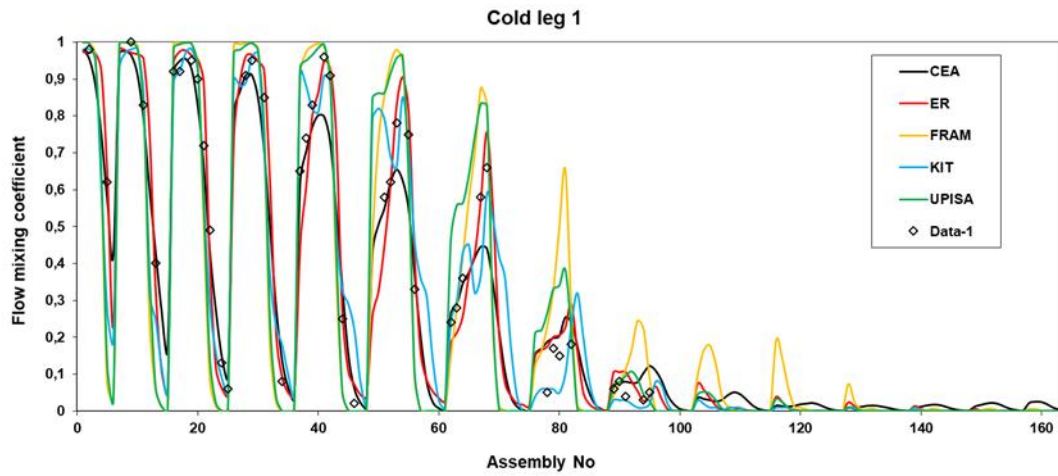


Figure 32: Comparison coolant mixing coefficient (data) of loop-1 with the predictions of the partners

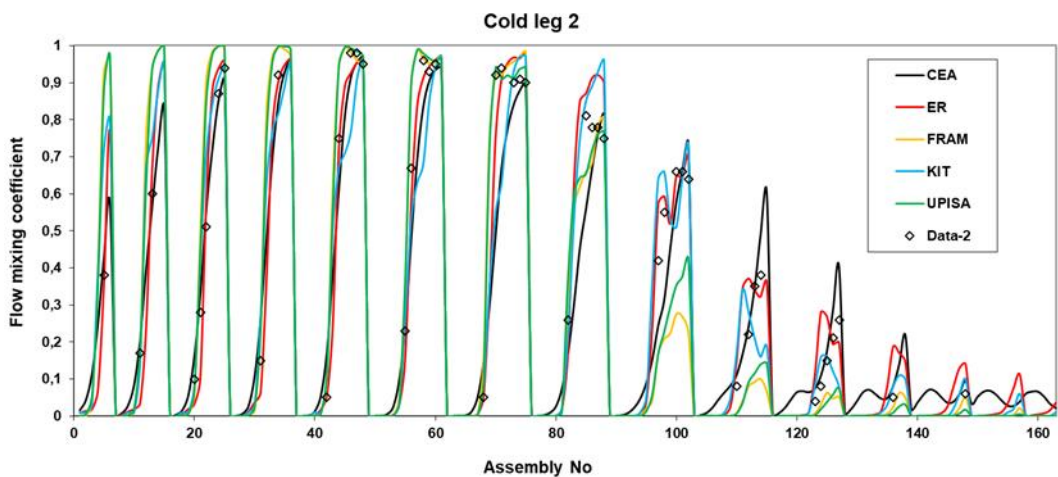


Figure 33: Comparison coolant mixing coefficient (data) of loop-2 with the predictions of the partners

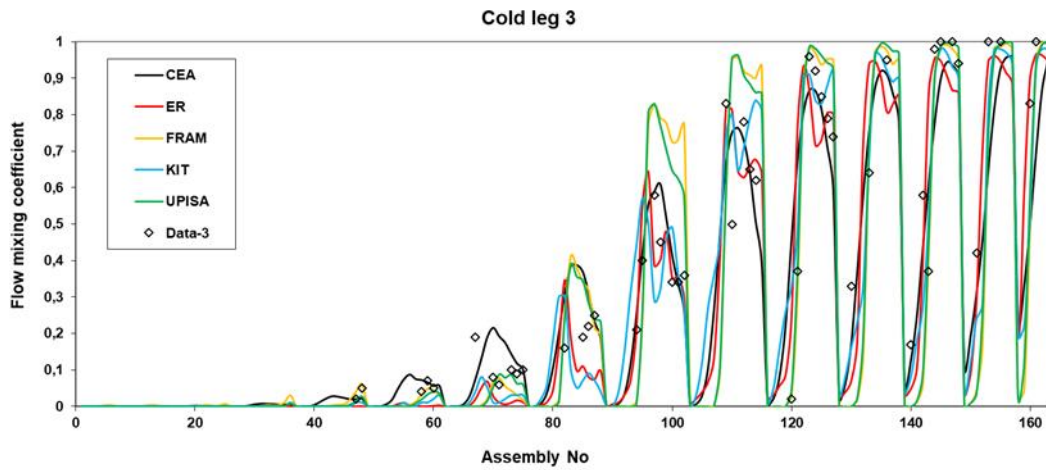


Figure 34: Comparison coolant mixing coefficient (data) of loop-3 with the predictions of the partners

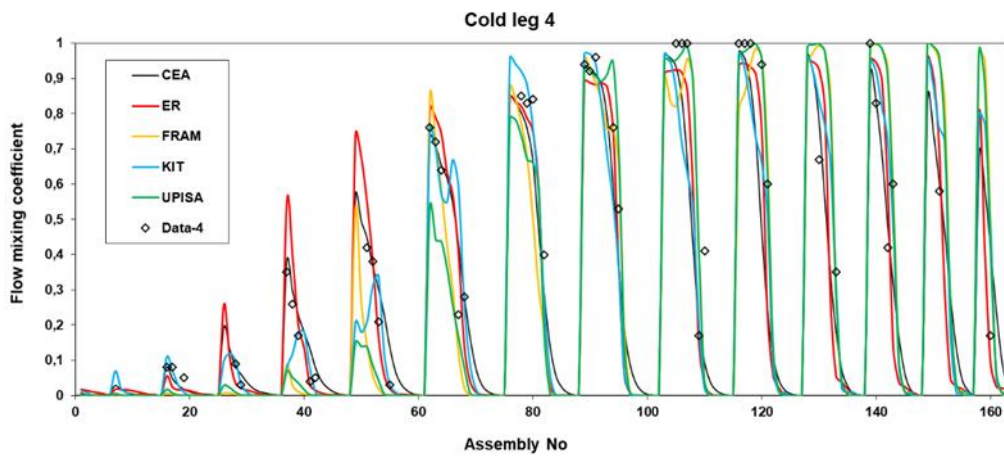


Figure 35: Comparison coolant mixing coefficient (data) of loop-4 with the predictions of the partners

The average absolute deviation of the different predictions with respect to the data are summarized in **Table 13**.

Table 13: Average absolute deviation of model results vs. data

	Loop 1	Loop 2	Loop 3	Loop 4	av. 1-4
CEA	0,060	0,081	0,111	0,099	0,088
ER	0,082	0,071	0,114	0,108	0,094
FRAM	0,135	0,134	0,148	0,145	0,141
KIT	0,079	0,109	0,116	0,118	0,106
UNIPI	0,150	0,121	0,135	0,139	0,136

6.1.5 Angular analysis – Loop 1:

The purpose of this analysis is to determine the central position of lowest coolant mixing for each loop in terms of the angular difference against the central cold leg inlet nozzle positions. In principle this can be done by analysis of passive tracer fields – mixing coefficients for each loop - or by analysis of temperature differences as for plant data, where the higher temperature at the inlet of cold leg 1 of about 10 K was used as tracer (by neglecting the thermal diffusion).

The mixing coefficients were calculated only for the initial state case, because of the lack of experimental data during the transient. The Figures 36-39 are presenting mixing coefficients for all loops and assemblies and the dependency on the local angular assembly positions at the core outlet. Furthermore, the central angular position of minimum coolant mixing in each loop for the plant data is shown (see indications “data centreline”).

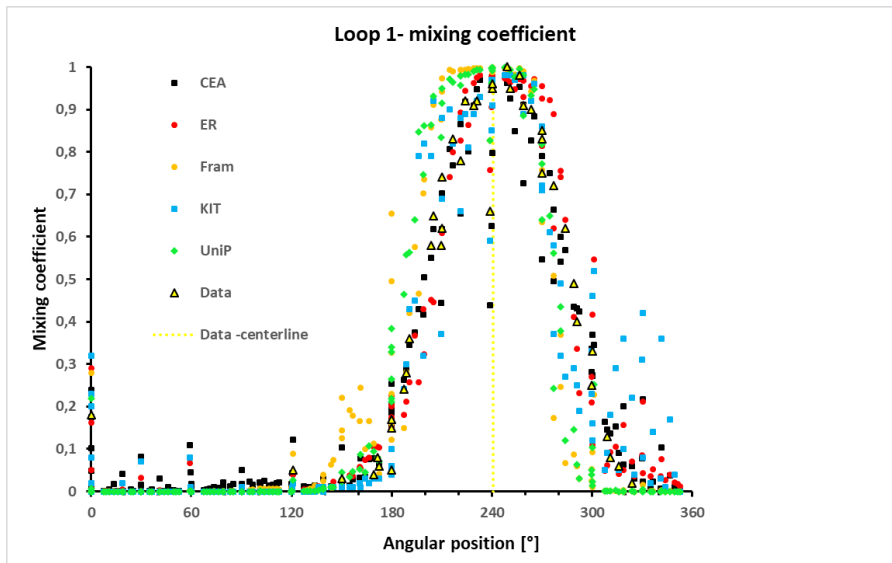


Figure 36: Angular position of mixing coefficients for loop 1

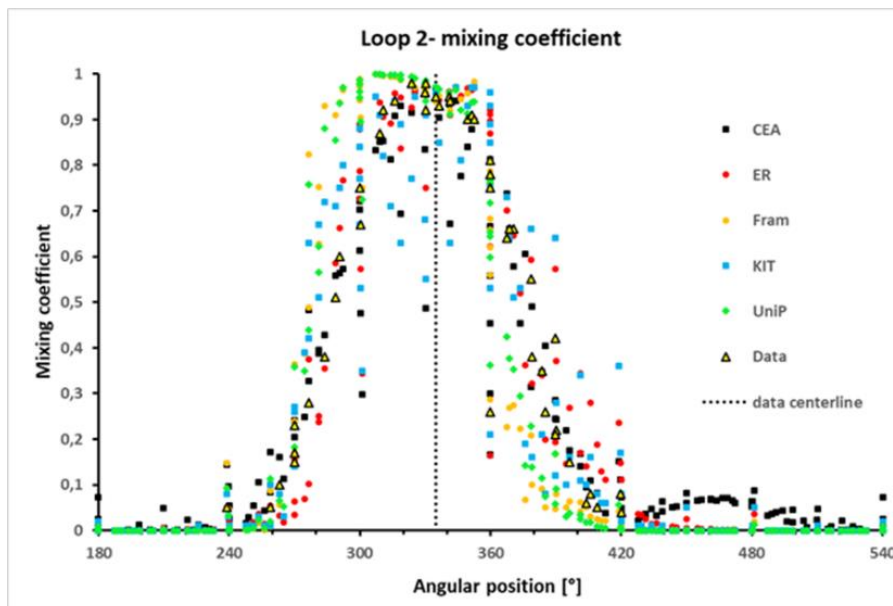


Figure 37: Angular position of mixing coefficients for loop 2

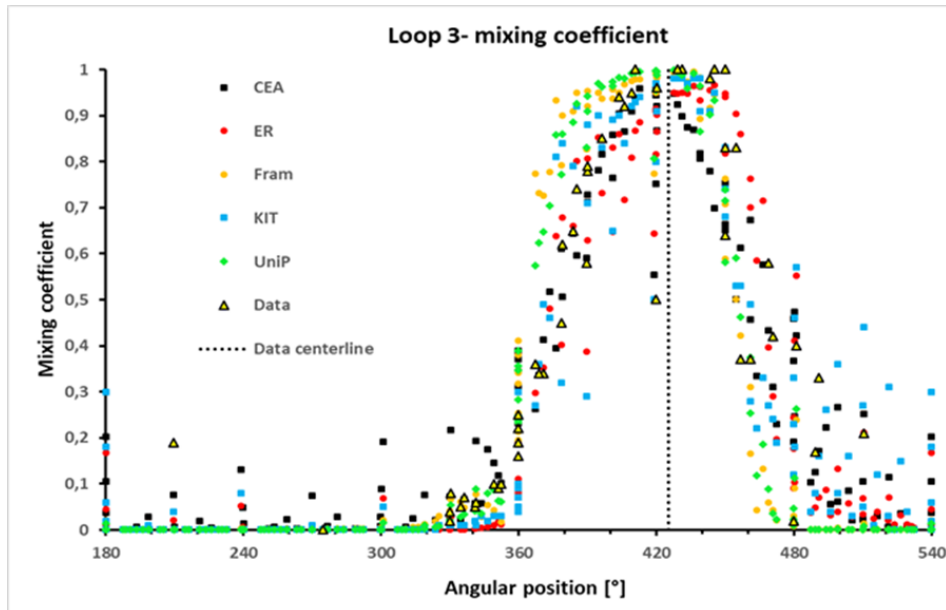


Figure 38: Angular position of mixing coefficients for loop 3

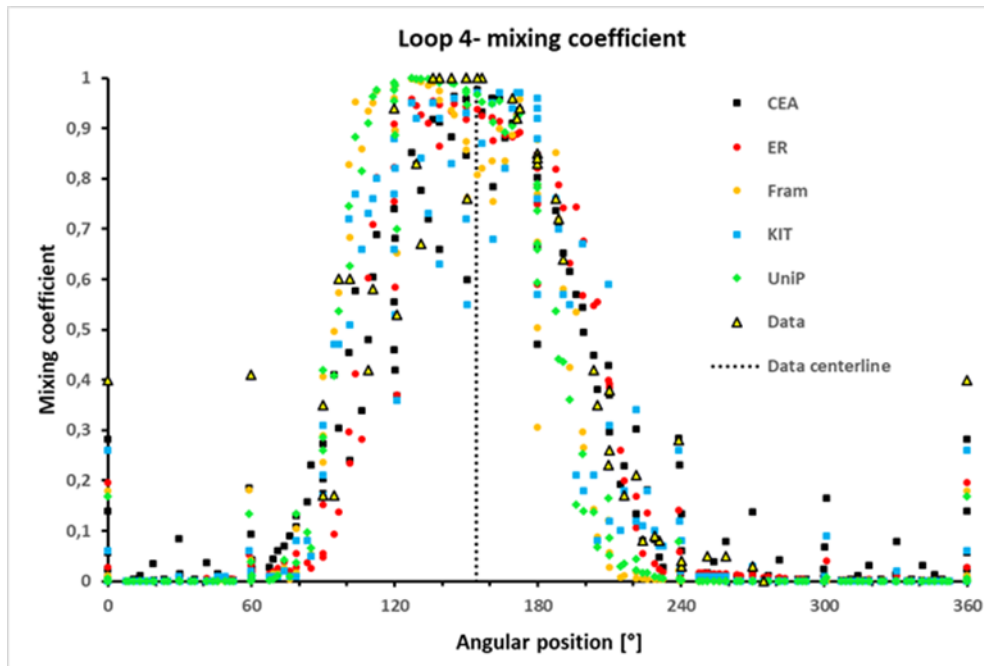


Figure 39: Angular position of mixing coefficients for loop 4

Additionally, an analysis at the core inlet for loop 1 at final state conditions was performed, where angular turns were calculated based on temperature differences between those at core inlet and cold leg inlet temperature at loop 1, see Fig. 40.

For the angular turn analysis the following algorithm was used:

Step 1: identification of assemblies with lowest mixing

$$\alpha_{ij} \geq 0.9 \text{ for mixing coefficients at core outlet } (i=1,4; j=1,163)$$

$$dT_{ij} \leq 0.8 \text{ K for temperature differences at core inlet } (i=1; j=1,163)$$

Step 2: calculation of center area for previously identified assemblies by arithmetic averaging of all individual assembly center points

Step 3: for the center area, the angular turn is calculated

It has to be mentioned that the final results are sensitive for the adjusted limits of 0.9 and 0.8 K.

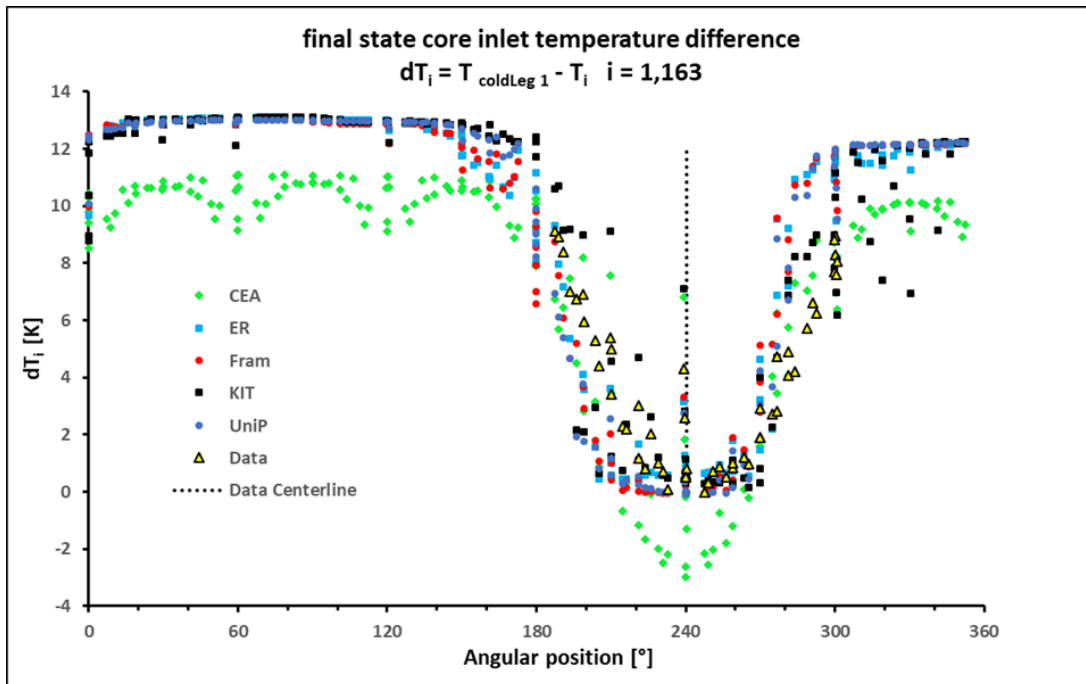


Figure 40: Loop 1 angular turn analysis for final state core inlet temperature differences

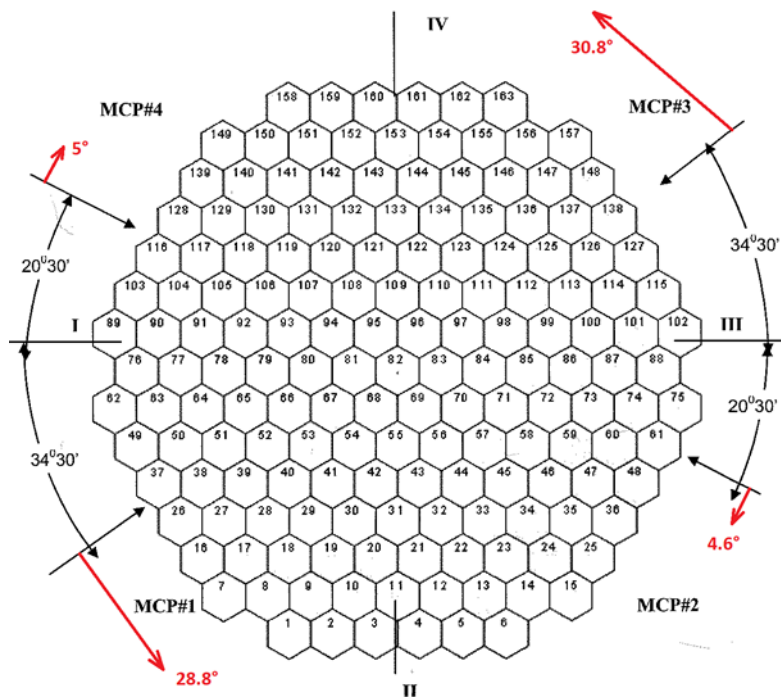


Figure 41: Angular turn of plant data at core outlet (final state)

Fig. 41 indicates the angular turns of plant data at the core outlet. The flow tries to achieve a circumferential regular arrangement. The absolute angular displacements between the loop centres are moving towards 90° (L1/L2: 91.6° L2/L3: 90.4° L3/L4: 89.2° L4/L1: 88.8°).

The best agreements at the core outlet for loop 1 were obtained by the CEA and KIT models. The reason therefore seems to be mainly the added swirl component at the cold leg inlets. The suggested swirl by KIT was adjusted mainly by obtaining best agreement for this loop.

Ang. Turn [°]	CEA	Energorisk	Framatome	KIT	UniP	Data	Av. deviation against data
Loop 1 ^a	27.1	34.0	22.8	28.0	21.2	28.8	-2.2
Loop 2 ^a	-6.8	-5.1	-20.2	-3.0	-3.0	-4.6	-3.0
Loop 3 ^a	23.7	41.3	17.0	26.6	26.6	30.8	-3.8
Loop 4 ^a	-3.3	-16.1	-25.5	-3.0	-19.0	-5.0	-8.4
Loop 1 ^b	26.6	22.9	24.8	30.7	25.5	26.5	-0.4
^a core outlet, mixing coefficient analysis, initial state ^b core inlet, temperature difference analysis, final state CEA and KIT models are using pump swirl at cold leg inlets							

Table 14 presents the angular turns for all loops and models at the core outlet. Furthermore, results at the core inlet based on temperature differences for loop 1 are shown.

For loop 1 the models show the lowest deviations against plant data. It has to be mentioned that the plant data is based on temperature differences, therefore loop 1 data should have the relative best accuracy compared with the data of the other loops. The turns of the other loops are calculated with significant larger deviations between the models and in comparison with plant data. The models with lowest deviations for all loops are by CEA and KIT. Both models are using additional pump swirl at the cold leg inlets and have lower maximum cell sizes compared with the other models. The overall tendency of the models is to underestimate the angular turn.

Between core inlet and core outlet the angular turn of loop 1 increases from 26.5° to 28.8° which seems to be reasonable because an imposed swirl continues downstream at decreasing strength as consequence of damping by friction in terms of core structures and dissipation.

At the core inlet a former OECD benchmark provided a value of 26° which is in reasonable agreement with the present analysis.

6.1.6 Code-to-code comparisons

6.1.6.a 2D thermal hydraulic parameters at core inlet

The comparison of the coolant temperature, mass flow rate and velocity predicted for the initial state is exhibited in Figures 42 to Figure 44.

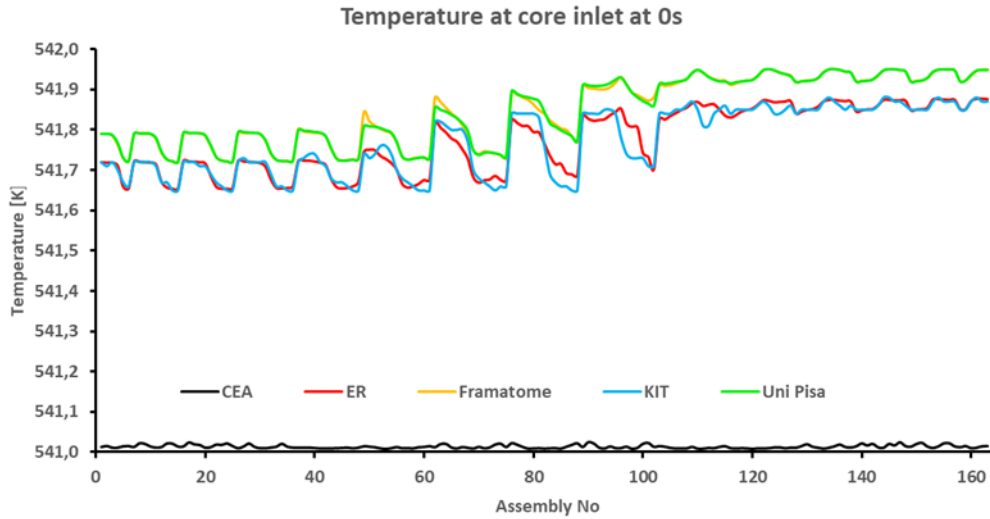


Figure 42: Coolant temperature at core inlet predicted for the initial state (0 s) by the partners

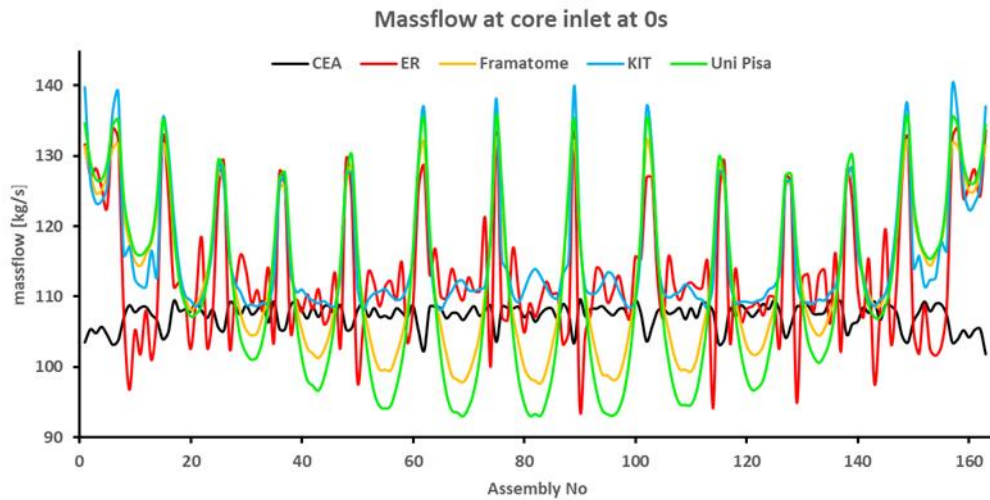


Figure 43: Mass flow rate at core inlet predicted for the initial state (0 s) by the partners

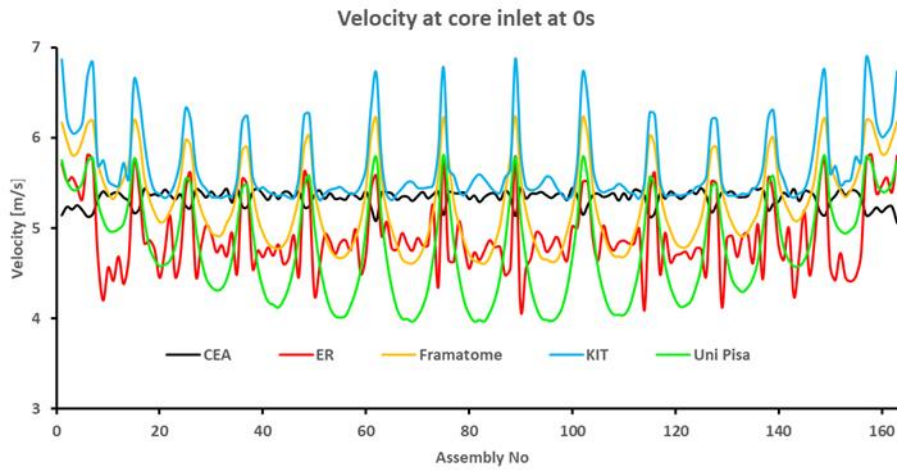


Figure 44: Coolant velocity at core inlet predicted for the initial state (0 s) by the partners

The comparison of the coolant temperature, mass flow rate and velocity predicted for the initial state is shown in Figure 45 to Figure 47.

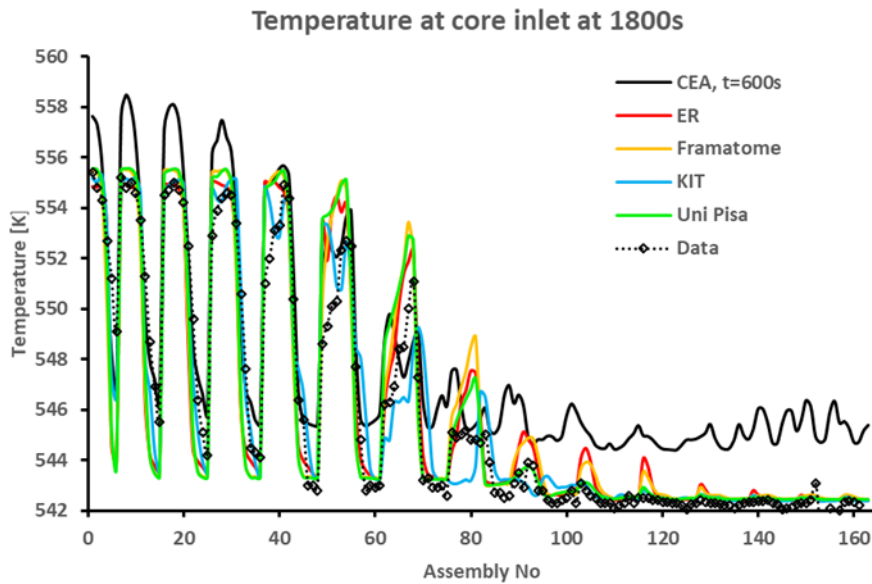


Figure 45: Coolant temperature at core inlet predicted for the final state (1800 s) by the partners

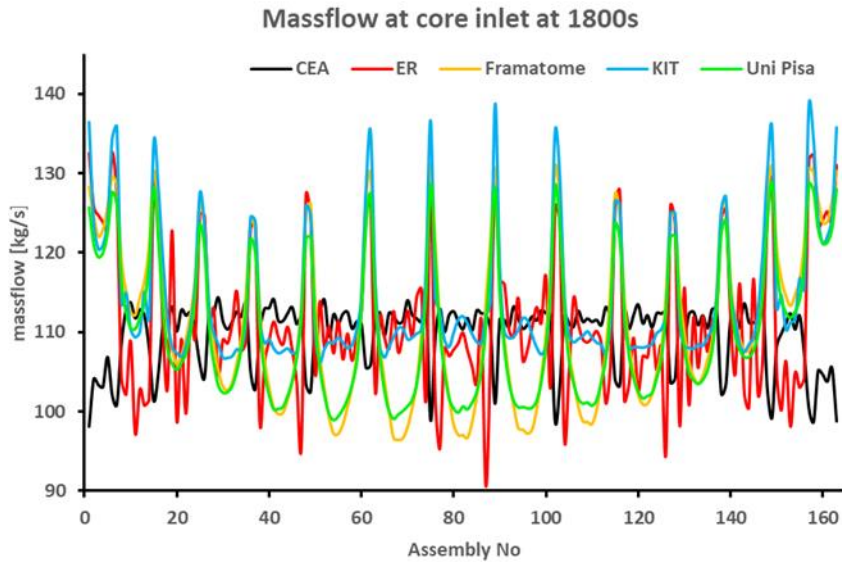


Figure 37: Mass flow rate at core inlet predicted for the final state (1800 s) by the partners

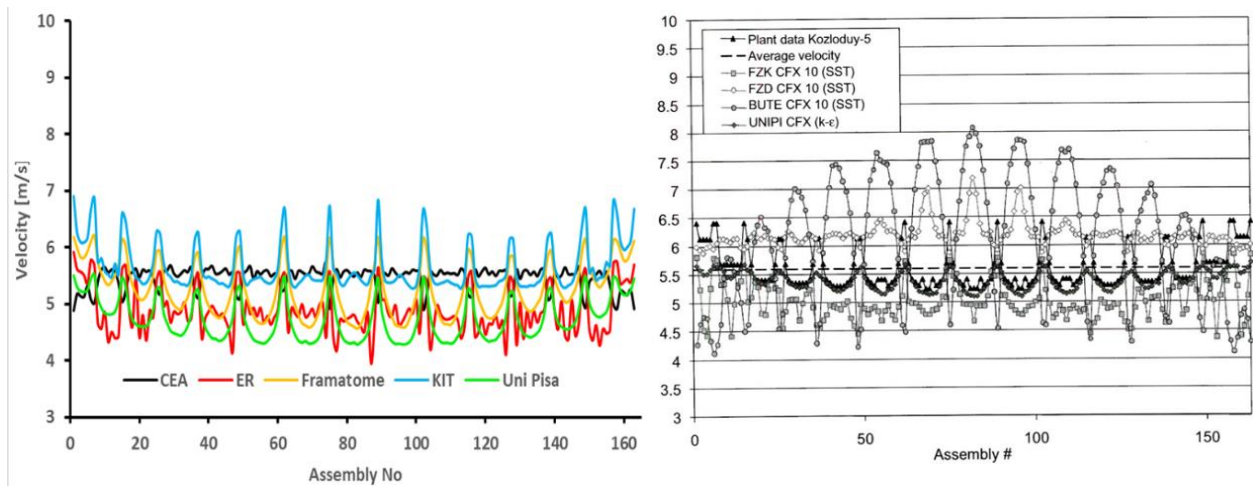


Figure 47: Coolant velocity at core inlet (1800 s) – comparison with OECD benchmark (2011)

Fig. 47 shows the distribution of coolant velocity at the core inlet and direct comparison with former OECD benchmark results [19]. The variations between the models have decreased significantly. The reasons are improved and bigger computer hardware (leading to larger models with smaller cell sizes and less numerical diffusion), improved meshing technics and more advanced porous media models.

The present (mainly commercial) meshing software makes boundary layer refinement possible also in high complicated geometries and is able to generate smarter transition regions between anisotropic regions like walls and isotropic regions. Furthermore, some commercial CFD tools like STARCCM+ support polyhedral cell types that allows a reduction of the cell numbers and therefore lower computational costs. Semi-automatic meshing technics have reduced the development time of models significantly. But it has to be mentioned that meshing has still a large user impact and it shows a high sensitivity on model results.

Concerning porous media modelling advances are made in the implementation of anisotropic source terms for momentum and energy and a more sophisticated handling of the solid phase. Also the numerical robustness of the solvers due to the handling of meshes of meshes with partially poor quality has reduced the development time for high complex CFD models.

The most sensitive data because of differences between the several models is the velocity distribution at the assembly inlets as shown in the Figures 44 and 47. The meshing and wall boundary resolution from the downcomer, the elliptical bottom plate and porous media model from the core support columns as well as different concepts for the bypass modelling provide significant uncertainty. Furthermore, different core porosity factors as shown by **Table 15** are one of the reasons of deviations between the models. In case of mass flow rates the differences between the models are smaller because variations of the core porosity have no influence.

	CEA	ER	Framatome	KIT	UNIFI
Core porosity	0.54	0.5887	0.46	0.5385	0.55

Between core inlet and outlet, the flow has suffered a significant pressure loss of approximately 1.4 bar, which homogenizes the velocity and mass-flow profiles. Compared with old benchmark results, the differences between the several models have become smaller. For the final state at the core inlet, the range for velocities from 4.2 m/s until 8.2 m/s has decreased now to 3.9 m/s to 6.9 m/s.

6.1.6.b 2D thermal hydraulic parameters at core outlet

The comparison of the FA-outlet mass flow rate and velocity predicted by the partners with the different CFD-codes is represented for the initial state is shown in Figure 48 and Figure 49.

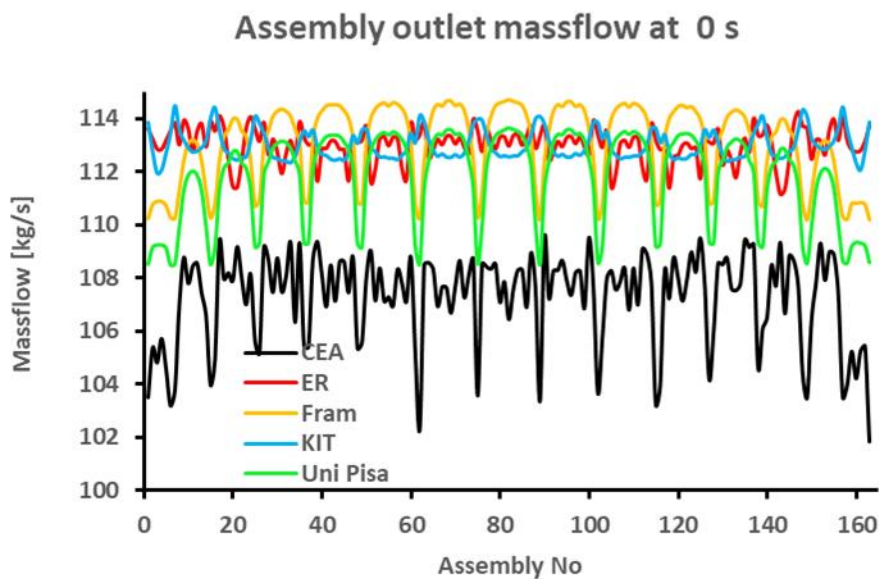


Figure 48: Coolant mass flow rate at FA-outlet predicted for the initial state (0 s) by the partners

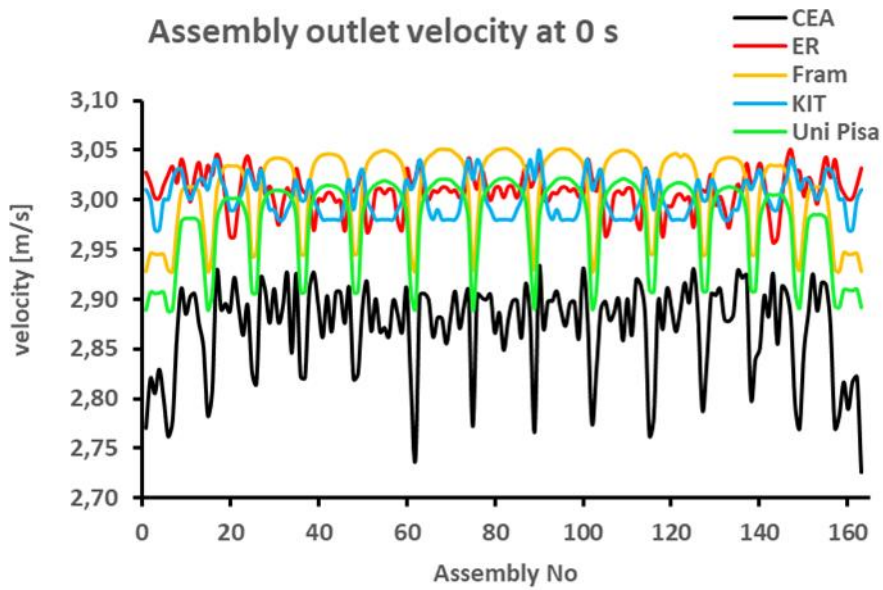


Figure 49: Coolant velocity at the FA-outlet predicted for the initial state (0 s) by the partners

The comparison of the FA-outlet mass flow rate and velocity predicted by the partners with the different CFD-codes is represented for the final state is shown in Figure 50 and Figure 51.

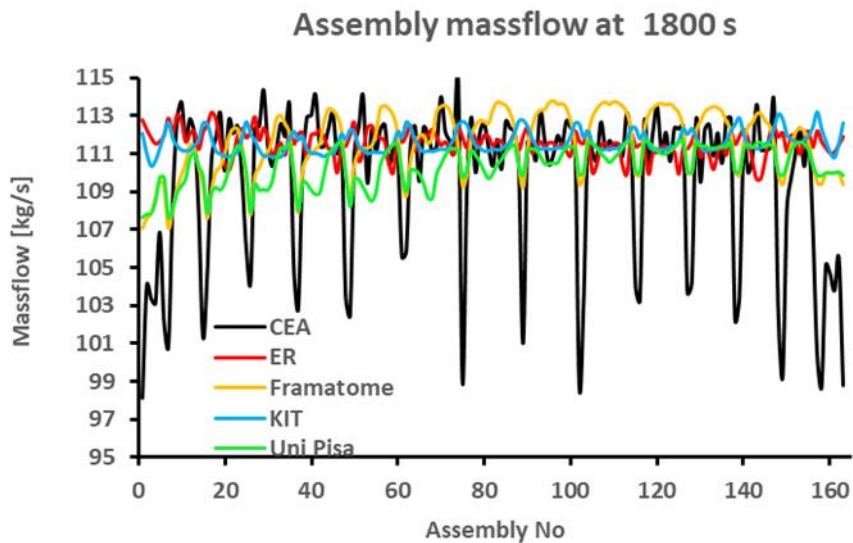


Figure 50: Coolant mass flow rate at FA-outlet predicted for the final state (1800 s) by the partners

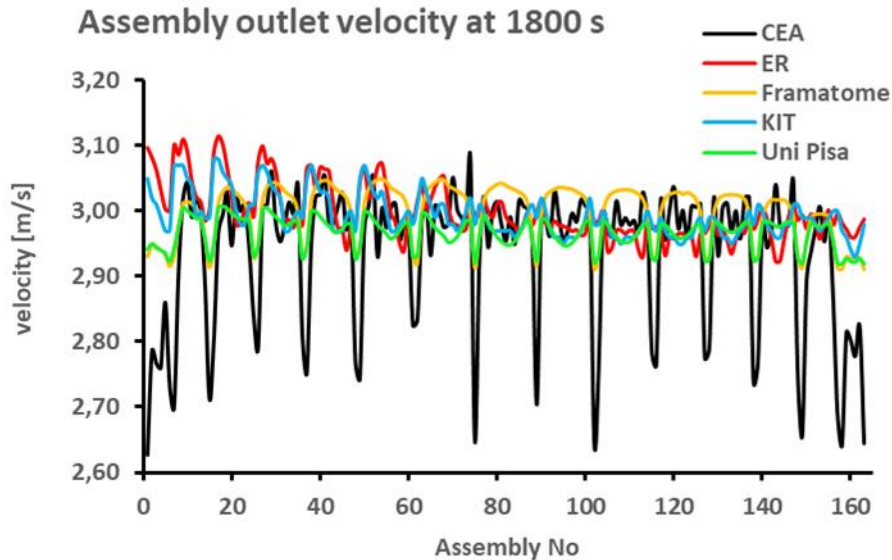


Figure 51: Coolant velocity at FA-outlet predicted for the final state (1800 s) by the partners

6.1.6.c Loops mass flow rate at RPV-outlet

The comparison of the loops mass flow rate at the RPV-outlet predicted by the partners with the different CFD-codes are represented in the Figures 52 to 55.

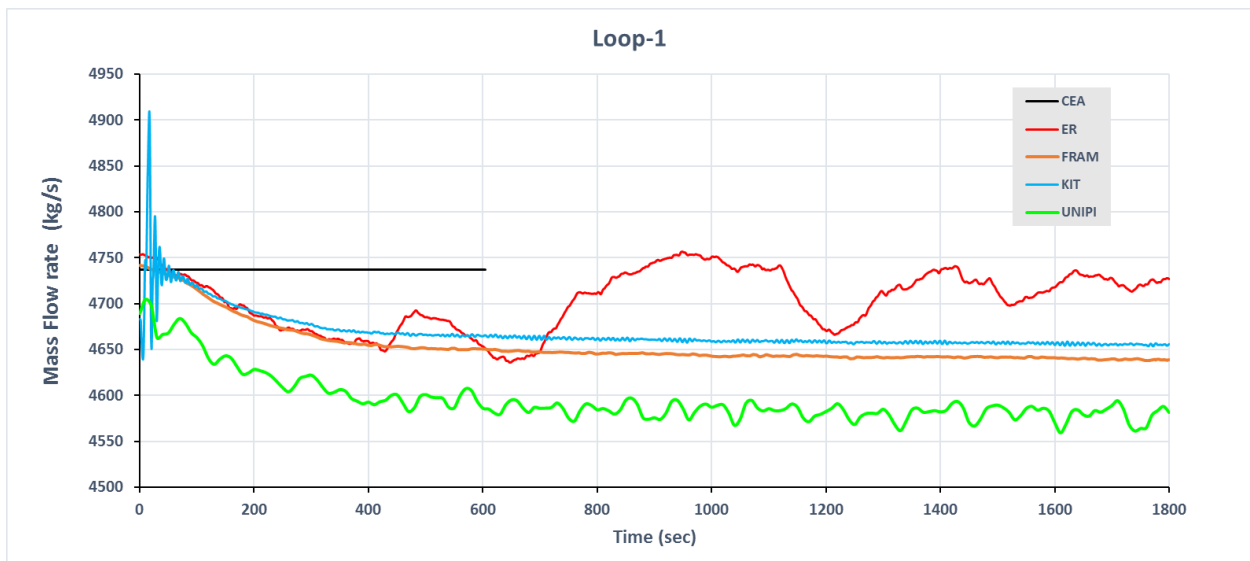


Figure 52: Loop-1 mass flow rate at the RPV-outlet predicted for the initial state (0 s) by the partners

The CEA model is solving only the energy equation, therefore the mass flow rate remains constant during the transient. The model by Framatome calculates a slightly decrease of the mass flow rates nearly without any oscillations while the models by KIT, Energorisk and UNI Pisa calculate oscillations at different frequencies and amplitudes. Compared with the average mass flow rates the amplitudes of the oscillations are low and in a range of 1%, but they are an indication of (mainly numerical) problems. For the KIT model it looks like a starter problem. After a short time the model stabilizes and the oscillations decay nearly completely. An improvement might be to use smaller time steps at the beginning of the transient. The specification of the reasons for oscillations in the other models requires some more detailed analysis.

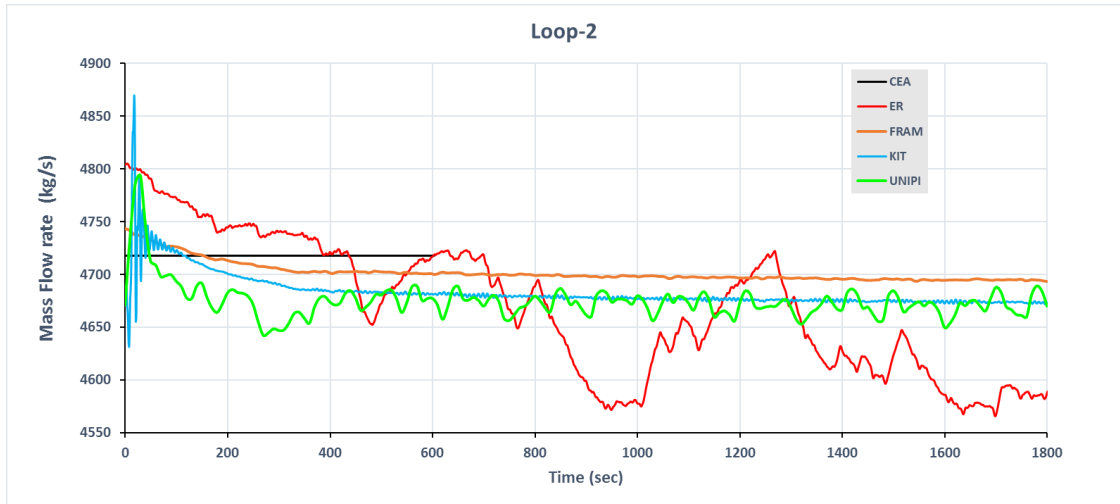


Figure 53: Loop-2 mass flow rate at the RPV-outlet predicted for the initial state (0 s) by the partners

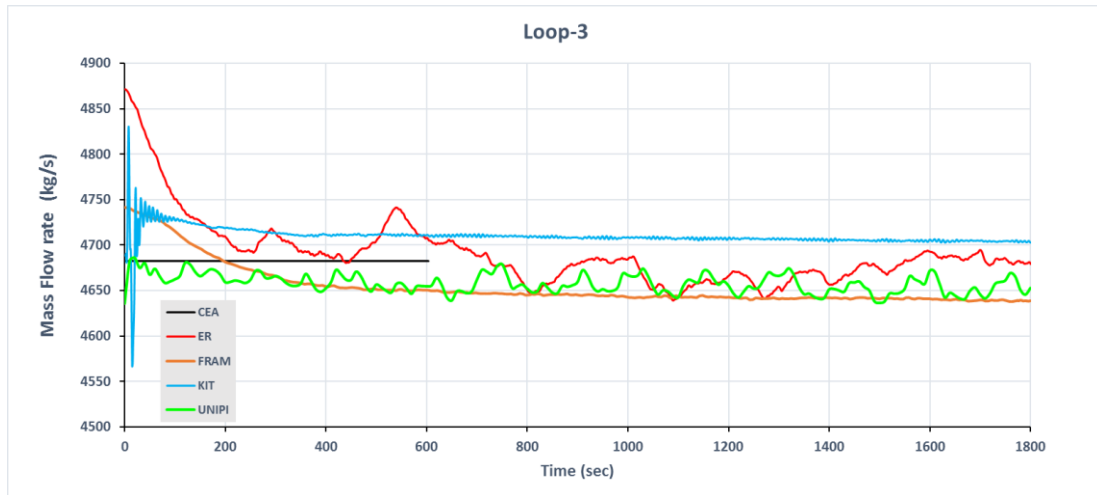


Figure 54: Loop-3 mass flow rate at the RPV-outlet predicted for the initial state (0 s) by the partners

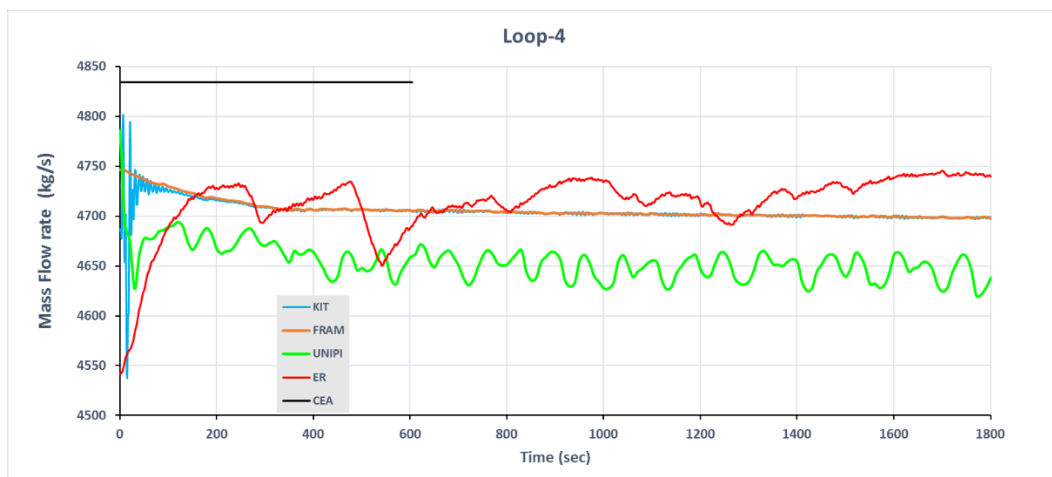


Figure 55: Loop-4 mass flow rate at the RPV-outlet predicted for the initial state (0 s) by the partners

7 Conclusions

The benchmark problem is equivalent with a former benchmark in 2010 by OECD. The results of the benchmarks can be directly compared, because the simulated scenario are completely identical. The improvements in the results of the new benchmark are a consequence of increased computer capacity, improved physical models and solver technics in CFD software such as porous media approaches. Further advances were obtained by the implementation of additional swirl at the cold leg inlets. Furthermore, significant improvements in meshing technics were made in the past decade.

In 2010, the average number of cells of the participant models was about 5.2 million cells and has increased to 27 million together with smaller time steps. Additionally, most participants were using a 1st order upwind scheme because of higher numerical stability and for the compensation of missing turbulent diffusion by additional numerical diffusion.

In the new benchmark, the modelling concept was to resolve all structures in the flow path from the inlets to the core outlet by resolving details as much as possible while upper plenum structures are considered mainly by porous media models (such as the core and the upper part of core support columns). All participants had to limit the cell number in order to obtain reasonable computational times for the transient scenario. This made a resolution of slot structures at core support column with essential impact on mixing impossible.

From the analysis of deviations and the comparison with the older benchmark the conclusion can be drawn, that a mesh with more spatial resolution of details but a coarser resolution of boundary layers is in advance towards a mesh with a finer resolution of wall boundaries but with additional porous media regions. A possibility of further improvement may be the tuning of mixing process in porous media regions like the core or core support columns (by fitted turbulent Prandtl and/or Schmidt numbers, sources for turbulent kinetic energy etc.) and a spatial resolution of structures with impact on coolant mixing as far as possible.

8 Bibliography

- [1] D. Verrier, B. Vezzoni, B. Calgaro, O. Bernard, A. P. C. L. A. H. P. Groudev, A. Stefanova, Z. Neli, F. Damian and e. al., “Codes and Methods for VVER comprehensive Safety Assessment: The CAMIVVER H2020 Project,” in *ICONE 2021-64169*, 2019.
- [2] N. Kolev, E. Royer, U. Bieder, S. Aniel, D. Popov and T. Topalov, “VVER-1000 Coolant Transient Benchmark Volume II: Specifications of the RPV Coolant Mixing Problem,” NEA/OECD NEA/NSC/DOC, Paris, France, 2004.
- [3] Siemens, “PLM Software: User Guide STAR-CCM+ v2019.3,” SIEMENS, Erlangen, Germany, 2019.
- [4] ANSYS, “Fluent User’s Guide. Release 2019 R3,” ANSYS INC. , Canonsburg (PA 15317), USA, 2019.
- [5] J. F. Wendt and e. all., *Computational fluid dynamics. An introduction*, 3rd edition, Germany: Springer-Verlag Berlin Heidelberg, 2009.
- [6] A. Jr. and J. D., “Computational Fluid Dynamics – An Engineering Tool? Numerical Laboratory Computer Methods,” *Fluid Dynamics Journal*, pp. 1-12, 1976.

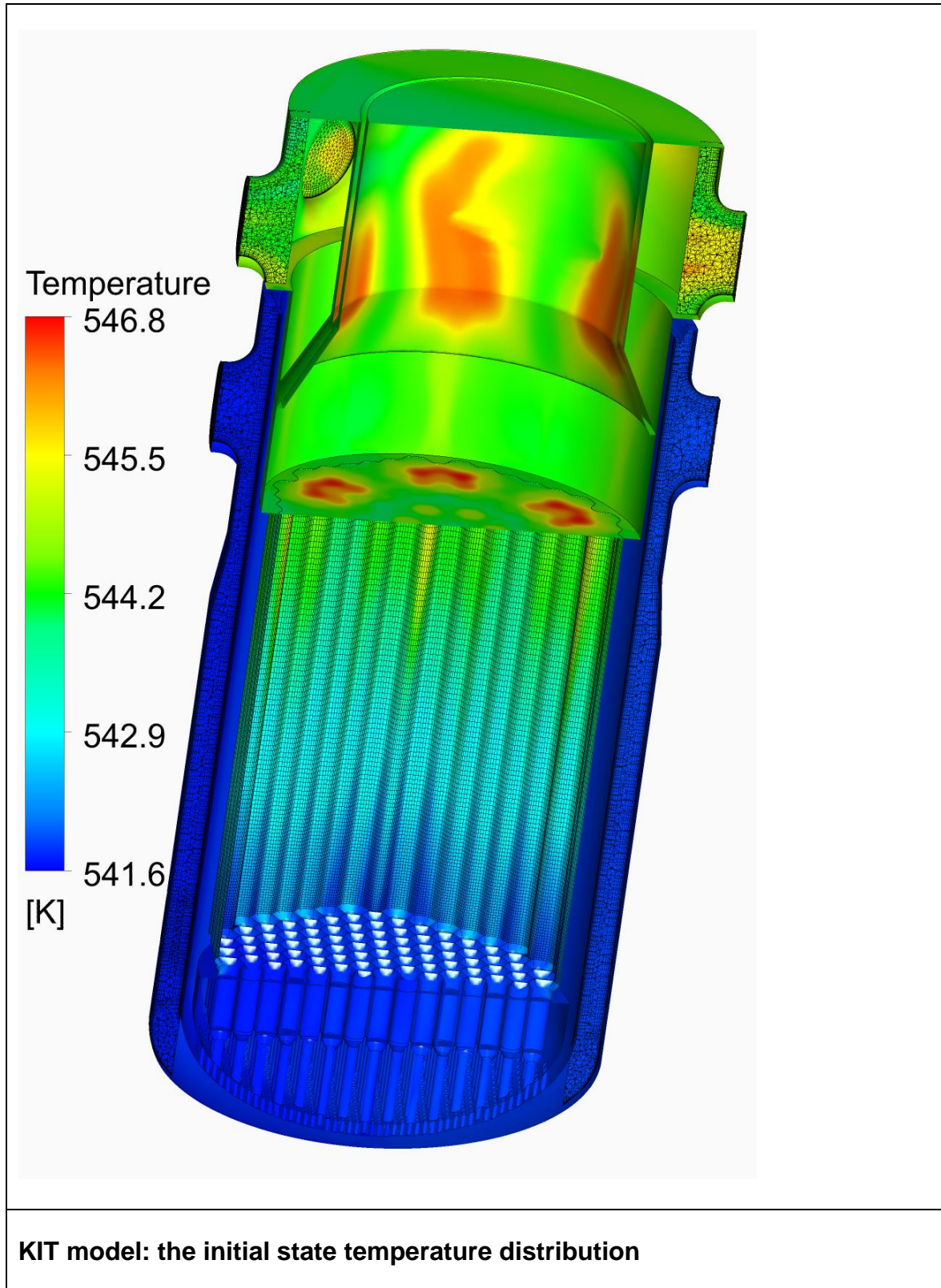
- [7] CFX, “ANSYS CFX, 2022 R2. Reference Guide.,” ANSYS, 2020.
- [8] P.-E. Angeli, U. Bieder and G. Fauchet, “Overview of the Trio_U code: Main features, V&V procedures and typical applications to engineering,” in *16th International Topical Meeting on Nuclear Reactor Thermal Hydraulics, NURETH-16*, Chicago, USA, 2015.
- [9] E. Saikali, P. Ledac, A. Bruneton, A. Khizar, C. Bourcier, G. Bernard-Michel, E. Adam and D. Houssin-Agbomson, “Numerical modeling of a moderate hydrogen leakage in a typical two-vented fuel cell configuration,” in *International Conference on Hydrogen Safety*, Edinburgh, United Kingdom, 2021.
- [10] S. Pope, *Turbulent Flows*, Cambridge: Cambridge University Press, 2000.
- [11] H. Reichardt, “Vollständige Darstellung der turbulenten Geschwindigkeitsverteilung in glatten Leitungen,” *Journal of Applied Mathematics and Mechanics*, vol. 31, no. 7, pp. 208-219, 1951.
- [12] V. Girault and P.-A. Raviart, “Finite Element Methods for Navier-Stokes Equations,” *Springer Series in Computational Mathematics*, 1986.
- [13] J. Ferziger and M. Peric, *Computational Methods for Fluid Dynamics*, Springer, 2002.
- [14] F. R. Menter, “Zonal Two Equation k- ω Turbulence Models for Aerodynamic Flows,” *AIAA*, pp. 93-2906, 1993.
- [15] M. Böttcher, “Detailed CFX-5 study of the coolant mixing within the reactor pressure vessel of a VVER-1000 reactor during a non-symmetrical heat-up test,” *Nuclear Engineering and Design*, p. 445–452, 2008.
- [16] M. Böttcher and R. Krüßmann, “Primary loop study of a VVER-1000 reactor with special focus on coolant mixing,” *Nuclear Engineering and Design 240 (2010) 2244–2253*, p. 2244–2253, 240 February 2010.
- [17] T. J. Barth and D. C. Jespersen, “The Design and Application of Upwind Schemes in Unstructured Meshes,” *AIAA Journal*, pp. 89-036, 1989.
- [18] A. Stefanova, N. Zaharieva, P. Vryashokava and P. Groudev, “The CAMIVVER Definition Report with Specification for NPP with VVER-1000 reactor with respect to selected transients,” CAMIVVER, Sofia, Bulgaria, 2020.
- [19] N. P. Kolev, I. Spasov and E. Royer, “VVER-1000 Coolant Transient Benchmark Phase 2 (V1000CT-2), Summary Results of Exercise 1 on Vessel Mixing Simulation,” NEA No. 6964, OECD, Paris, 2010.
- [20] G. Geffraye, O. Antoni, M. Farvacque, D. Kadri, G. Laviaille, B. Rameau and A. Ruby, “CATHARE 2 V2.5_2 : a Single Version for Various Applications,” *Proceeding of NURETH-13, Kanazawa City, Ishikawa Prefecture, Japan, Sept 27th-Oct 2nd*, 2009.
- [21] OECD/NEA, “Handbook on Lead-Bismuth Eutectic Alloy and Lead Properties, Materials Compatibility, Thermal-Hydraulics and Technology”, ISBN 978-92-64-99002-9, 2007.

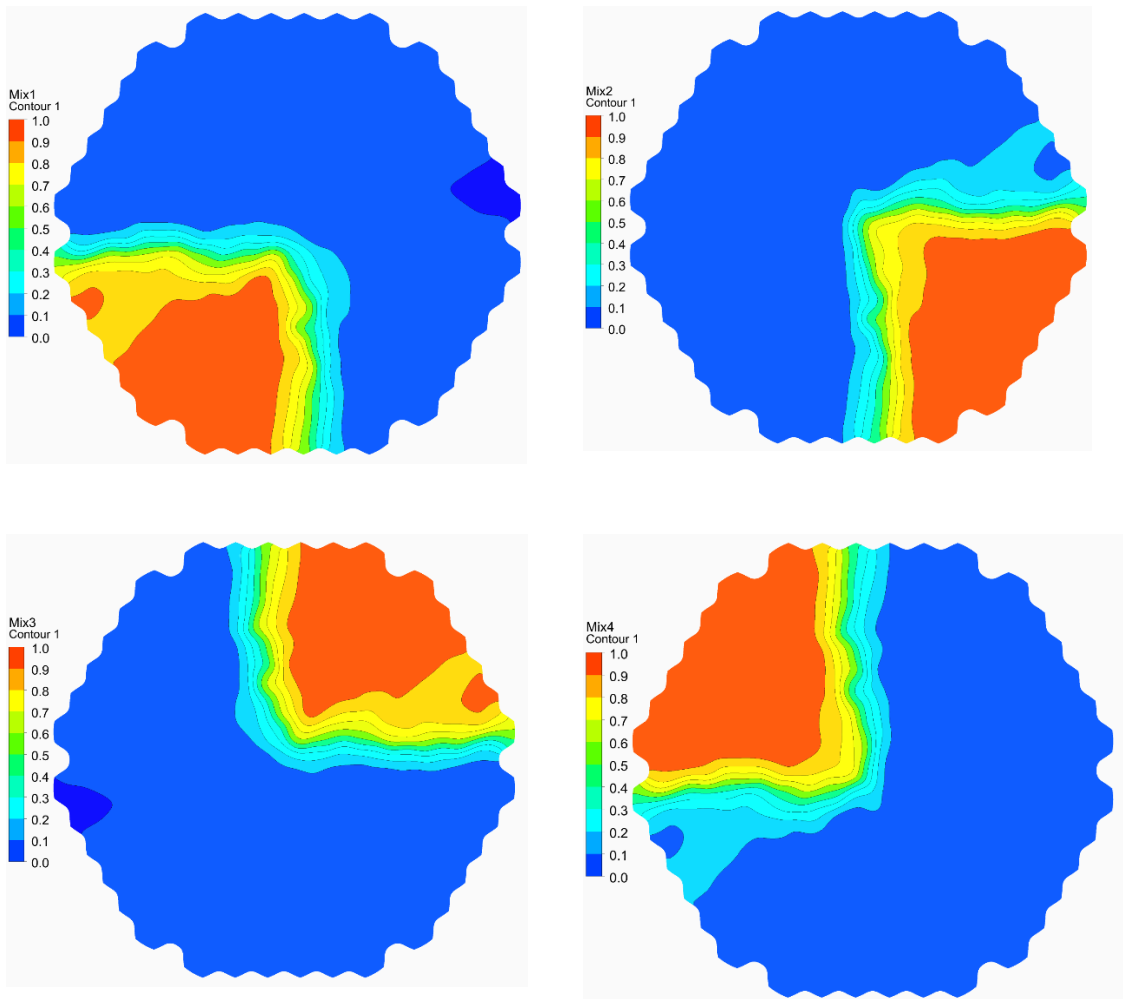
- [22] M. Polidori, "Implementation of Thermo-Physical Properties and Thermal-Hydraulic Characteristics of Lead-Bismuth Eutectic and Lead on CATHARE Code," *Rapporto Tecnico ENEA, NNFISS – LP1 - 001*, 2010.
- [23] I. Idelchik, *Handbook of Hydraulic Resistance*, 3rd ed., Jaico Publishing House, 2003.
- [24] S. Chen, N. Todreas and N. Nguyen, "Evaluation of existing correlations for the prediction of pressure drop in wire-wrapped hexagonal array pin bundles," *Nuclear Engineering and Design*, vol. 267, pp. 109-131, 2014.
- [25] Leibowitz and et al., "Properties for LMFBR safety analysis," *ANL-CEN-RSD-76-1*, 1976.
- [26] D. Rozzia, G. Fasano, I. Di Piazza and M. Tarantino, "Experimental investigation on powder conductivity for the application to double wall heat exchanger (NACIE-UP)," *Nuclear Engineering and Design*, pp. Volume 283, Pages 100–113, March 2015.
- [27] N. Forgione, M. Angelucci, D. Martelli and W. Ambrosini, "Proposal for a numerical benchmark on thermal-hydraulics for heavy liquid metal cooled system," *SESAME Deliverable 4.9, rev. 1*, 2016.

A Additional core configurations

A.1 Assorted model results

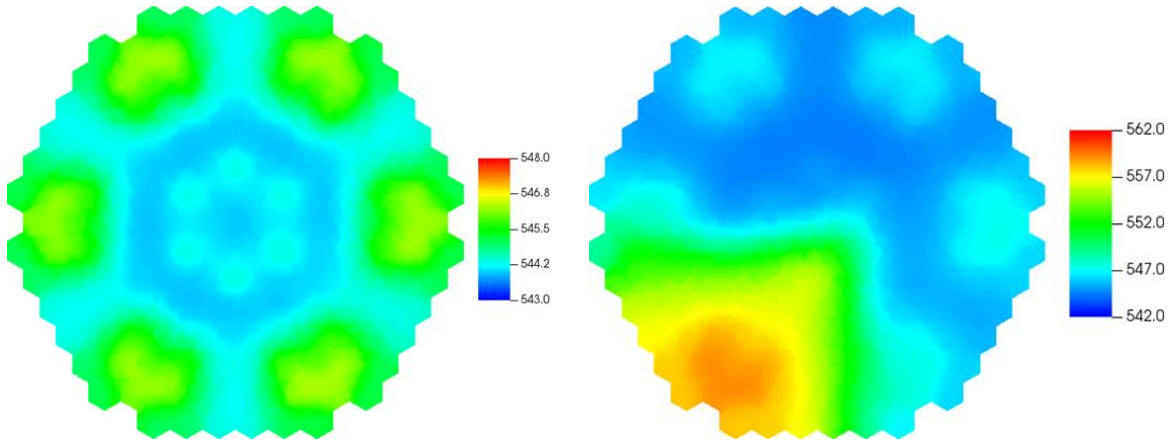
A.1.1 ANSYS CFX (KIT)



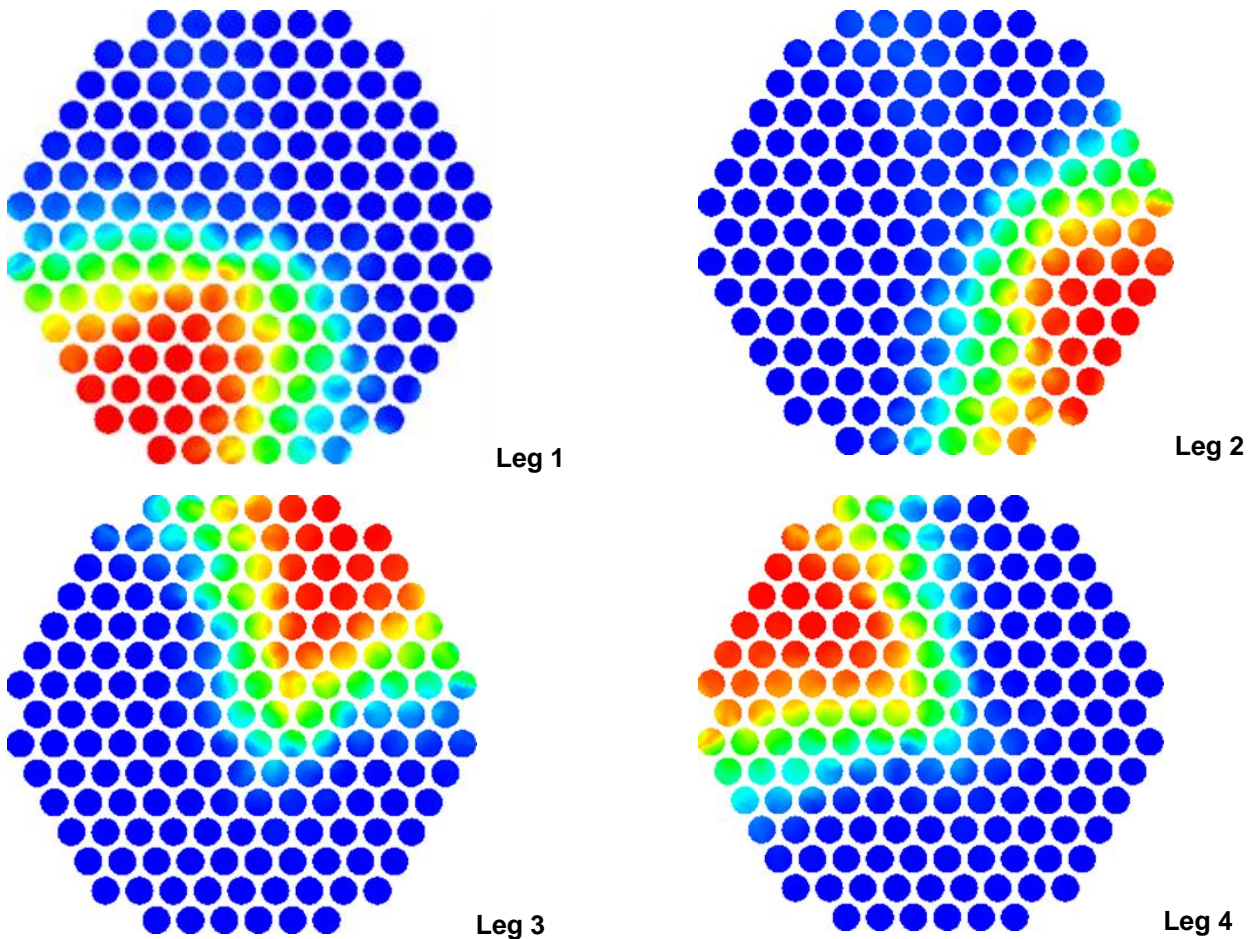


ANSYS CFX: Loops coolant mixing coefficients at core outlet (t=0s)

A.1.2 TrioCFD (CEA)

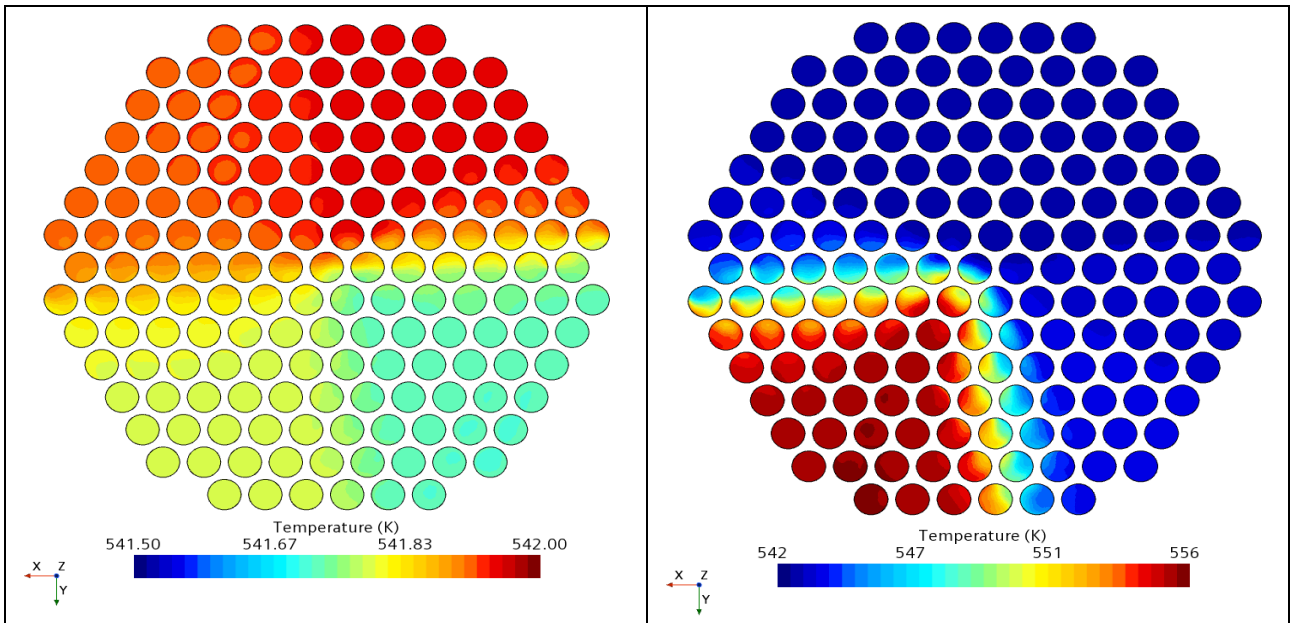


Coolant temperature at initial state and at final state (600s)

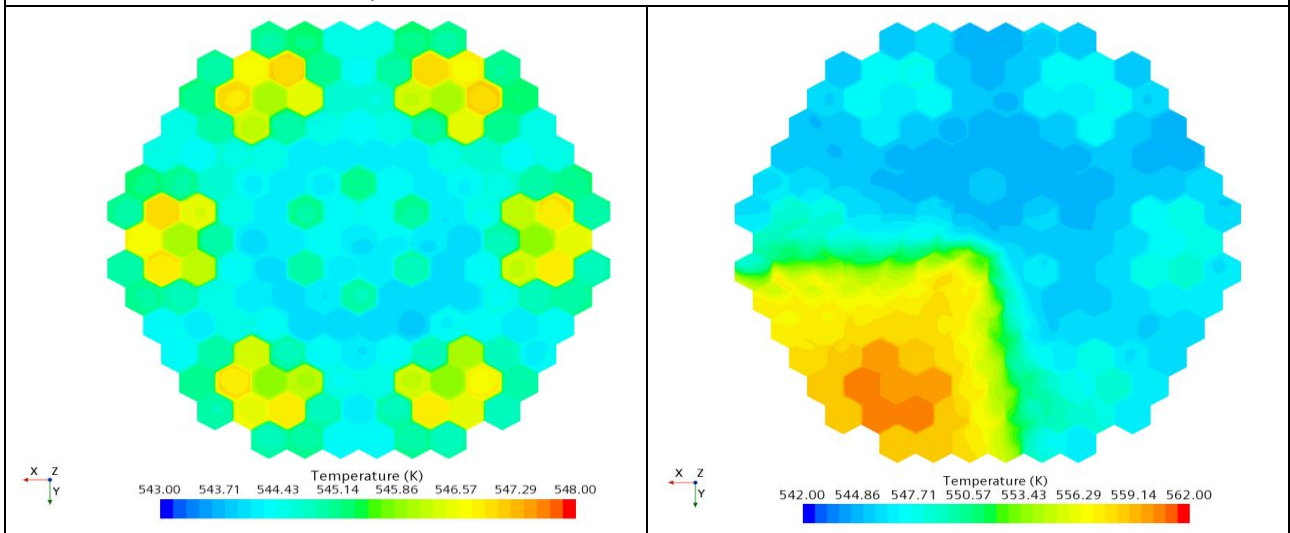


Loops coolant mixing coefficients (t=0s)

A.1.3 UPISA STAR-CCM+



STAR-CCM+: 2D coolant temperature at core inlet at 0 and 1800 s

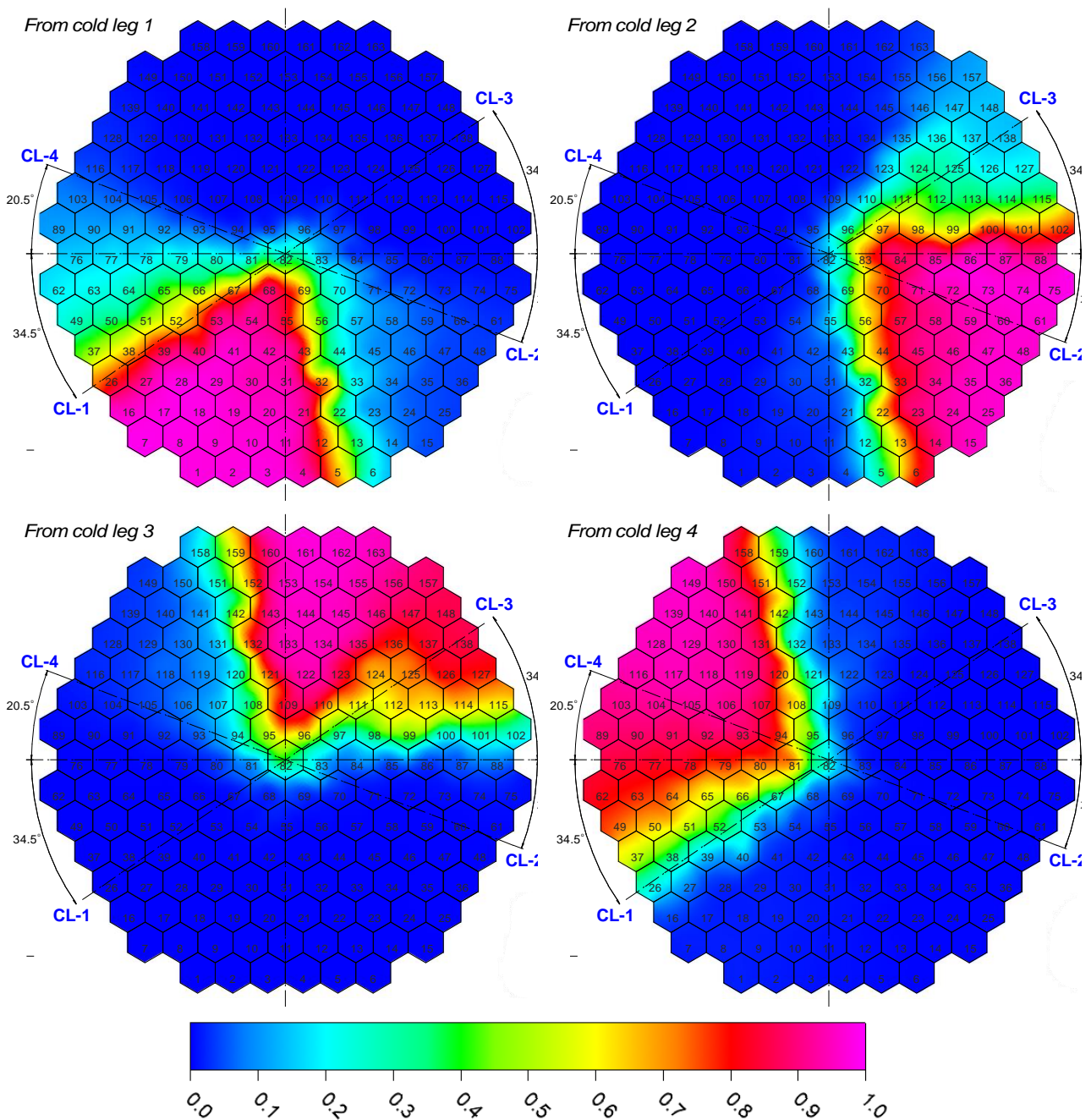


STAR CCM+: 2D coolant temperature at core outlet at 0 and 1800 s

A.1.4 ENERGORISK FLUENT

Predicted spatial distribution and spreading/transport of the mixing coefficients for the initial state. The mixing coefficients represent absolutely portion of a flow from the corresponding loop (cold leg) from total flow in the considered area of a model space; mixing coefficients are modelled using so-called passive scalars of additional flow transport equations. The azimuthal shift of the flow distribution (mixing coefficients) relative to the cold legs axis, as expected, corresponds to the asymmetry of the coolant flow rate from the CLs.

The most intensive mutual mixing is characteristic on the boundary of the sectors of the neighbouring 1st and 4th loops, which have the highest flow in the system; in this case, the flow from the 4th loop, which has the highest flow rate (kinetic energy), significantly shifts the flow from the 1st loop in the direction of the opposite 2nd loop, which has a proportional flow rate with the 1st loop.



CL-1:
MFR=4737 kg/s
T=541.72 K

CL-2:
MFR=4718 kg/s
T=541.65 K

CL-3:
MFR=4682 kg/s
T=541.88 K

CL-4:
MFR=4834 kg/s
T=541.85 K

Fig. 8.1 – The spatial distribution of mixing coefficients from cold legs to fuel cassettes outlet

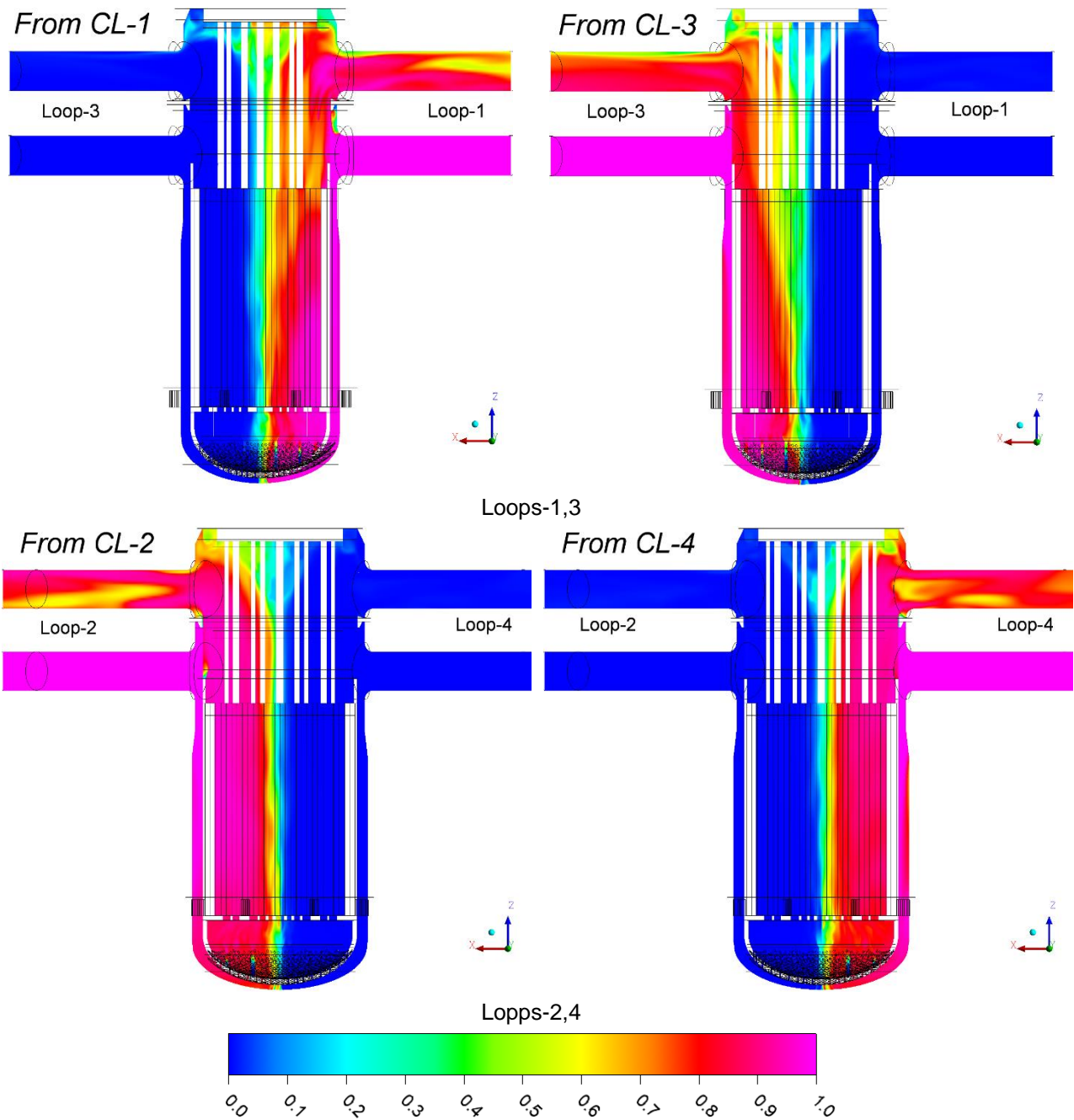
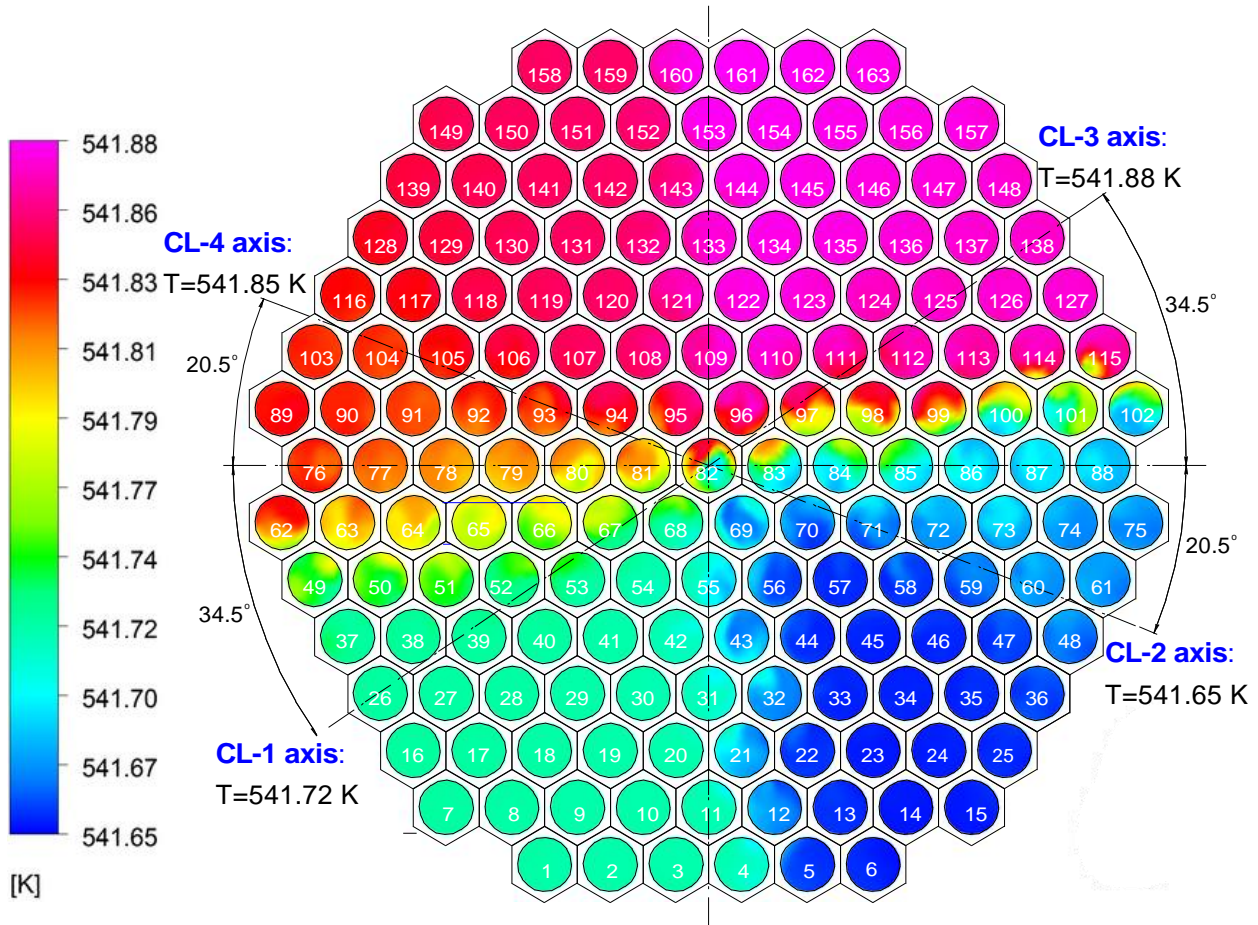


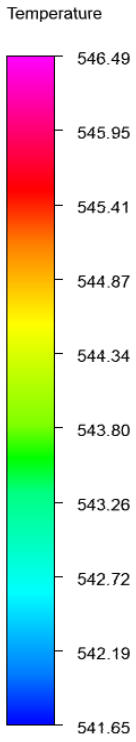
Fig. 8.2 – The spatial distribution of mixing coefficients from cold legs to vessel space (loops axial plane)

The spatial (2D) distribution of the main parameters (temperature, velocity, pressure) is shown in order to confirm the correctness of the calculated results of quasi-stationary calculation at the initial state of V1000CT-2 mixing experiment simulation: 2D Fa inlet temperature distribution in the normal cross-section (in relation to the core location) of the XY-plane

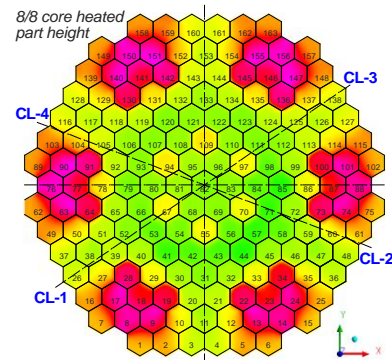
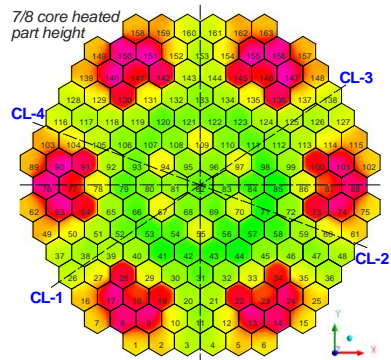
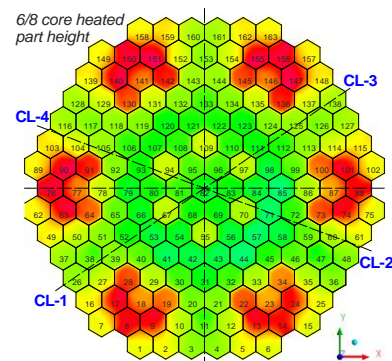
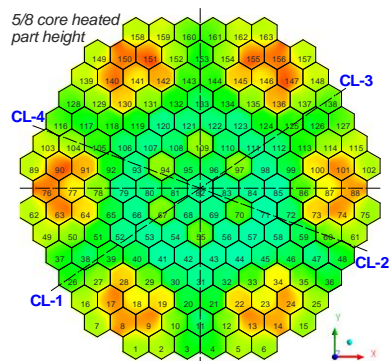
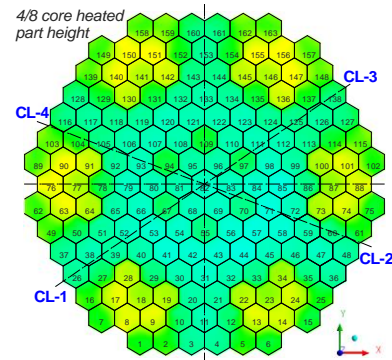
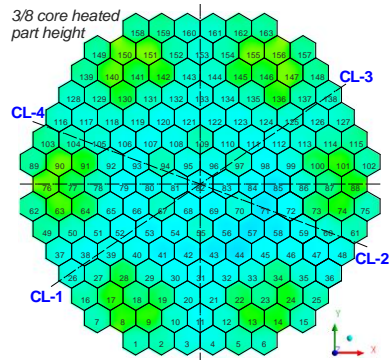
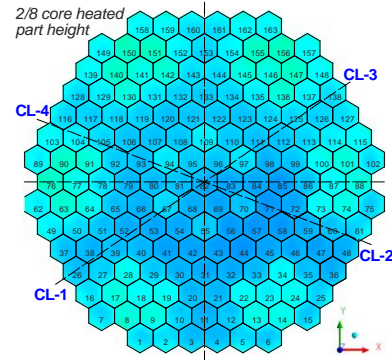
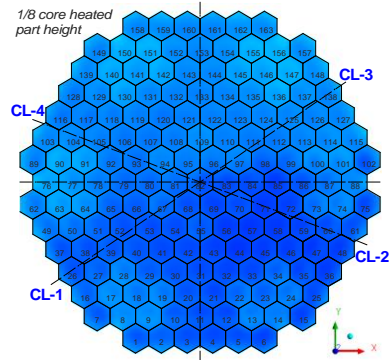


The spatial distribution of cassettes inlet temperature

- The spatial distribution of temperature by core heated part height: core temperature distribution in the normal cross-sections (in relation to the core location) of the XY-planes:



[K]



Pressure, velocity and temperature global range; ZX normal axial plane: pressure, velocity and temperature distribution in the normal section (in relation to the core location) of the ZX-plane.

